

© 2019

Namrata

ALL RIGHTS RESERVED

EPITAXIAL GROWTH OF TOPOLOGICAL MATERIALS

By

NAMRATA

A dissertation submitted to the

School of Graduate Studies

Rutgers, the State University of New Jersey

In partial fulfillment of the requirements

For the degree of

Doctor of Philosophy

Graduate Program in Electrical & Computer Engineering

Written under the direction of

Seongshik Oh

And approved by

New Brunswick, New Jersey

January, 2019

ABSTRACT OF THE DISSERTATION

Epitaxial Growth of Topological Materials

By NAMRATA

Dissertation Director:

Seongshik Oh

Recently, in 2007, a new electronic phase was discovered – termed as Topological Insulator (TI) – a bulk insulator that has conducting states bound to its surface. An apt analogy would be a ceramic block coated with a nanometer thick layer of metallic paint, so that electrical conduction occurs only on the surface, except in this case, the material is the same throughout. The understanding of topological insulators is based on the previously thought to be complete band theory, but taking into account the topological effects. The term topological implies the presence of certain bulk invariants that help differentiate between different systems having the same symmetry. The work presented here concerns the understanding of the transport properties of these electronic states that emerge only on the surfaces of this very special class of materials.

The spin of electrons in the heavy metals of the TIs is linked to their intrinsic angular momentum; this spin-orbit coupling (SOC) leads to twisting of the electronic

states in certain regions of momentum space, establishing a topological order. The term topology comes from mathematics, and deals with quantities remaining invariant under continuous modifications – it is the topology of the electronic band structures originating from SOC that protects these metallic surface states against disorders. The SOC also coerces the motion of spin-up electrons in one direction and spin-down electrons in the other – a distinguishing feature that forbids complete backscattering and localization i.e. the electrons can move freely with little or no resistance in their preferred direction. This ‘spin-momentum locking’ makes these materials interesting for future spintronic devices that require generation, control and detection of spins as information carriers.

The dissertation begins by reviewing the developing field of TIs which inspired this work, followed by an introduction to the many aspects involved in the growth of atomically precise thin TI films, mainly Bismuth Selenide (Bi_2Se_3). The details of electrical transport are mentioned next; the experimental techniques thus introduced are used to examine the interplay of bulk and surface contributions to the transport in thin grown Bi_2Se_3 films. Growth of thin films using molecular beam epitaxy (MBE) with atomic precision requires precise control of each flux, thus, we first discuss the flux stability in harsh oxidation conditions and derive the optimal configuration that helps grow stoichiometric thin-films. Following this, we discuss the growth of Bi_2Se_3 films on various substrates and study how this affects the electronic transport. The final work in the dissertation involves the transfer of these grown thin films to other substrates, including plastic, so as to provide a platform for future device applications.

Acknowledgements

I would like to first express my deep appreciation and gratitude to my advisor, Professor Seongshik Oh, for his invaluable guidance and continuous support throughout my graduate school career. With his limitless patience, and unfailing encouragement, he enabled me to become a researcher equipped with skills and confidence. I express my heartfelt appreciation for his advice, insights, and genuine concern throughout the course of my study.

In addition, I would like to thank my committee members, Professors Sang-Wook Cheong, Sigrid McAfee, and Weida Wu, for their valuable time and insight, which have helped me in completion of this work.

I owe a tremendous amount to Yong-Seung Kim who mentored me in my first couple of years in the lab, and who patiently, and repeatedly answered my any and all questions. I would also like to thank my labmates - Eliav Edrey, Mathew Brahle, Nikesh Koirala, Maryam Salehi, and Jisoo Moon, for creating a great learning and working environment.

Last, but not the least, I would like to thank my family for their unconditional love and trust throughout all these years. Special acknowledgements to my brother, Ritesh, who has constantly supported and encouraged me, through all the good and the bad times.

Dedication

To my father, Ram Kumar Bansal, and my mother, Asha Bansal, for always encouraging me in my passion for science. And to my wonderful brother, Ritesh, and sister-in-law, Aarti, without whose constant support, I would not have had the vigor to successfully finish this work.

Table of Contents

Abstract	ii
Acknowledgements.....	iv
Dedication.....	v
List of Figures.....	ix

Chapter 1. INTRODUCTION 1

1.1 Material Classification.....	1
1.2 Topological Band Theory.....	5
1.2.1 Quantum Hall State (QHS)	8
1.3 Topological Insulators	13
1.3.1 Theoretical Review.....	13
1.3.2 Experimental Work.....	20
1.4 Outline of the work.....	22

Chapter 2. THIN FILM GROWTH 24

2.1 Epitaxial Growth.....	25
2.1.1 Modes of Film Growth.....	26
2.1.2 Relaxation, Reconstruction, and Defects.....	29
2.2 Molecular Beam Epitaxy.....	33
2.2.1 Ultra-High Vacuum Conditions	35
2.2.2 MBE System at Rutgers University.....	39
2.2.3 Substrate Handling.....	42
2.2.4 Thermal Cell.....	44
2.3 Atomic Flux Measurement	45
2.3.1 <i>In situ</i> Quartz Crystal Microbalance.....	46
2.3.2 <i>Ex-situ</i> Rutherford Backscattering Spectroscopy	48
2.4 Reflection High Energy Electron Diffraction	49

Chapter 3. ELECTRICAL MEASUREMENT	52
3.1 Electrical Transport	52
3.1.1 Drude Model.....	52
3.1.2 Hall Effect.....	55
3.1.3 Van der Pauw and Hall Bar Geometries	56
3.2 Transport Measurement	58
3.2.1 Magnet Systems.....	58
3.2.2 Instrumentation.....	63
3.2.3 Data Analysis	66
 Chapter 4. FLUX STABILITY AGAINST OXIDATION IN OXIDE - MBE ENVIRONMENT	 69
4.1 Flux, Geometry, and Pressure Dependence	70
4.2 Crucible Aperture	79
4.3 Self-gettering Differential Pump	83
 Chapter 5. MBE GROWTH & TRANSPORT PROPERTIES OF Bi₂Se₃ ON Si (111).....	 90
5.1 Epitaxial Growth of Bi ₂ Se ₃ on Si(111).....	90
5.1.1 Substrate Preparation.....	92
5.1.2 Basic Bi ₂ Se ₃ Recipe	94
5.1.3 Film Structural Analysis	100
5.2 Thickness – dependence of Bulk Transport Properties.....	103
5.2.1 Basic Transport.....	103
5.2.2 Weak Anti - Localization	107
5.3 Conclusions	111
 Chapter 6. THICKNESS – INDEPENDENT TRANSPORT CHANNELS IN Bi₂Se₃ THIN FILMS.....	 113
6.1 Bi ₂ Se ₃ Film Growth on Al ₂ O ₃	114
6.2 Two - Channel Transport.....	116

6.2.1 Two - Carrier Model	118
6.2.2 Weak Anti-Localization.....	120
6.3 Quantum Confinement.....	122
6.4 Shubnikov de Haas Oscillations.....	127
6.5 Conclusion	131
 Chapter 7. ROBUST TOPOLOGICAL SURFACE STATES OF Bi_2Se_3 ON AMORPHOUS SiO_2/Si & AMBIPOLAR GATING EFFECT	132
7.1 Bi_2Se_3 Film Growth on SiO_2/Si	133
7.2 Transport Properties: Substrate Effect	136
7.3 Electrostatic Back - Gating.....	140
7.4 Conclusion.....	142
 Chapter 8. TRANSFERRING MBE-GROWN Bi_2Se_3 FILMS TO ARBITRARY SUBSTRATES	143
8.1 Transfer Process.....	144
8.2 Transport Analysis	148
8.3 Electrostatic Back-Gating & Metal - Insulator Transition via Dirac Gap	151
8.4 Conclusion	157
 Chapter 9. FUTURE RESEARCH	158
9.1 Review.....	158
9.2 Future Scope	159
 REFERENCES	161

List of Figures

Figure 1-1. Pictorial representation of how the ground state of a system breaks the symmetry	2
Figure 1-2. An illustration of the band theory of crystals	3
Figure 1-3. Pictorial representation of a reversible transformation process between topologically equivalent cup and a donut	5
Figure 1-4. Comparison between a band insulator and a quantum Hall state	9
Figure 1-5. Chiral edge modes at the interface between a quantum Hall state and a trivial insulator	12
Figure 1-6. Comparison of the quantum Hall state and the quantum spin Hall state	15
Figure 1-7. Scattering of a quantum spin Hall edge state by a non-magnetic impurity	16
Figure 1-8. Schematic of edge states in quantum spin Hall insulator	17
Figure 1-9. Edge states between two degenerate points, $\Gamma_a = \mathbf{0}$ and $\Gamma_b = \pi\mathbf{a}$	18
Figure 1-10. The linear dispersion at TR-invariant point forms a ‘Dirac’ cone.....	19
Figure 2-1. Accumulation modes of deposited material on a substrate surface.....	26
Figure 2-2. Possible growth modes of the deposited material for different coverage regimes	27
Figure 2-3. Reconstruction of Si (111) structure as observed in RHEED	30
Figure 2-4. A schematic illustration of different crystallographic defects	32
Figure 2-5. A schematic illustration of a typical molecular beam epitaxy system.	34
Figure 2-6. Images of various types of pumps used in a UHV chamber	38
Figure 2-7. Front overview of the MBE system at Rutgers University	40
Figure 2-8. Mounting the substrate in the load-lock chamber.....	43

Figure 2-9. Low temperature thermal cell during maintenance.....	45
Figure 2-10. Images of the QCM mounted in the MBE system.....	47
Figure 2-11. Images and schematics for in situ reflection high energy electron diffraction system mounted on the growth chamber.....	50
Figure 3-1. A schematic of the Hall effect measurement on a sample of width, W , and thickness, t	56
Figure 3-2. A schematic for different geometries used for dc transport measurement. (a) Van der Pauw geometry, and (b) Hall bar geometry.....	57
Figure 3-3. Images of the AMI liquid helium cryostat used to perform transport measurements at a temperature as low as $\sim 1.5\text{ K}$, and at up to 9 T	59
Figure 3-4. Images of the ARS cryostat used to perform transport measurements at a temperature of $\sim 5\text{ K}$, and at up to 0.6 T	60
Figure 3-5. Front interface of the variable magnetic field ramp rate LabVIEW program.....	62
Figure 3-6. Sample preparation for transport measurement.....	64
Figure 3-7. Front interface of the LabVIEW program designed to communicate with the source meters and switch matrix.....	65
Figure 3-8. A pictorial representation of the need for data symmetrisation.	66
Figure 4-1. The effects of source temperature, source-to-substrate distance, and source type (unmelted and premelted) on flux.	71
Figure 4-2. Short-term Sr-flux stability in argon and oxygen environment for different port and flux configurations.....	73
Figure 4-3. Long-term Sr-flux stability for standard and extended port.....	75
Figure 4-4. Short-term flux stability and flux transient at comparable fluxes for different depths of the source and different ports.....	77
Figure 4-5. Schematic diagram of the alumina and tantalum aperture inserts.....	80

Figure 4-6. Dependence of the short-term and long-term stability on the aperture depth at comparable flux values	81
Figure 4-7. Cross sections of different port configurations equipped with apertures and collimators	83
Figure 4-8. Effect of port apertures and collimators on short-term Sr-flux stability various flux rates.	85
Figure 4-9. Time dependence of oxygen pressure near Sr source at standard port and extended port with various configurations	87
Figure 4-10. Normalized long-term flux stability for the extended port with collimator and standard port with/without port aperture, differential pumping.....	88
Figure 5-1. RHEED patterns for different stages in the growth of Bi_2Se_3 on Si(111) substrate	95
Figure 5-2. Evolution of the specular beam intensity during Bi_2Se_3 growth at different temperatures	97
Figure 5-3. Evolution of RHEED pattern on the surface from Si(111) 1×1 structure obtained by Se exposure at low temperature to the Bi_2Se_3 thin film grown by the two-temperature growth process.	99
Figure 5-4. Structural characterization of Bi_2Se_3 films grown on Si(111).	102
Figure 5-5. Thickness dependence of the transport properties of Bi_2Se_3 thin films grown on Si(111)	104
Figure 5-6. Normalized magnetoresistance for different thickness Bi_2Se_3 films grown on Si(111)	107
Figure 5-7. Weak antilocalization effect observed in Bi_2Se_3 on Si.....	109
Figure 6-1. RHEED and AFM images showing the steps of Bi_2Se_3 growth on sapphire substrates	115
Figure 6-2. Transport properties of Bi_2Se_3 films grown on Al_2O_3 as a function of thickness	117
Figure 6-3. Hall conductance data fitted with the two-carrier model.....	120

Figure 6-4. Normalized magnetoresistance for different thickness Bi_2Se_3 films grown on Al_2O_3 .	121
Figure 6-5. Schematic of k-space energy dispersion on a Bi_2Se_3 surface and band-bending near the surface	124
Figure 6-6. A schematic showing how the quantized 2DEG levels in the accumulation layers are affected by the film thickness when the surface Fermi level is pinned	125
Figure 6-7. SdH measurements on Bi_2Se_3 thin films as a function of sample thickness	128
Figure 7-1. Evolution of RHEED pattern during growth of Bi_2Se_3 film on a- SiO_2 substrates.	134
Figure 7-2. XRD, ARPES and STEM images of Bi_2Se_3 films on a- SiO_2 substrates	135
Figure 7-3. Comparison of transport properties of Bi_2Se_3 films grown on a- SiO_2 with those on Si(111) and $\text{Al}_2\text{O}_3(0001)$ (c and d) ($T = 1.5$ K, $B = \pm 0.6$ T)	138
Figure 7-4. Electrostatic back-gating of an 8 QL Bi_2Se_3 film on a- SiO_2 /doped-Si substrate ($T = 6$ K, $B = \pm 0.6$ T)	141
Figure 8-1. Process for transfer of Bi_2Se_3 thin films grown on a- SiO_2 or $\text{Al}_2\text{O}_3(0001)$ to any arbitrary substrate	145
Figure 8-2. Structural characterization of the transferred Bi_2Se_3 film using AFM and TEM	147
Figure 8-3. Transport properties of Bi_2Se_3 films transferred to different substrates	149
Figure 8-4. Electrostatic back-gating of ultrathin transferred films	153

Chapter 1. INTRODUCTION

1.1 Material Classification

The understanding of materials has always been at the forefront of advancements in human technology. All materials contain electrons – interaction of these electrons with ion cores results in clustering of electrons in energy bands separated by regions of energy that prohibit presence of any electronic state. Insulating state occurs when the allowed energy bands are either completely filled or completely empty, forbidding movement of electrons under an applied electric field; whereas conducting state occurs when one or more bands are partially filled. Based on this understanding, materials were initially categorized as electrically conductive or insulating; then based on quantum theory and other scientific breakthroughs came yet another set of classification like semiconductors and superconductors, ferromagnets and antiferromagnets, and many others.

The idea of symmetry is the underlying principle in fundamental laws of physics. Using Landau's approach of phase transitions, different states are classified

by the symmetries that they spontaneously break. Order parameters associated with these symmetries acquire a finite expectation value, and different values for these parameters distinguish between different states. The most commonly observed example is crystallization of solids through electrostatic interactions (Fig. 1-1a,b). To gain an energetically favorable ground state, the translational invariance of atoms placed at random locations is broken and replaced by lattice vector. Another much studied example is ferromagnetism, with localized magnetic moments ordered along some chosen direction; various types of magnetic ordering are possible resulting in antiferromagnetism, ferrimagnetism etc. However, in all cases, the global rotational invariance or the rotational symmetry of the spin, usually obeyed by magnetic interactions in solids, is broken to observe such ordering. (Fig. 1-1c,d).

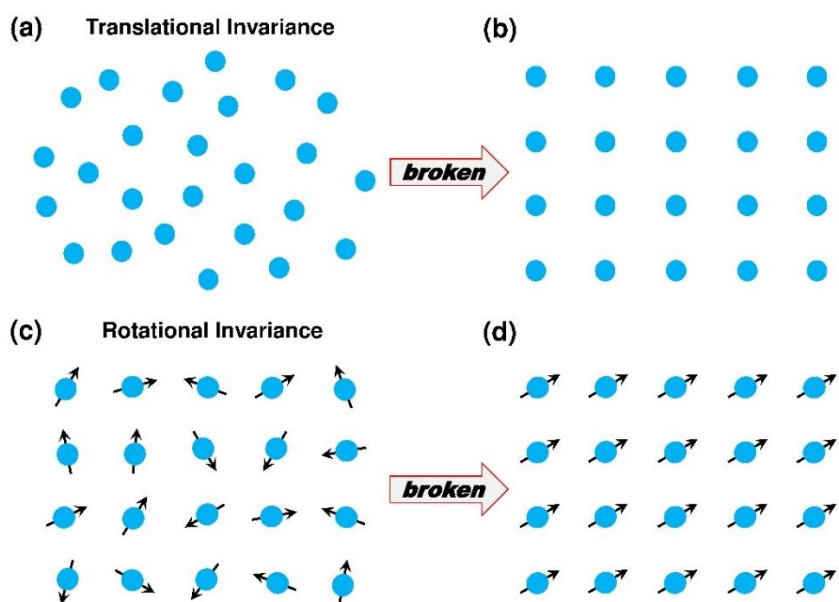


Fig. 1-1. Pictorial representation of how the ground state of a system breaks the symmetry. **(a)** The translational invariance of atoms placed at random locations, **(b)** is broken to crystallize into a lattice. **(c)** The magnetic interaction does not break the rotational invariance. **(d)** The ground state of ferromagnetic interaction is formed by breaking the rotational invariance of magnetic moments to line up in the same direction.

In free space, the electrons behave as independent particles, and thus, follow the Newtonian physics, taking the continuous range of energy with $= p^2/(2m)$. However, once placed in a crystal, these electrons are under the influence of a periodic background potential due to the ion cores, thus diverting from the free electron model. Similar to interference pattern formed by light on a diffraction grating, the electron-lattice interaction results in destructive and constructive interference along certain crystal directions. The electrons that destructively scatter become localized, resulting in the continuous energy band (from classical model) to be split into a spectrum of energy bands separated by regions of forbidden energy, or the band gap, where no electron orbitals exist (Fig. 1-2).

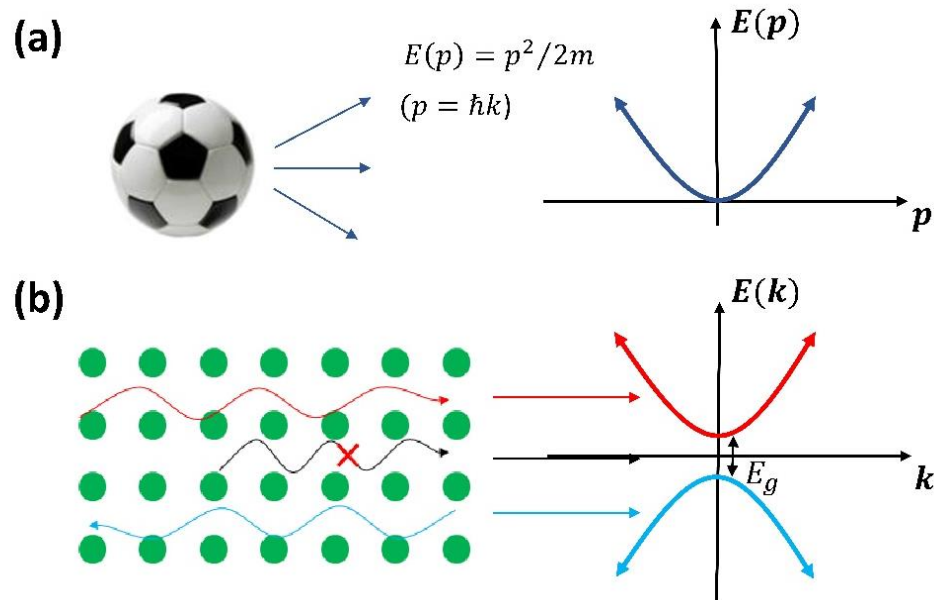


Fig. 1-2. An illustration of the band theory of crystals. **(a)** For classical objects, or quantum-mechanical objects in free space, the energy states form continuous states. **(b)** Destructive interference caused by the periodic potential introduced by crystal lattice induces certain forbidden energy gaps in the otherwise energy continuum. (Adapted from ¹Brahlek, 2014)

The electronic properties of the material are determined by how the electrons, constrained to these allowed energy levels, respond to an applied electric field. As per Fermi-Dirac distribution, under the assumption of thermodynamic equilibrium and negligible mutual interaction, the electrons start filling from the lowest energy level and continue filling higher levels until all electrons are accommodated. The energy of this topmost filled level in the ground state (or at absolute zero) is called the Fermi level (E_F). If E_F falls inside the forbidden band gap, resulting in energy bands that are either completely filled or completely empty, the material would be an insulator and will allow charge to flow only if the applied electric field is large enough to disrupt the electronic structure, thus exciting an electron from the completely filled band below (the valence band, VB) to the completely empty band above (conduction band, CB). On the other hand, the material will be metallic in case the E_F falls inside an energy band, thus, leaving the band partially filled; here, any arbitrarily minute electric field is enough to enable the conduction to occur. As an example, the free space can be considered as an insulator with a band gap of $\sim 1 \times 10^6$ eV, which is the excitation energy required for production of free charges, or the electron-positron pair, required for charge to flow. In contrast, in the case of plasma, there are free electrons floating around, giving the vacuum a metallic nature.

Recent work in theory of insulators (²Kane *et al.*, 2005; ³ Kane *et al.*, 2005) showed that systems can be classified by not only the symmetries they break, but also the symmetries, such as time-reversal, charge conjugation, or chiral symmetries, that they preserve to ensure the stability of the state. The following section discusses how the topological order can be used to classify various insulating states.

1.2 Topological Band Theory

Topological band theory is the study of the gapped electronic band structure of a system based on the topology of the occupied bands. Mathematically, topology is concerned with properties of objects (or topological spaces) based on the broad details that are not sensitive to adiabatical changes, especially under invertible transformations. Topology is associated with the problems that depend on how an object is put together, and not the exact shape involved, bringing forth the notion of topological equivalence, which is understood as objects (for example – a cup and a donut, as seen in Fig. 1-3) being able to be deformed into the other without involving a non-reversible transformation such as cutting or gluing.



Fig. 1-3. Pictorial representation of a reversible transformation process between topologically equivalent cup and a donut. (Adapted from ⁴Hood, 2016)

Gauss and Bonnet typified this equivalence by defining a single quantity, insensitive to adiabatical transformations, called the topological index or the genus

of the object (or surface), or the number of “holes” an object has (⁵Nakahara, 1990). In terms of topology, a ball and a bat are equivalent with a genus of 0 or no holes; while the same ball (genus = 0) is different than a donut (genus = 1). In this context, slow and smooth changes constitute adiabatic deformations, while drastic non-reversible transformations include actions such as tearing, or gluing. This can be further exemplified by classification of the ten Hindu-Arabic numerals into three classes – Class I (genus = 0): [1,2,3,5,7], Class II (genus = 1): [4,6,9,0], and lastly class III (genus = 3): [8]. All the objects within each class can be transformed to another within the same genus under a continuous deformation (topologically equivalent – e.g. ‘4’ can be deformed to make ‘6’), but a ‘dramatic’ mathematical change is required to switch genus class, i.e. filling in a hole or poking a new hole (topologically different – e.g. ‘0’ can be deformed to ‘8’ only if a hole is made).

This general idea of categorizing 3D objects by a topological index can be extended to more abstract space, such as Hilbert space. The role of geometric shape or the Gaussian curvature is replaced by the characteristics of the wave function of the electrons. Topological equivalence is defined in terms of the ordering of the energy bands – for example an atomic insulator, such as Ar, and a semiconductor can be broadly considered topologically equivalent, as one can adiabatically tune the Bloch Hamiltonian between the two without closing the energy gap. The term topological, here, implies the existence of a bulk invariant, $n \in \mathbb{Z}$ (\mathbb{Z} denotes the integers) called the Chern invariant, that differentiates between phases of matter having the same symmetry.

The Berry Phase (Berry, 1984), derived from the general idea that under slowly varying fields, quantum adiabatic transport could modify the wavefunction by a geometric phase in addition to the conventional dynamic phase, acquired due to the geometrical properties of the parameter space of the Hamiltonian, is an important concept in topological band theory. When the amplitude and phase parameters of the wave function are simultaneously changed over a closed path (or a loop) and brought back to the initial configuration, it is possible that the states at t and $t + dt$ are not identical, this discrepancy gives rise to the gauge-invariant Berry phase. For a system, where the energy levels are singly degenerate, the sum over the Berry phase of all energy levels is zero, showing that the sum of all filled bands can only have zero Berry phase. In case of a gapless Dirac fermion in 2 dimensions, the Berry phase acquired by the eigenstates going around the Fermi surface equals π .

The Berry curvature is gauge invariant, and derived from the geometric properties of Bloch wave functions, $|u_m(k)\rangle$, associated with an energy band. The degeneracy points in parameter space act as sources and drains of the Berry curvature. The Berry curvature integrated over a closed manifold is 2π times the net number of monopoles contained inside. Similar to the concept of genus for geometrical shapes, Berry curvature integrated over a 2-D Fermi surface (in 3-D metals) gives an integer topological index, in units of 2π , called the Chern number. The Chern invariant is the total Berry flux in the Brillouin Zone, and cannot change when the Hamiltonian varies smoothly. In filled bands in two dimensions, the integral of the Berry curvature over the full 2-D Brillouin zone is related to the Hall conductance of the insulator and defines the topological class of an insulator. The

total Chern number, summed over all occupied bands is an invariant, provided the gap separating the occupied and empty bands is finite. For, conventional band insulators, such as vacuum, the total Chern number (sum of the integrals of all filled bands) is zero, and the insulator is topologically trivial.

1.2.1 Quantum Hall State (QHS)

Unlike other physical systems, the properties to be observed for the existence of topological states is not just the symmetries being broken, but the symmetries, such as time reversal, charge conjugations, or chiral, that must be preserved in order to maintain these states. Before moving to topological insulators, the simplest example of topological material, quantum Hall state (QHS) will be briefly discussed. The quantum Hall effect was first reported for a two-dimensional electron gas (2DEG) in the inversion layer of a silicon MOSFET (Klitzing *et al.*, 1980).

Classically, the motion of a free charged particle in a magnetic field is a combination of circular cyclotron motion in the plane perpendicular to the applied magnetic field and a free motion parallel to it. On the other hand, quantum-mechanically, the motion of the charged particle perpendicular to the magnetic field is quantized and the free-particle kinetic energy, $= \hbar^2 k^2 / 2m$, is converted into sub-bands, corresponding to a given Landau level (Fig. 1-4).

When the free electron gas is confined to two dimensions by means of appropriate semiconductor interfaces or metal-oxide-semiconductor interfaces etc, the carriers behave as free moving parallel to the planar structure, but are strongly

localized in a thin layer of atomic planes next to the interface. When a magnetic field is applied perpendicularly to such 2DEG, the free electrons within feel the Lorentz force, and begin making cyclotron orbits, with a cyclotron resonance frequency of $\omega_c = eB/m$, and the energy levels are quantized, taking discrete values as $E_n = (n + 1/2)\hbar\omega_c$, where B is the applied magnetic field, and $n = 0, 1, 2, \dots$ indicate the Landau level, and the energy separation between adjacent Landau levels is $\hbar\omega_c$. To prevent the dispersion of these Landau levels, $\hbar\omega_c$ must exceed the random thermal energy. For a free electron in three dimensional gas, the energy of the Landau levels can be obtained by taking into account the free motion parallel to the direction of the applied magnetic field, $E_{nk_z} = \left(n + \frac{1}{2}\right)\hbar\omega_c + \frac{\hbar^2 k_z^2}{2m}$.

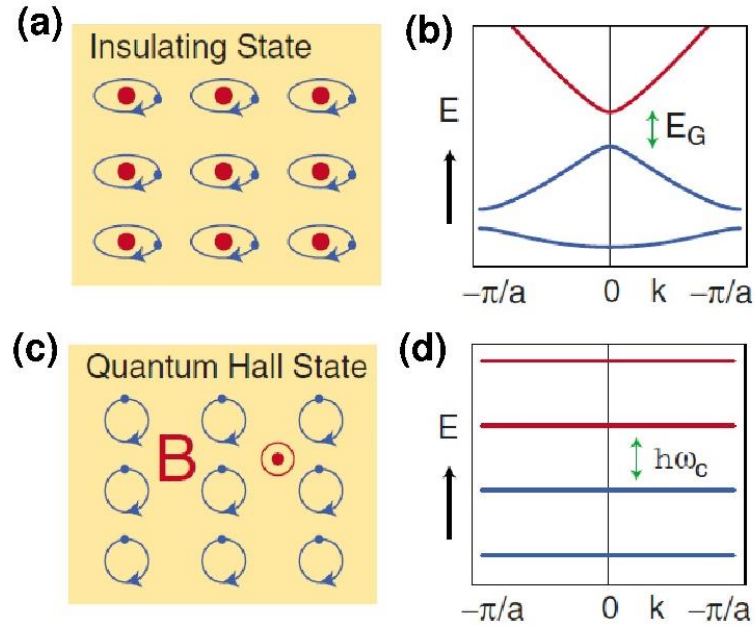


Fig. 1-4. Comparison between a band insulator (a-b) and a quantum Hall state (c-d). **(a)** Pictorial description of electrons being localized around atoms, and **(b)** the corresponding band structure. In an atomic insulator, the Fermi level sits in the bulk band gap. **(c)** The cyclotron motion of electrons in the QHS with electrons localized around magnetic flux lines, and **(d)** the Landau levels, viewed as a corresponding band structure, where the energy bands are separated by the cyclotron energy, $\hbar\omega_c$. (Adapted from ⁸Hasan and Kane, 2010)

The transport properties of two-dimensional conductors, when observed in high purity samples, at very low temperatures and strong magnetic fields, show that the parallel component of the electric resistance, $\rho_{xx}(H)$, becomes vanishingly small, while quantum Hall effect emerges as a sequence of flat plateaus in the Hall resistance, $\rho_{xy}(H)$, as a function of applied magnetic field. As is seen in the energy relation above, in the absence of a periodic potential, the energy of a level depends only on n , and not k , implying that the states with same n , but different k are degenerate; this degeneracy gives rise to δ -functions, called Landau levels. If Fermi level falls between $(n - 1)^{th}$ Landau level completely filled, and the n^{th} Landau level completely empty, the system behaves as an insulator. However, unlike an atomic insulator, an electric field causes the cyclotron orbits to drift, leading to a quantized Hall conductivity, $\sigma_{xy} = ne^2/h$. The Chern number is also quantized to an integer value, corresponding to the number of total filled Landau levels.

Now, a question arises as to why there is a non-zero Hall conductance in a quantum Hall insulator (QHI), even though the Fermi level is in the gap. The answer lies in the fact that edges are formed in the system, such as by making contacts for any measurement, resulting in gapless edge modes traversing the bulk gap. These gapless edge states are a fundamental aspect of Topological Insulators (TI), and the triviality or the non-triviality of an insulator depends on the presence or absence of edge states.

Extending this concept, another question to ask is what happens to these states if the QHI (Chern number $\neq 0$) is bounded by other trivial insulator (Chern number $= 0$). To answer this, let's consider two insulators, with different values of

Hall conductance (zero or non-zero), close to each other such that away from the interface, the two samples extend to $\pm\infty$, respectively. (For the samples in D dimensions, the interface would be in D-1 dimension space). Since Hall conductance is an integer characterizing the phase of the system, and because this cannot be changed unless the bulk gap collapses and then reopens, it can be seen that the only way the charge symmetry of the system is preserved is that the interface between the two insulators must have a gap-closing and re-opening, or an edge mode crossing the Fermi level, at some point on it. In absence of such state, the whole space would be gapped, implying that the Hall conductance is same throughout, thus, invalidating the initial assumption. As can be seen in Fig. 1-5, the edge-confining potential cause the bulk states, deep in the valence band, to rise up in energy, and thus forming gapless edge modes. Halperin first studied these edge states at the interface between vacuum and the integer quantum Hall state (⁹Halperin, 1982). These edge states are insensitive to disorder in the absence of any state available for backscattering, and are chiral in the sense that they propagate along one direction.

The development of this ‘faux metallicity’ is a direct consequence of the topology of the materials (¹⁰Thouless *et al.*, 1982) through the bulk-boundary correspondence theorem which states that at the interface between materials described by different topological invariants (Chern number for right and left as N_R and N_L , respectively), the number of modes in the gapless metallic states is simply the difference in the Chern number across the interface ($\Delta n = N_R - N_L$) (⁸Hasan *et al.*, 2010). The topologically non-trivial QHS requires a large magnetic field to push it into an insulating state; Haldane later realized QHE in systems without an external

magnetic field, and proposed a model for spinless fermions in a two-dimensional honeycomb lattice. In early turn of the millennium, Kane and Mele extended the Haldane model to include spin degree of freedom, and thus, making the magnetic field spin-dependent. Immense work was done to observe non-trivial topological phase in an absence of external magnetic field, led by C. L. Kane (³Kane and Mele, 2005; ²Kane and Mele, 2005; ¹¹Fu and Kane, 2007; ¹²Fu *et al.*, 2007), S-C. Zhang (¹³Bernevig *et al.*, 2006; ¹⁴Bernevig and Zhang, 2006; ¹⁵Qi *et al.*, 2006; ¹⁶Qi *et al.*, 2008), and J. E. Moore and L. Balents (¹⁷Moore and Balents, 2007), which became a pioneer in the developing field of TI.

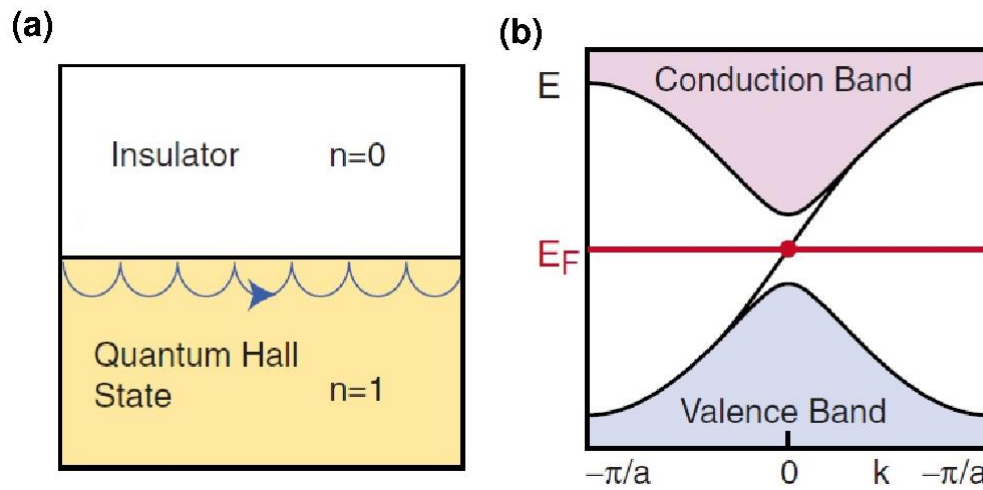


Fig. 1-5. Chiral edge modes at the interface between a QHS and a trivial insulator. **(a)** The skipping motion of electrons as their cyclotron orbits bounce off the edge, and **(b)** the corresponding band diagram – a single edge state, bound to the edge, connects the bulk valence band to the bulk conduction band. (Adapted from ⁸Hasan and Kane, 2010)

1.3 Topological Insulators

1.3.1 Theoretical Review

1.3.1.1 Quantum Spin Hall State (QSHS)

For any experimentally observable system, one of the most important property is its behavior on time-reversal (TR), or a transformation that reverses the arrow of time, $T : t \rightarrow -t$. The idea of time-reversal symmetry can be understood by considering the motion of charge particles in a magnetic field – on reversing the ‘arrow of time’, i.e., reversing the direction of motion, the path traversed by the particle is not retraced, thereby breaking the TR symmetry. In an absence of an external magnetic field, spin-orbit coupling (SOC) allows a different topological class of insulating band structure where TR symmetry is unbroken.

The topologically non-trivial insulators can be further divided into two broad classes based on whether TR symmetry is preserved or not. The QHS is a topological insulator state that, by virtue of observing non-zero Hall conductivity, violates the TR symmetry. In 2001, Zhang, and Hu introduced the first model of a TR-invariant topological insulator (¹⁸Zhang *et al.*, 2001). Murakami, Nagaosa, and Zhang developed the theory of intrinsic spin Hall effect based on a system with strong SO coupling, and then extended the theory to TR-invariant insulators (¹⁹Qi *et al.*, 2010). Quantum spin Hall effect (QSHE) was first studied in 2D in graphene with spin orbit interactions generating an energy gap (³Kane *et al.*, 2005). In an applied electric field, the up-spin and down-spin electrons flow in opposite directions, leading to a net zero Hall

conductivity, but there is a quantized spin Hall conductivity. This phase distinguishes itself from the spin Hall effects observed in 3-D systems in that it leads to a phase that is topologically distinct from a band insulator. This system is gapped in the bulk but supports both spin and charge transport at the boundaries. These counter-propagating edge modes with opposite spin orientation, defined as quantum spin Hall (QSH) states, are non-chiral, but are also insensitive to disorder because their directionality is correlated with spin, i.e. if the sign of the momentum is flipped, the spin gets flipped as well.

In a simplistic scenario, in one-dimension, electrons can either flow forward (say, spin up) or backward (spin down), and any random disorder can lead to scattering and thus resistance. Now, consider QHS in a 2DEG under strong applied magnetic field, Fig. 1-6a, charge transport occurs along the edge channels with the forward and backward motion being spatially separated, with each edge containing half the degrees of freedom. As shown in the figure, in absence of any back-scattering channel, the charge simply moves around an impurity without scattering, resulting in robust channels.

Fig. 1-6b shows the case for a TR-invariant system, the channels for transport are split into forward-moving and backward-moving for both spin-up and spin-down electrons. Such a system is said to be in QSH state because it satisfies the zero charge conductivity constraint imposed by the TR symmetry, with a net forward spin transport along the top edge and converse along the bottom edge. One might think that having two channels along the edge will result in more scattering, however

such a scenario is prohibited by the TR symmetry, and electron propagation is immune to backscattering from a non-magnetic impurity. Unlike general semiconductor, the only path available (due to large SOC) for an electron to scatter into involves circling around the impurity in either clockwise or anti-clockwise direction.

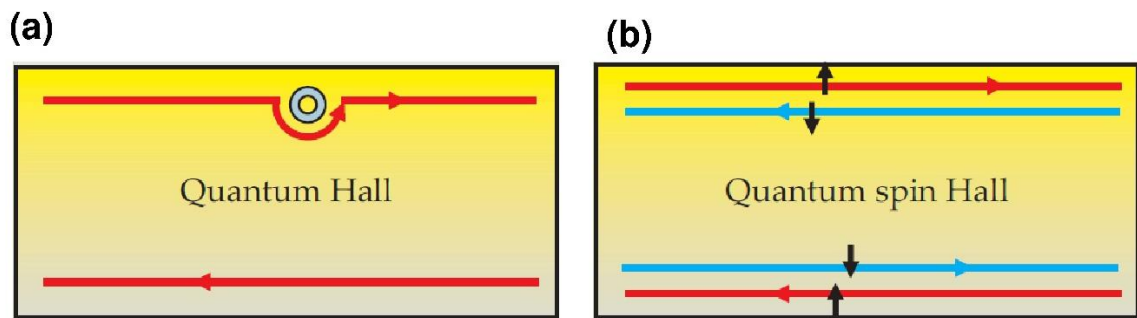


Fig. 1-6. Spatial separation is important for both QH and QSH states. **(a)** In a QH ‘bar’, the upper edge has only forward moving, spin-up electrons, and the lower edge has the backward moving spin-down electrons. **(b)** For the QSH ‘bar’, upper edge modes allow both – a forward motion of spin-up electrons and a backward motion of spin-down electrons, and the converse for the lower edge. (¹⁹Adapted from Qi and Zhang, 2010)

As shown in Fig. 1.7, the spin rotates by either π or $-\pi$, resulting in a net difference of $\pi - (-\pi) = 2\pi$ between the two paths. Thus, the two backscattering paths always interfere destructively leading to perfect transmission. In case of a magnetic impurity, however, the TR symmetry is broken, leading to scattering. However, this concept leads to another constraint that there be an odd number of forward and backward moving channels. In case of an even number, the impurity can easily scatter an electron from a forward- to a backward- moving channel without reversing its spin, causing dissipation.

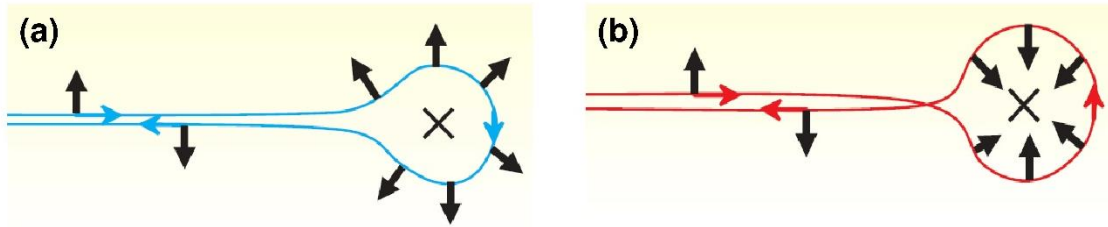


Fig. 1-7. Scattering of a QSH edge state by a non-magnetic impurity – due to SOC, the spin of the electron is locked perpendicular to the momentum. **(a)** going clockwise, the spin rotates by π . **(b)** going anticlockwise, the spin rotates by $-\pi$. A quantum mechanical phase difference of -1 between the two paths lead to destructive interference resulting in zero amplitude for back scattering. (Adapted from ¹⁹Qi and Zhang, 2010)

Both QSH state and an ordinary insulating state have a gapped bulk, but QSH state have edge states that traverse the energy gap in pairs – so what happens when a QSH state meets an ordinary insulating state? Similar to that in the case of QH state, at the interface, the energy gap closes, allowing the edge states to exchange electrons. As seen in Fig. 1-8b, these QSH edge states are half an ordinary 1D conductor in the sense that up-spins propagate in one direction, while down-spins in other, giving QSH edge states a robustness against disorder.

TR symmetry is represented by an anti-unitary operator, Θ , such that $\Theta^2 = -1$. This leads to the constraint that the states need to be doubly degenerate at TR-invariant points in the Brillouin zone (Kramer's theorem). The equivalence classes of Hamiltonians satisfying the constraint, $\Theta H(k) \Theta^{-1} = H(-k)$, can be classified as those that can be smoothly deformed without closing the energy gap (⁸Hasan *et al.*, 2010). Although any TR-invariant perturbation may destroy the quantization of the spin Hall conductance, Kramer's theorem prevents from opening a gap at the edge due to the perturbations, thus QSH state does not necessarily imply a quantized value of spin Hall conductivity (²Kane *et al.*, 2005).

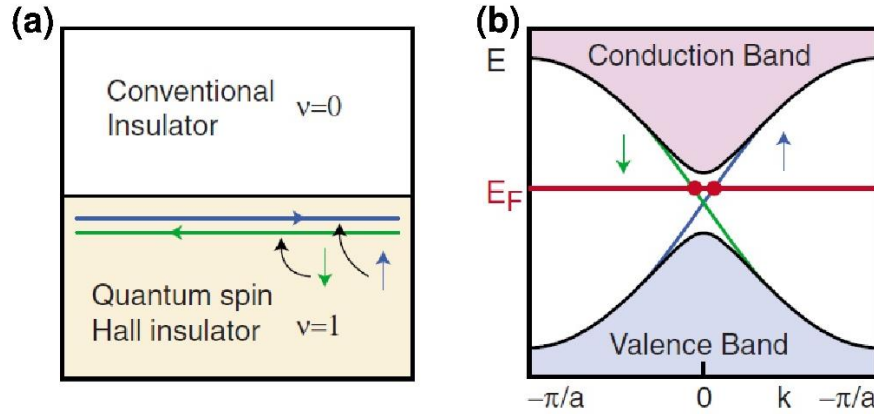


Fig. 1-8. Schematic of edge states in QSHI. **(a)** Interface between a topologically trivial, conventional, insulator and a topologically non-trivial, QSH, insulator. **(b)** The edge states are non-degenerate with up-spin and down-spin electrons propagating in opposite directions. (Adapted from ⁸Hasan and Kane, 2010)

In absence of any SO interactions, the conduction and valence bands are degenerate and the degeneracy arises due to spin-up and spin-down states. Even though SO interaction (acting like a magnetic field), splits the spin-up and spin-down states, Kramer's theorem requires the band overlap at TR invariant moment, i.e. at $k_x = 0, \pm \pi/a$, as seen in Fig. 1-9.

For the case where the edge states are connected in a pair and cross E_F at even number of points, (Fig. 1-9a), the system can be adiabatically deformed to a situation where no bands cross E_F , leading to a topologically trivial insulating state. On the other hand, for a staggered connection (Fig. 1-9b), where the edge states cross E_F at odd number of points, as long as TR symmetry is preserved, under no adiabatic deformation the edge states can be completely removed, defining a non-trivial topological insulating state. This classification of insulators, based on even or odd number of edge modes intersecting the Fermi level for a robust QSH state, leads to define another topological invariant, called Z_2 topological invariant. This topological

invariant can only be either 0 or 1. Thus, the QSH edge state is robust as long as TR symmetry is preserved, and there are an odd number of edge modes.

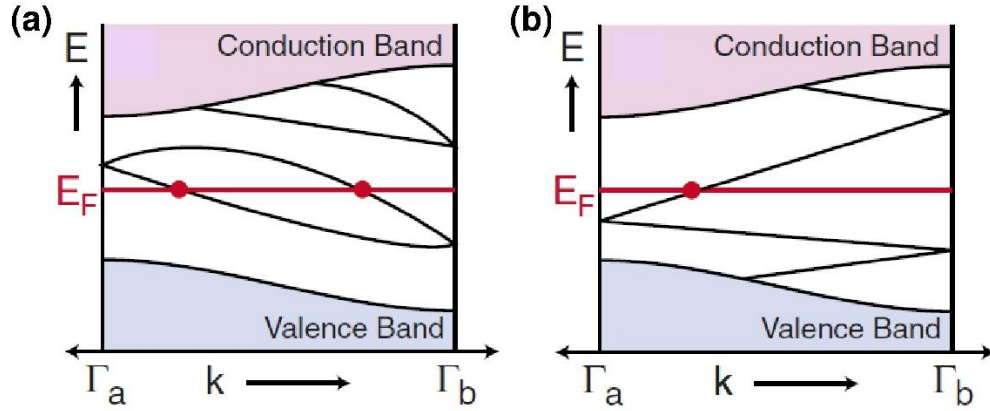


Fig. 1-9. Edge states between two degenerate points, $\Gamma_a = 0$ and $\Gamma_b = \pi/a$. (TR symmetry gives $k = -k$, thus, only $k > 0$ is shown.) **(a)** The number of states crossing E_F is even, and can be adiabatically tuned similar to a trivial insulator. **(b)** Odd number of states crossing E_F results in a non-trivial insulating state with metallic edge states. (Adapted from ⁸Hasan and Kane, 2010)

1.3.1.2 Topological Surface States (TSS)

The concept of Z_2 topological insulators can be generalized to 3D TI, where the boundary transport occurs in 2-D surface states (SS). As seen from Fig. 1-9, near the TR-invariant momentum, at $= 0, \pm\pi/a$, the dispersion of the edge states is linear, $E \propto k$, similar to that obtained from Dirac equation for a massless relativistic fermion in 1D. Generalizing for a 3D TI, the 2D energy-momentum relation takes a conical shape with the tip of the cone at TR-invariant point, known as Dirac cone, see Fig. 1-10. Due to the strong SOC, the electron spin is locked perpendicular to its momentum, leading to a phenomenon termed as spin-momentum locking. TR symmetry is preserved in the sense that time reversal switches both the direction of the propagation and the direction of the spin. Since TR symmetry requires the states having opposite spins at momenta k and $-k$, the spin must rotate around the Fermi

surface with change in k (Fig. 1-10), thereby gaining a nontrivial Berry phase (of 0 or π). The spin of an electron going around a Dirac point rotates by 2π , resulting in a π Berry phase.

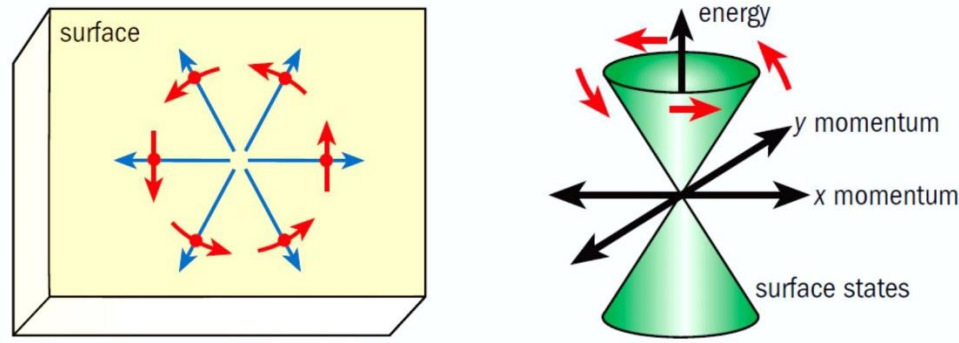


Fig. 1-10. The linear dispersion at TR-invariant point forms a ‘Dirac’ cone. The electronic motion is free along the surface, but due to spin-momentum locking, the electron’s motion determines the spin direction. (²⁰Adapted from Kane and Moore, 2011)

There are four TR-invariant points on the surface Brillouin zone, where Kramer’s degeneracy dictates that any SS present must be degenerate. The Fermi circle on the surface encloses these Dirac points, and a Z_2 topological invariant is characterized by the even or odd numbers of Kramers degenerate Dirac points being enclosed by the surface Fermi circle. For the Z_2 topological invariant value of zero, the Fermi circle encloses an even number of Kramers points, and the system is called a weak topological insulator; the TR symmetry does not protect these surface states. Conversely, in the case of odd number of Kramers points, the Z_2 topological invariant is 1, and the topological insulator is said to be strong. The SS for a strong TI forms a unique 2D topological metal with the spin non-degeneracy making it like ‘half’ a 2D conductor.

1.3.2 Experimental Work

The QSH insulator is also known as 2D topological insulator. 2D TI were first predicted to exist in graphene (³Kane *et al.*, 2005), and in 2D semiconductor systems with a uniform strain gradient (¹⁴Bernevig *et al.*, 2006). Graphene makes an interesting system to study QSH state since the conduction and valence band in graphene touch each other at two points in the Brillouin zone. 2D TI was then predicted to exist in HgCdTe quantum well structures (¹³Bernevig *et al.*, 2006), which was then later realized (²¹König *et al.*, 2007). In certain heavy elements, such as Hg and Te, the SOC is so large that the usual ordering of the conduction band (*s*-orbitals) and valence band (*p*-orbitals) is inverted, and thus changing the Z_2 topological invariant from 0 to 1. Mercury telluride quantum wells are made by sandwiching the material between cadmium telluride layers, with a similar lattice constant but much weaker SOC. As the thickness of HgTe layer is increased, the net SOC of the system is also increased, slowly pushing the *p*-orbital above the *s*-orbital band, causing a completely inverted band at a thickness of ~ 6.5 nm.

In 2008, (²²Hsieh *et al.*, 2008) reported the first 3D TI in $\text{Bi}_{1-x}\text{Sb}_x$ system, using angle-resolved photo emission spectroscopy (ARPES) to map the surface bands, where the sample is illuminated by high energy photons (X-rays) and the emitted electrons are collected by a detector to further analyze. The core electrons will have lower kinetic energy than the valence electrons, thus depending on the energy of the emitted electron, information about the orbital previously occupied by the electron is obtained. Similarly, electrons with different momentum will escape at different

angles, thus providing with momentum information. Using the work function of the materials and the information on energy and momentum of an electron provided by ARPES, a clear picture of band dispersion and Fermi surface can be obtained. By looking at the perpendicular component of the momentum, k_z , one can also determine the dimensionality – whether the electron originated from a 2D or a 3D state. This surface sensitive technique is widely used for study of topological insulators where interesting phenomena occur at the surface.

Bismuth is a semi-metal with strong SOC. Pure bismuth has a band structure with overlapping valence and conduction bands near the TR-invariant points in the Brillouin zone. In the $\text{Bi}_{1-x}\text{Sb}_x$ system, substituting bismuth with antimony changes the critical energies of the band structure; at $x \sim 0.4$, the energy gap closes and a massless Dirac point is realized. As x is further increased, the energy gap reopens with an inverted ordering.

Unfortunately, the SS in the $\text{Bi}_{1-x}\text{Sb}_x$ system were very complicated with a small band gap, prompting researchers to look for other classes of materials with a simpler surface spectrum. This led to the discovery of the so-called ‘2nd generation’ TIs, previously known as excellent thermoelectric materials, bismuth telluride (Bi_2Te_3) and bismuth selenide (Bi_2Se_3) as topological insulators using ARPES (²³Chen *et al.*, 2008; ²⁴Xia *et al.*, 2009) and scanning tunneling microscopy (STM) (²⁵Roushan *et al.*, 2009).

Bismuth chalcogenides, well known semiconductors with strong spin-orbit coupling, have a relatively larger bulk energy gap and a simplistic surface structure

containing a single Dirac cone per unit cell on the surface of Brillouin zone. Among the possible Bismuth chalcogenides being studied as TI, Bi_2Se_3 is the most extensively studied one because of its topologically non-trivial energy gap of 0.3 eV and a more accessible Dirac point at $k = 0$, almost in the center of bulk band gap. Another important feature is that $\text{Bi}_2(\text{Se},\text{Te})_3$ are stoichiometric and can be prepared with higher purity, which is important since experimental probes, including ARPES, are clearer in high-purity samples. Although the simpler surface band structure and a relatively large band gap make Bi_2Se_3 an attractive system to study, it was realized that the grown bulk crystals have high defect densities (including Se vacancies) to make the bulk conduction (in parallel to surface conduction) overwhelm the TSS signature. Thus, major effort is being made to make the bulk more insulating and move the Fermi level closer to the Dirac point.

1.4 Outline of the work

From the Stone Age to the Silicon era, our ability to control materials has been integral in shaping of our society throughout history. Recent advances in thin-film growth techniques allow materials to be designed atomic-layer by atomic-layer. The goal of this work is to bridge the gap between fundamental understandings of the physics of condensed matter systems to the practical applications.

In this work, we study bismuth selenide (Bi_2Se_3) as a topological insulator. The thin film growth and characterization techniques are discussed next in Chapter 2 with electrical measurement details in Chapter 3. Thin Bi_2Se_3 films for the study are grown using molecular beam epitaxy (MBE). To do a qualitative study, it is imperative

these films are grown in a desired stoichiometry with precise control over the various elemental layers, under all ambient conditions. Thus, we will devote some time to study various configurations in the MBE system, and determine how to maintain a steady flux rate over the growth duration (Chapter 4). Equipped with the tools to engineer a stoichiometric film, we then grow high quality Bi_2Se_3 thin films on silicon, sapphire and silicon-dioxide substrates, and study the electronic properties of these films (Chapter 5-7). Both bulk and surface channels contribute to the conduction and these contributions are also discussed in detail. In an attempt to make use of these films as devices for any future applications, we transfer these films to various other substrates, and study the change in transport properties as a result in Chapter 8; and then some concluding remarks in Chapter 9.

Chapter 2. THIN FILM GROWTH

In the realm of solid state physics, experimental probes coupled with mathematical models help in understanding both macroscopic and microscopic physical properties of matter, especially crystalline solids that host a myriad of exotic phases within themselves. The study of these electronic properties relies on synthesis of high quality crystalline samples, either in the form of bulk crystals, thin films, nanorods/nanoribbons, or nanocrystals, with the net sample size ranging from macroscopic to nanoscopic in one or all dimensions. Curiously, the same material can show different physical properties depending on whether the study is conducted on a bulk crystal or a nanoscopic structure. An interesting example would be iron selenide (FeSe) which exhibits superconducting transition at $\sim 9\text{ K}$ macroscopically, but when monolayer of FeSe is grown on SiTiO_3 substrates, the superconductivity can be noted at a temperature as high as $\sim 100\text{ K}$. In this work, our main focus is on the growth of thin film crystals using molecular beam epitaxy (MBE). In this chapter, the crystal growth and characterization techniques are briefly introduced; the instrumental set-up of a MBE system is addressed in section 2.2.

2.1 Epitaxial Growth

The origin of the term epitaxy lies in the ancient Greek words, *epi*, meaning 'onto', and *taxis*, meaning 'arranging' or 'ordering'. Thus, epitaxy refers to an oriented overgrowth of deposited material onto the surface of a suitable substrate; the overlayer thin film being referred to as epitaxial film or epitaxial layer. With the substrate acting as a 'seed crystal', if the material deposited is the same as the substrate, the process is termed as homoepitaxy. Heteroepitaxy refers to the epitaxial growth where the deposited thin film and the employed substrate are of different materials, for example – GaAs being deposited on Si. The growth mechanism is heavily influenced by surface kinetics and surface chemistry, affecting both impurity incorporation and defect generation.

The growth process starts with the creation of atomic/molecular flux; once reaching the heated substrate, a portion of the atoms in the flux is weakly adsorbed to the surface, mostly by van der Waals attraction. These adatoms are still mobile enough in the plane parallel to the surface that they can migrate around on the surface to energetically favorable lattice sites and bond. Under unfavorable growth conditions, the physisorbed species may: (i) gather at the substrate surface to form agglomerations, such as in the case of too low substrate temperatures or presence of surface contaminations, or (ii) simply migrate around before desorbing, in the case of thermally energetic flux or too high substrate temperatures. Once bonded to the underlying lattice, these adatoms are more stable, and act as nucleation centers for the incoming flux. The final configuration of the overlayer is determined by the

thermodynamic interactions and reordering of the top 3-4 atomic layers near surface region.

2.1.1 Modes of Film Growth

On exposing the substrate to a source flux, the atomic/molecular specie in the flux condense on the substrate from the vapor phase where it may either diffuse along the surface, leading to adsorption, or re-evaporation. Depending on the various growth parameters such as deposition rates, substrate temperatures, lattice mismatch etc., the adsorbed atoms accumulate to form single crystalline, polycrystalline, or amorphous thin films, as shown in Fig. 2-1.

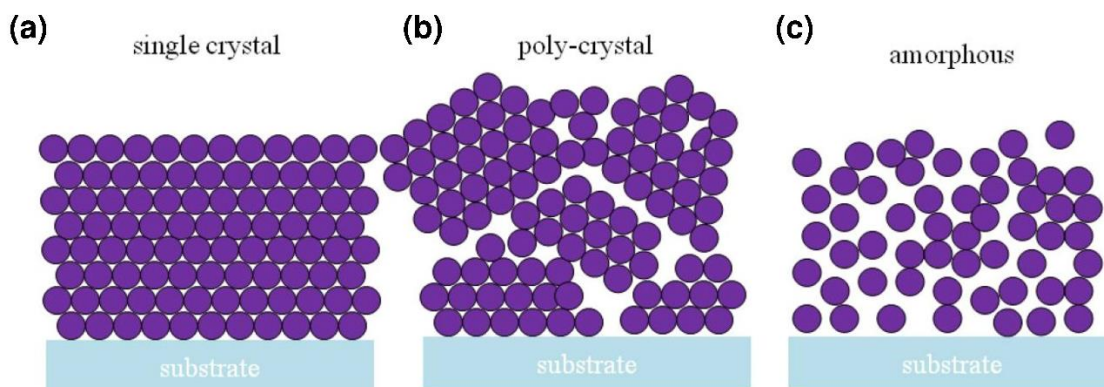


Fig. 2-1. Accumulation modes on a substrate surface. **(a)** Single crystal growth – deposited material arrange uniformly in a lattice across the entire sample. **(b)** Poly-crystalline growth – structure consists of short-order crystals growing along arbitrary orientations. **(c)** Amorphous – deposited atoms arrange randomly with no order. (Adapted from ¹Brahlek, 2014)

In a single crystalline growth, the crystal structure in the epitaxial film has a long range order and remains the same across the entire substrate (Fig. 2-1a). For this phase to occur, the growth rate has to be low enough that allows ample time for the atoms to move around on the surface to the preferred sites before more material

reaches the substrate. Also, to avoid unwanted desorption, and to maximize surface mobility, the substrate temperature also need to be optimized based on the substrate type and the material being deposited. Too low substrate temperature results in the incoming species having limited to no mobility resulting in a thin film with randomly oriented crystal grains, with grain size ranging from tens or hundreds of nanometer for polycrystalline film, to the order similar to that of unit cells in the case for amorphous thin films. Another reason for forming polycrystalline or amorphous film lies in the different crystal symmetries and/or lattice parameters of the substrate and the overlayer.

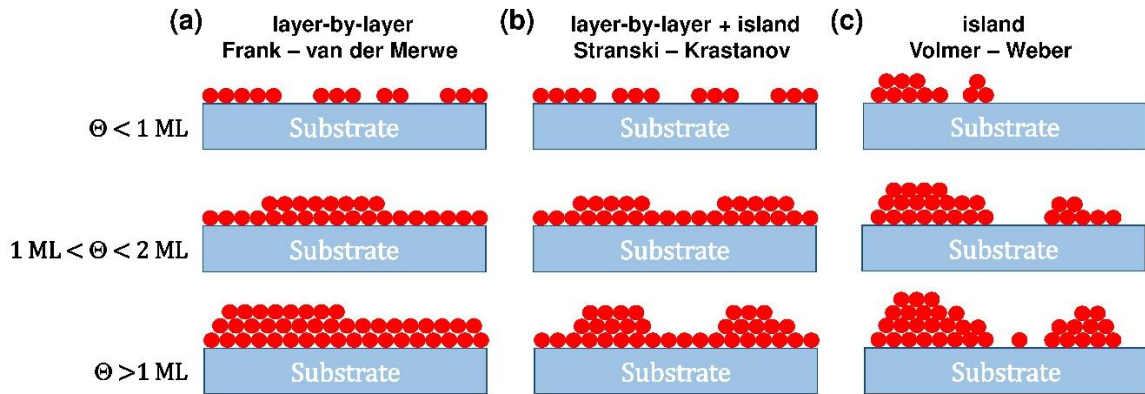


Fig. 2-2. Possible growth modes of the deposited material for different coverage (Θ) regimes, ML means monolayer: **(a)** the layer-by-layer (Frank – van der Merwe) growth, **(b)** Layer-plus-Island (Stranski – Krastanov) growth, and **(c)** Island (Volmer – Weber) growth.

The interactions between the substrate and the overlayer depend on many factors including the substrate's surface morphology, lattice mismatch between the epitaxial film and the substrate, and other growth parameters such as deposition rate, deposition method, substrate temperature etc. Based on these interactions, there are three primary modes by which an epitaxial growth proceeds, as shown in Fig. 2-2. In

the Frank – van der Merwe, or the layer – by – layer growth mode, the interaction between the substrate and epitaxial film is stronger than the interaction between atoms in neighboring layers of the epifilm, causing the adatoms to preferentially stick to the surface sites, resulting in a two-dimensional growth where a layer is completely formed before a new monolayer deposition begins (Fig. 2-2a). In contrast, in the Volmer-Weber, or the island growth mode, the interactions between the adatoms are stronger than the overlayer – substrate interactions, leading to a multilayer clustering of the adatoms and the subsequent growth of three-dimensional islands (Fig. 2-2c). In this mode, full surface coverage is possible only when the different islands grow in size, large enough for them to merge together. The Stranski – Krastanov, or the layer – plus – island growth mode is characterized by formation of both 2D layers and 3D islands (Fig. 2-2b). It can be considered as a two-step process: after an initial formation of one, or at times a few, complete monolayer in a layer-by-layer growth mode, the strain and chemical potential of the epifilm causes the further growth to be carried out through nucleation and coalescence of islands. This growth mode is heavily influenced by the symmetry or orientation of the epitaxial film with respect to the substrate.

One of the major factors influencing the growth is the lattice mismatch between the substrate with the film to be grown; depending on whether the lattice spacing of the film is larger or smaller than that of the substrate, compressive or tensile strain will be incorporated in the epitaxial film during the growth as the film tries to adjust to the substrate lattice. The level of this strain introduced due to the lattice mismatch can be quantified as, $f = (a_{film} - a_s)/a_s$, where a_s and a_{film} are

the substrate and the epifilm in-plane lattice constants respectively. In case of a large lattice mismatch, the strain energy will dominate other surface-adatom interactions, leading to an island-like growth occurring off few energetically favorable nucleation points. On the other hand, if at the onset of growth, this strain is minimal, the surface tension energetics between the substrate and the adatoms exceeds the energetic cost of straining the film, and the growth may proceed in the layer-by-layer mode. This strain may not continue all the way into the bulk of the epitaxial film, and beyond a critical thickness, if the elastic strain in the field exceeds the adhesion force in the deposited material, the need for energetically favorable structure may force the transition from layer-by-layer to island growth mode.

2.1.2 Relaxation, Reconstruction, and Defects

Although the surface of a crystal indicates the end of its bulk structure, it's not as simple as mere truncation of the bulk crystal. The interatomic forces acting on the surface atoms differ from those in the bulk owing to the absence of neighboring atoms on one side, which then leads to a surface layer with altered atomic positions with different spacing and/or symmetry, as compared to the bulk. This shift in equilibrium atomic configuration of top few layers parallel to the surface, can be categorized as either relaxation or reconstruction.

Most metals have a strongly delocalized electron gas due to broken chemical bonds on one side of the surface, causing the surface layers to move in a direction normal to the surface plane, thus, reducing the inter-layer spacing. This change in position of entire layer of atoms in the lateral or normal direction so as to minimize

the positional energy is referred to as relaxation. In this case, the periodicity within the topmost atomic layer parallel to the surface is the same as that in the bulk.

On the surface of most semiconductors, significant directional bonding is present, leading to a change in the two-dimensional atomic configuration within the surface layers, in addition to possible shift in interlayer separations normal to the surface. This type of atomic rearrangement where the total number of atoms in a layer may be greater or fewer than in the bulk is called reconstruction. One of the well understood examples of reconstruction is the atomically clean Si (111) surface, as seen in Fig. 2-3, from reflection high energy electron diffraction (RHEED) images.

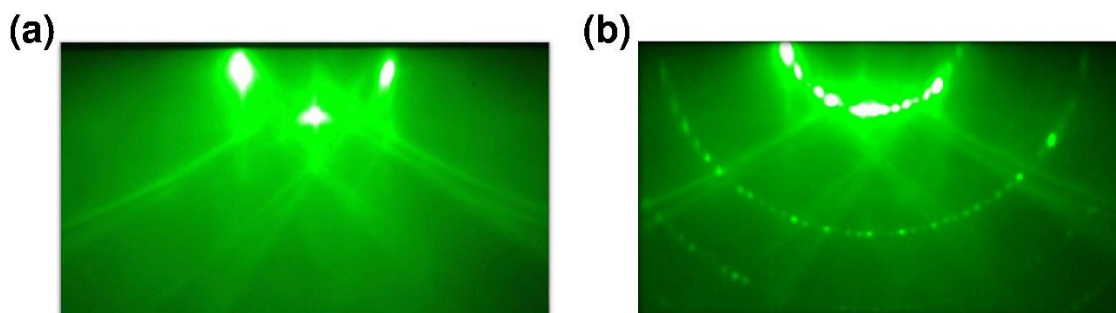


Fig. 2-3. Reconstruction of Si (111) structure as observed in RHEED. **(a)** 1×1 reconstruction observed on heating the substrate up to $900\text{ }^{\circ}\text{C}$. **(b)** Converts to a 7×7 reconstruction on cooling down the sample to below $850\text{ }^{\circ}\text{C}$.

Along the (111) Si surface, to decrease the overall surface free energy, free dangling bonds are saturated by forming new bonds within the surface, resulting in long π -bonded zig-zag chains between the first and second surface layers, known as 2×1 reconstruction. On heating the sample in high vacuum conditions to temperatures above $400\text{ }^{\circ}\text{C}$, the surface atoms rearrange into a more energetically stable structure, called the 7×7 reconstruction (Fig. 2-3b). To obtain an optimal

balance of charge transfer and stress, this new arrangement involves top three atomic layers to form a much larger cell unit. At temperatures above 870 °C, a disordered 1×1 structure is obtained, and a 7×7 reconstruction is regained on then cooling the sample.

A perfect crystal with complete translational symmetry is an idealization; whether in the grown film, or the reconstructed surface, defects are always found. While a perfect crystalline structure may be energetically preferable, it is difficult to eliminate the imperfections introduced in the crystal during growth. A major source of introducing defects is the lattice mismatch between the substrate and the grown film; as the film thickness increases, so does the strain accumulated in the film. If at a certain point, known as critical thickness, the accumulated strain exceeds the energy associated with some structural transformation in the film, dislocation defects may form at the interface, and the film relaxes to its original lattice structure. Other defects can be formed in the epitaxial film due to other growth conditions. These defects can be broadly classified on the base of their dimensionality, as point defects, line defects, and planar defects, schematically shown in Fig. 2-4.

The zero-dimensional defects affect only isolated sites in the crystal structure and do not extend in space in any dimension beyond the affected site, hence known as point defects, shown in Fig. 2-4a. These highly localized point defects may alter the crystal pattern at a single point, including a vacancy being formed when an atom is missing from its original position in the crystal structure, or when atom occupies an interstitial site that ought to be empty, resulting in an interstitial defect. In certain

cases, an atom may be missing from the crystal structure and a foreign atom occupying the same site, resulting in a substitutional point defect, these substitutional defects may be introduced intentionally to tailor the properties of the grown film.

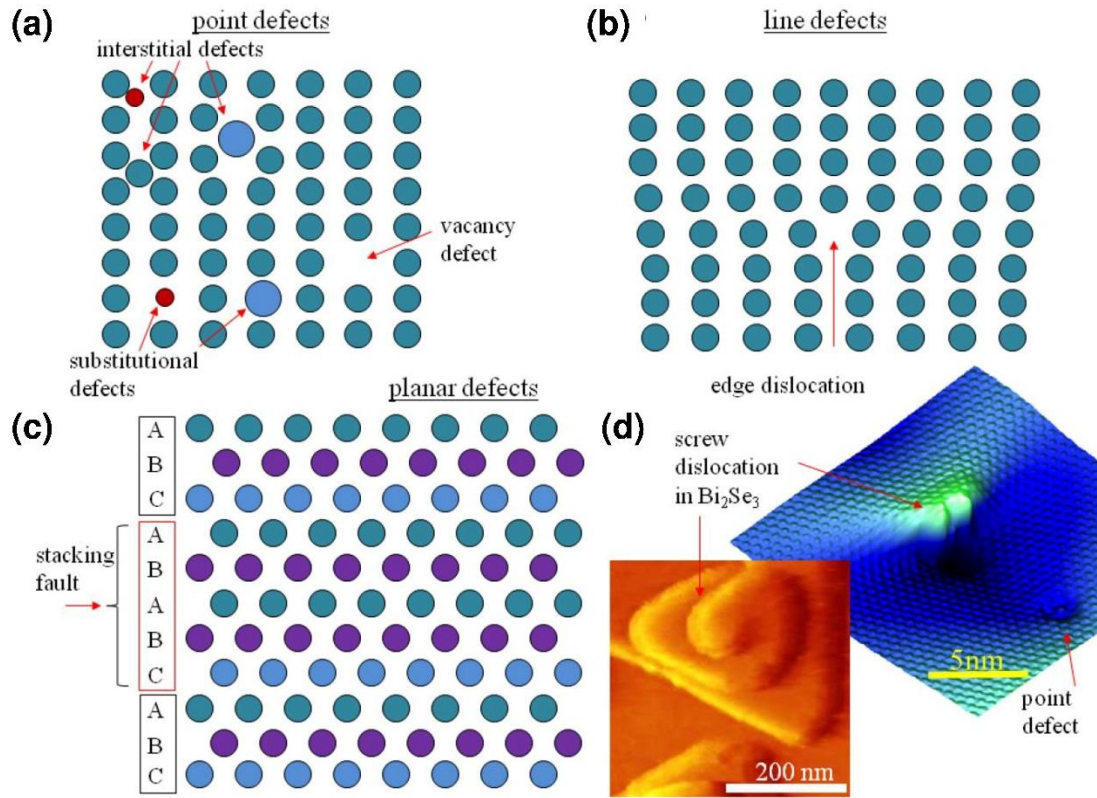


Fig. 2-4. A schematic illustration of different crystallographic defects. **(a)** shows the various point defects, **(b)** an extra column is grown into the crystal structure, causing an edge dislocation. **(c)** 2D planar defect is formed when the regular growth pattern is interrupted by an extra layer of atomic plane. **(d)** AFM images showing point defect and line defect in Bi_2Se_3 . (Adapted from ¹Brahlek, 2014)

The 1-dimensional defects, or the line defects, also known as dislocations, are lines through the crystal along which the crystal pattern is broken (Fig. 2-4b). Their principle role is to control the strain in the film, and can occur at the substrate-epifilm interface during the growth. Besides the edge dislocation, another example is screw

dislocation, as shown in Fig. 2-4d, where the thin film grows helically along a linear defect, forming a spiral structure.

A planar defect, or the 2-dimensional defects are surfaces along which different crystallites are joined, such as grain boundaries in a polycrystalline material. Another way this defect is introduced is when the stacking order of a crystal is interrupted; for example, the normal ABC-ABC-ABC... ordering of a hexagonal close-packed crystal structure, where A, B, C represent identical layers with 120° rotation, is interrupted and a layer is formed with ABA, ACA, BAB, BCB, CAC, or CBC ordering, as shown in Fig. 2-4c.

Depending on the desired properties in the grown films, growth parameters are optimized to either minimize these defects, or at times, to intentionally introduce defects to tailor the material properties or combinations required.

2.2 Molecular Beam Epitaxy

MBE is a material deposition technique, where fluxes of the desired species are generated by evaporation or sublimation of source material (molecular beam), and then deposited on a substrate, held at a suitable temperature, to form an ordered overlayer (epitaxy). A typical MBE system, as shown in Fig. 2-5, is equipped with multiple evaporation sources, mainly effusion cells; each source containing an individual element. Besides thermal cells, electron-beam evaporators are used for refractory elements, such as Zr, Nb, Mo, Ta, W, Re, Os, Ir, and a few other elements that are difficult to thermally evaporate, such as B, Rh, and Pt. However, e-beam

evaporation imparts higher energies to the emitted particles, and is not as easily controllable and reproducible as thermal evaporation.

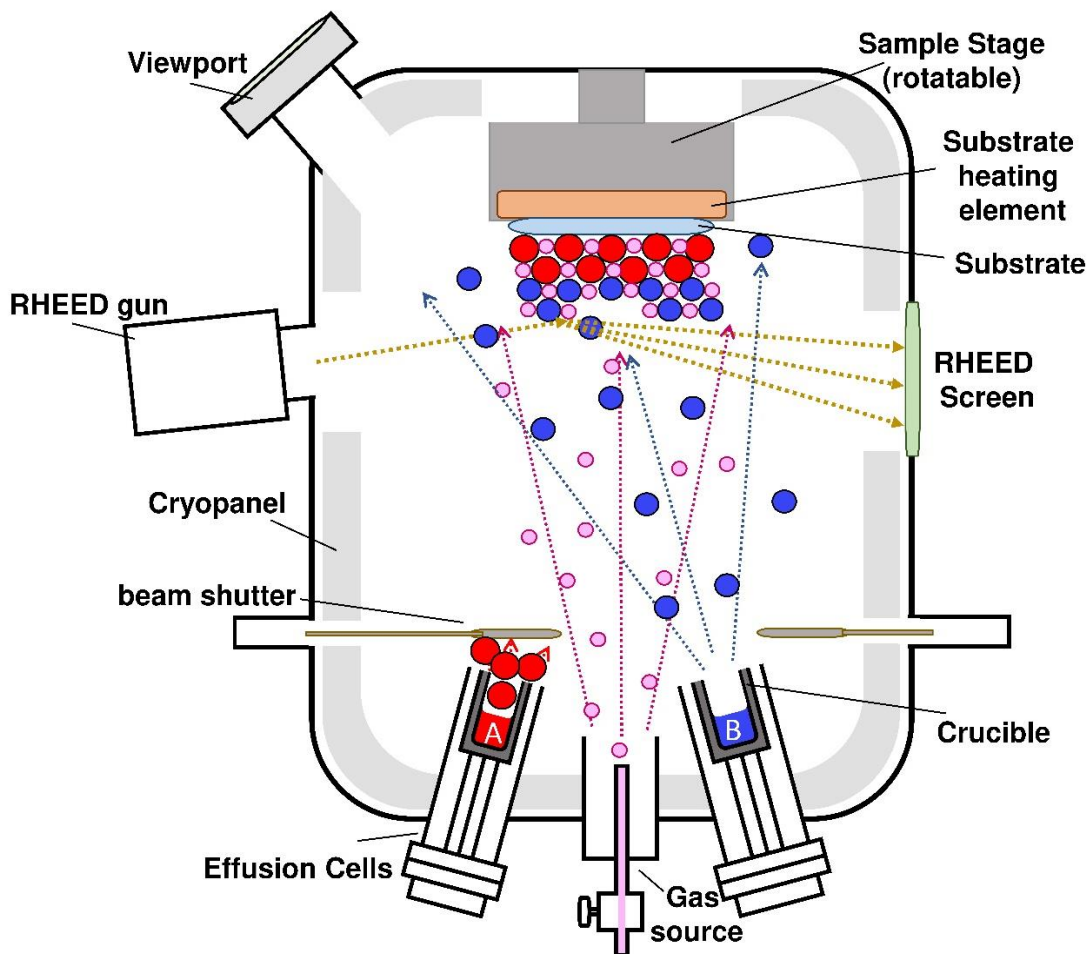


Fig. 2-5. A schematic illustration of a typical molecular beam epitaxy system. Thermal evaporators are used for flux generation, and beam shutters allow interruption of flux to control the film composition and doping levels. Cryopanel are used to lower the chamber temperature so as to avoid incorporation of impurities emitted by outgassing of the chamber walls. Ultra high vacuum conditions are maintained and RHEED is used to monitor film growth in real-time.

In case of many binary materials, such as ZnO, GaAs etc., the growth is self-limited and dependent on the cation flux, and thus, the stoichiometry of the film can be easily controlled as long as the growth is carried out in an excess (~ 10 -15 times) of the anion flux. However, for the growth of complex materials, such as perovskites

with the structure ABO_3 , the flux for sources A and B have to be controlled manually. For example, if the growth is carried out such as monolayers of AO and BO_2 are deposited sequentially, it is important to be able to interrupt the flux, and thus, beam shutters are employed to block the line of sight of source to the substrate. The substrate stage generally includes a heater assembly and a rotation system so as to heat the substrate to the desired growth temperature and also rotate the sample to ensure uniform coverage.

MBE process differs from other epitaxial techniques in its low deposition temperature and slow growth rates. Due to very low ambient pressures ($\sim 10^{-10}$ Torr) in the MBE chamber, the molecular species in the flux traverse the distance to the substrate without interacting with residual gases, minimizing accidental doping. The low chamber pressure also allows real-time *in-situ* monitoring of the growth process using RHEED. With a precise control over the composition and doping levels, MBE allows the growth of highly crystalline structures with arbitrary compositional profile.

2.2.1 Ultra-High Vacuum Conditions

The substantial progress in the physics of epitaxial thin films can be related to the advent of Ultra-High Vacuum (UHV) techniques. With ambient pressures lower than 10^{-10} Torr, thin films with negligible contamination can be grown because of the minimal reaction of the grown surface with residual gases in the vacuum chamber. Secondly, the UHV environment prevents scattering of (i) the atomic flux, and thus, reducing inter-source contamination, and (ii) the electron beams used in various monitoring techniques, thus, increasing the reliability of such techniques.

Under an assumption of complete adsorption, i.e. all species incident on the surface are adsorbed, a chamber pressure of $\sim 5 \times 10^{-7}$ Torr, corresponds to the growth rate of one monolayer per second (²⁶Farrow, 1995). The seriousness of this situation can be seen in that a typical MBE growth rate is of similar order. Normally, the residual gases are volatile enough not to adsorb on the substrate, but in the case of newly deposited surface, there are enough free chemical bonds to enhance the adsorption of these residual gases. These contaminants are incorporated either as an impurity on the surface, or combine with the incident specie to create an undesirable molecule, such as oxidation of the flux; in either case, leading to a disruption in the growth. In contrast, at a pressure of $\sim 10^{-10}$ Torr, the time taken to deposit one monolayer of the residual gas is to the order of hours; thus, to achieve high purity samples with low defect densities, clean UHV conditions are nonnegotiable.

A typical UHV chamber is a stainless steel vessel attached to a combination of different pumps, each operating over a limited pressure range, and respective pressure gauges to obtain a background pressure range from atmospheric to UHV conditions on the order of 10^{-10} Torr. These different parts are joined together by standard conflat flange systems; to make a UHV seal, knife-edges of the two flanges bite into a copper gasket inserted in the middle of the two. A rubber, or viton gasket, on the other hand, cannot be used for achieving UHV pressure as they not only act as a source of outgassing, but may also deform and generate air leaks during the bake-out process.

During operation of an MBE system, at times, it is necessary to expose the UHV growth chamber to air, often in the case of replenishing exhausted source materials,

resulting in the inner walls accumulating several monolayers of adsorbed atmospheric gases, especially oxygen and water molecules. On pumping down the chamber, these molecules slowly desorb over a long period of time, the lowest achievable pressure being around 10^{-8} Torr. Thus, after each air exposure, to completely degas the chamber walls, it is required to *bake* the UHV system to a temperature of ~ 200 °C. At our MBE lab at Rutgers, we wrap heating tapes around the chamber and heat the chamber for about 8 – 10 hours, or longer if required. Once the pressure of the heated chamber stabilizes to the order of low 10^{-7} Torr or high 10^{-8} Torr pressure range, it indicates that the water and oxygen molecules have been removed, and the bake-out equipment can be switched off. On cooling to ambient temperatures, the chamber pressure then slowly falls into the UHV regime.

There are several types of vacuum pumps, categorized by their operating pressure range; each requires different initial pressures at which they can be reliably turned on. In basic terms, a vacuum pump can be said to operate by removing the air molecules from the vacuum chamber; as the chamber pressure drops, removing additional molecules becomes exponentially difficult. Thus, a typical system requires different styles of pumps to achieve UHV conditions.

Positive displacement transfer pumps, usually consist of two nested spiral stages mounted in series, Fig. 2-6a, that trap and compress a volume of gas until it reaches a minimum volume and a maximum pressure, which is then vented to the atmosphere. Rotary pumps, also known as roughing pumps, include Piston, scroll, rotary vane, or diaphragm pumps, and are used to establish an initial vacuum, pumping down the system from atmospheric (~ 760 Torr) to $\sim 10^{-2} - 10^{-3}$ Torr

range; often used as dry backing pumps for high vacuum pumps connected in series. It is recommended to avoid roughing pumps that use oil, so as to prevent contamination of the chamber in case of an accidental back streaming. In high vacuum conditions, the rotary pump starts acting a source of leak, and thus, needs to be valved off from the main chamber.

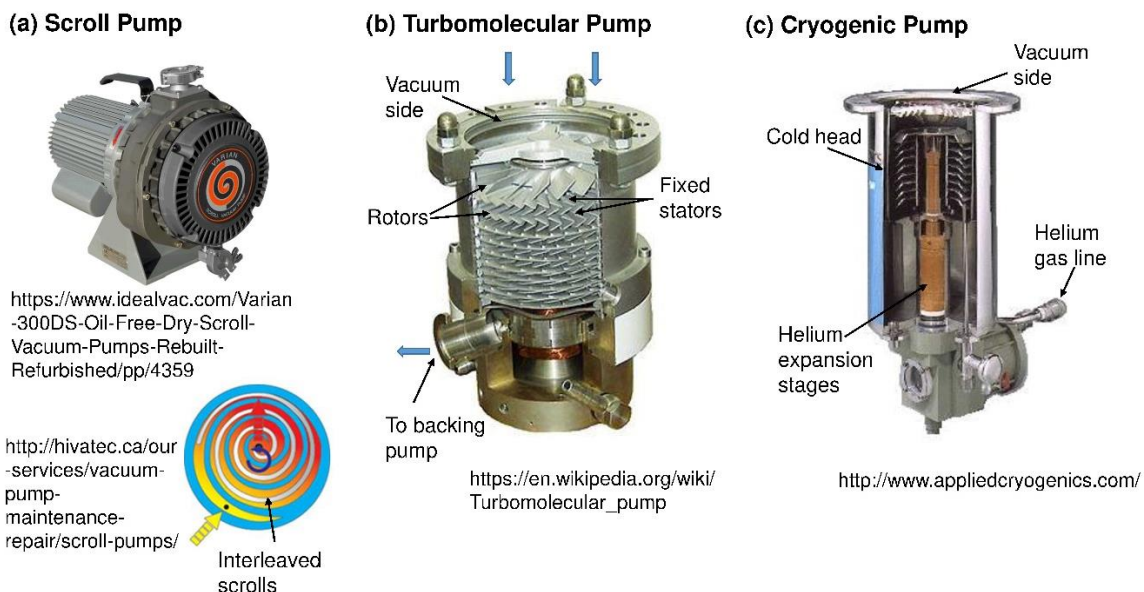


Fig. 2-6. Images of various types of pumps used in a UHV chamber: **(a)** scroll pump, **(b)** turbomolecular pump, and **(c)** a cryogenic pump. (References for different images included in the figure)

Turbomolecular (or Turbo-) pumps (Fig. 2-6b) are the most commonly used momentum transfer pumps; they operate by directing gas molecules from the vacuum side towards the pump outlet using high speed rotating angled-blades, interleaved with stationary rotor blades. The momentum transfer from the rotating blades to the residual gases increases the probability of molecules moving towards the gas transfer holes in the stator. By passing through several of these stages, the captured gas is lead towards the vent port; this high pressure build-up at the outlet is

then pumped by a roughing pump connected in series. The turbo-pumps can be used to achieve a vacuum of around high 10^{-9} to low 10^{-8} Torr.

To achieve ultra-high vacuum, beyond the capability of a turbomolecular pump, capture pumps that entrap the residual gases are then used. Typical examples include cryogenic pumps (or cryopumps) and ion pumps; these operate at lower flow rates than transfer pumps, and are, thus, usually valved off until a medium-high vacuum is achieved in the UHV chamber. Cryopumps, as the name suggests, entrap the gas molecules onto a very cold surface within the vacuum pump to achieve UHV, down to the order of low 10^{-10} Torr. Cryopumps use compressed helium as a refrigerant, which is then expanded within a cold head, and subsequently cooling down to ~ 10 K. The pump holds the trapped gases as long as the surface remains cold. Due to limited gas storage capacity, these pumps need to be regenerated by warming up the cold surfaces to room temperature, allowing the trapped gases to change into a gaseous state, which are then pumped through another vacuum pump. During the regeneration, the cryopump is usually isolated from the vacuum chamber to prevent the chamber from exposure to the released gases.

2.2.2 MBE System at Rutgers University

The MBE system at Rutgers University, Fig. 2-7, was designed and build by SVT Associates; constructed out of 300 series stainless steel, sheets of ~ 0.1 in. thick are rolled and welded together with conflat flanges for mounting myriad vacuum components. At many different angles, sealed glass windows or viewports are mounted, allowing a sight into the chamber. Gas is introduced into the system using

either sapphire leak valve that allows slow and controlled flow of gas, or shut-off valves that are used to vent the system. The jumbled up mess of wires and tubes, as seen in Fig. 2-7, are electrical wiring (for thermal cells, sputter gun, RHEED electron gun, thermocouples, and all pressure gauges), cooling lines (pink because of using glycol as a coolant), purified gas sources lines (for introducing O₂, N, Ar, and He), compressed air lines (for pneumatic gate valves and beam shutters), and vacuum exhaust lines. All the control units for pneumatic valves and other electronics are mounted on the electronic rack (blue unit behind the computer desk), and are all interfaced with a computer, allowing remote control of most growth processes.

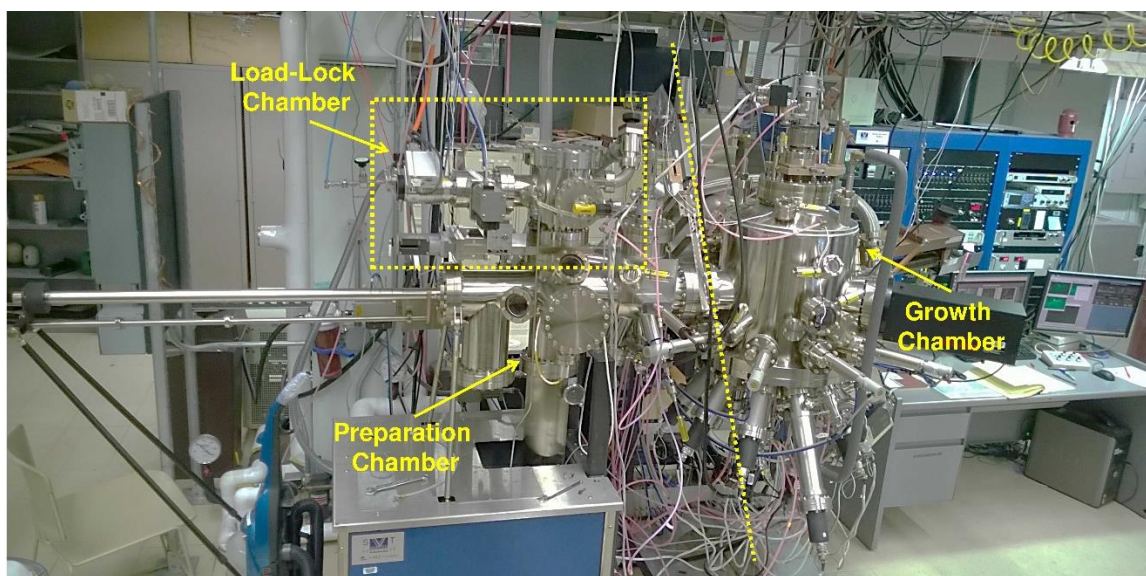


Fig. 2-7. Image of the front overview of the MBE system at Rutgers University; the system has three vacuum chambers – a load lock chamber, preparation chamber, and finally the growth chamber. (The dashed lines are along the position of respective UHV gate valve.)

The entire system is broadly composed of three vacuum chambers – load lock chamber, preparation chamber and the growth chamber. The “fast-entry” load lock (LL) system is used for introducing substrates into, and removing processed samples

from the MBE system, and is the only chamber regularly vented and opened to atmosphere. The vacuum is achieved using a turbomolecular pump with a dry scroll pump acting as a backing pump; pumping the chamber pressure from atmosphere (760 *Torr*) down to 10^{-6} *Torr*.

Vertically below the LL chamber is the preparation (prep) chamber; the clean substrates and grown samples are usually kept in this chamber. The prep chamber is equipped with a sample stage and can be used to pre-process the substrates, if required, such as heating or de-gassing or sputter-depositing something prior or after film growth, without breaking vacuum. Transfer of samples from LL to prep chamber was conducted only when the LL chamber pressure was in low 10^{-6} *Torr*, so as to minimize the contamination of prep and growth chambers from outgassing of the air-exposed surfaces in the LL chamber.

Adjacent to the prep chamber is the growth chamber; UHV gate valves between LL and the prep chambers, prep and the growth chambers, ensure high vacuum integrity of the growth chamber while venting the load-lock chamber. From the LL chamber, the samples are moved to prep chamber in UHV conditions, and then to the growth chamber, eliminating the need to expose air exposed LL chamber to growth chamber, and minimizing contamination. Both the prep and growth chambers are pumped by cryo-pumps, with typical base chamber pressure being $\sim 10^{-9}$ *Torr* and $\sim 10^{-10}$ *Torr* respectively; the comparatively higher pressure of the prep chamber is due to its regular exposure to the “dirty” LL chamber during sample transfer.

For routine maintenance, such as to replenish or change the source in a thermal cell, the MBE system needs to be vented. To minimize adsorption of atmospheric gases, instead of venting the system with air, compressed nitrogen gas is used to vent the required chamber; a continuous flow of nitrogen is maintained while the system is open to air so as to further minimize the effects of air exposure. To achieve UHV, it is necessary to make sure there is no leak – at this vacuum level, any minute leak can cause the chamber pressure to be stuck at $\sim 10^{-7} - 10^{-8}$ Torr. Main sources of leak are improperly tightened conflat flanges; a star-pattern order should be used to tighten the flanges to ensure uniform compression of the Cu gasket. Using a residual gas analyzer (RGA), helium gas levels in the chamber are measured, while flowing compressed He gas around the flanges and other areas suspected to leak; any small leak will lead to sharp rise in the He level as monitored by RGA.

2.2.3 Substrate Handling

The MBE system is capable of holding different sized substrates, ranging from few millimeters to three inches in diameter; mounted on up to ten holding rings. In this work, majority of the substrates used were $1\text{ cm} \times 1\text{ cm}$ in size. As shown in Fig. 2-8, any substrate smaller than 3 in. in diameter, can be mounted on to 0.030 in. thick sample plate, made from either molybdenum or Inconel (alloy based on nickel and chromium) and 3 in. in diameter.

As can be clearly seen in Fig. 2-8a, these sample holders have a window milled through allowing direct heating of the substrate from the heating element in the growth stage. There is a groove milled along the window perimeter that allows the

substrate to snugly sit in place. To hold the substrate in place, 0.016 *in.* thick tungsten-rhenium alloyed wires are threaded through holes on the substrate holding plate, and are bent such that they apply a downward pushing force on the edges of the substrate. Once the substrate is attached to the sample plate, it is mounted onto a holding ring and placed in the substrate cassette (Fig. 2-8c). In the load-lock chamber, the substrate cassette sits on a laterally retractable holder (Fig. 2-8d).

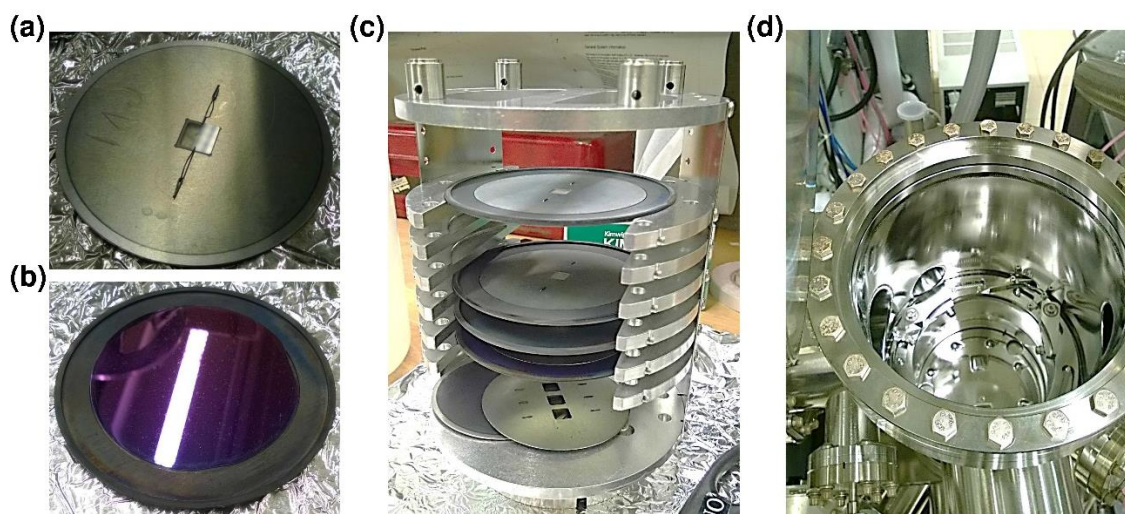


Fig. 2-8. Images for mounting the substrate in the load-lock chamber. **(a)** A 3 *in.* molybdenum plate holding a 1 *cm* × 1 *cm* Al₂O₃ substrate using tungsten-rhenium wires; the hole in the plate allows direct heating of the substrate. **(b)** A 3 *in.* SiO₂/Si wafer mounted on the holding ring. **(c)** The substrate holder and the holding ring are placed in the grooves in the sample cassette; six substrates can be loaded into the MBE system at the same time. **(d)** The retractable holder that the substrate cassette sits onto.

Using a roughing pump and then a turbo pump, the pressure in the LL chamber is brought down to $\sim 10^{-6}$ Torr. At this point, the gate valve between the LL and prep chamber is opened; the elevator is raised until the cassette is pushed above the retractable holder. On retracting the holder, the substrate cassette can be then smoothly brought down in the prep chamber, and the gate valve is again closed. Using the pulley elevator, the substrate cassette can be moved up and down to allow

the desired substrate holder ring to be placed on the transfer arm. The horizontal transfer arm is aligned with the prep sample stage and the growth sample stage, allowing transfer of the sample to and from the growth chamber.

2.2.4 Thermal Cell

Effusion cells (Fig. 2-9) are often used as thermal evaporation is a controllable and reproducible process, giving the ability to control the flux rate by simply changing the cell temperature. Highly purified elements, with purity better than 99.999%, are commercially available; the material properties to be considered are the reactivity and the temperature dependence of its vapor pressure.

When installing a new crucible, before source is placed into it, it needs to be outgassed by heating it to high temperatures in vacuum to minimize any source contamination. Commonly used crucible materials are Al_2O_3 , pyrolytic boron nitride (PBN), graphite and tantalum; Ta crucible is used only for sources that have low vapour pressures, such as lanthanum, thus requiring being heated to high temperatures before a useable flux can be obtained. Many of these crucible materials are brittle, and can crack during melting and solidification of source material. To minimize this stress, a very slow ramp rate is used near the source melting point, $\sim 1 - 2 \text{ }^\circ\text{C}/\text{min}$. To achieve a useable flux, typically $\sim 10^{13} / \text{cm}^2\text{s}$, the source vapor pressure needs to be in the range of $\sim 10^{-4} - 10^{-3} \text{ Torr}$, which then gives an approximate cell temperature; the flux can be measured at this point, and the cell temperature can be tweaked to obtain the desired flux.

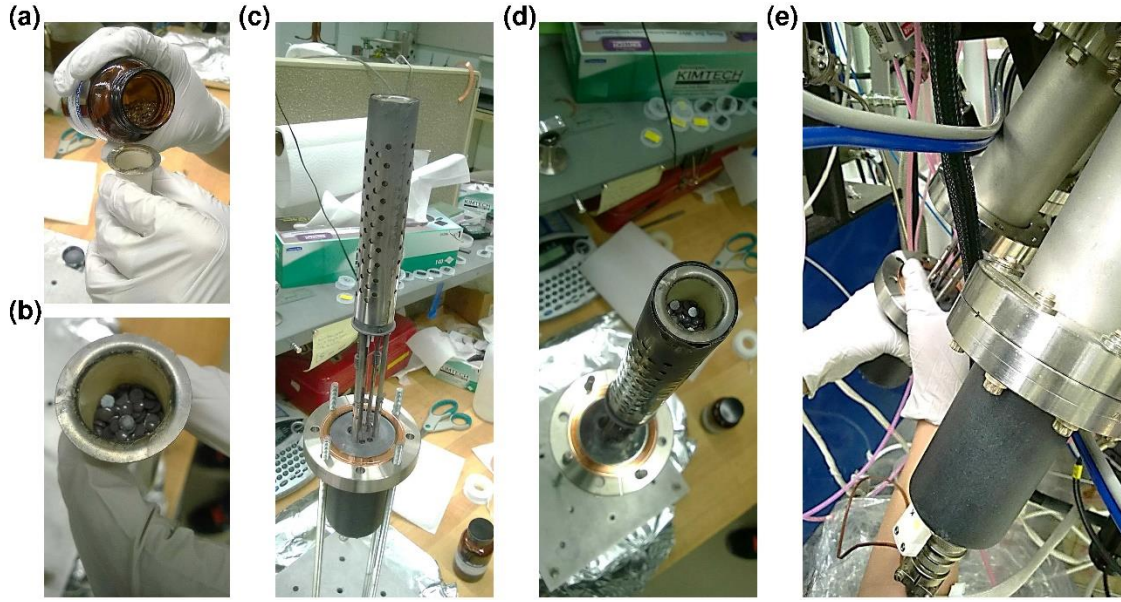


Fig. 2-9. Images of a low temperature thermal cell while replenishing the source material. **(a-b)** The alumina crucible as it is refilled with Se shot. **(c-d)** The front and top view of a Se thermal cell, while mounted on a maintenance stand. **(e)** Remounting the thermal cell in the MBE chamber after replenishing the source, Se.

2.3 Atomic Flux Measurement

Growth of high quality thin films with a very precise composition by MBE necessitate accurate control over fluxes, thus, requiring some reliable and reproducible methods for periodic recalibration of the flux. MBE systems are equipped with various in-situ flux measurement techniques, such as quartz crystal microbalance (QCM), atomic absorption (AA) or ion gauges, depending on the required stability or accuracy of the flux and the nature of the flux source. The source flux can also be calibrated *ex situ* by Rutherford backscattering spectroscopy (RBS) in conjunction with the *in situ* methods. In our work, we use a combination of QCM and RBS measurements to determine the source flux to an accuracy of $\lesssim 1\%$.

2.3.1 *In situ* Quartz Crystal Microbalance

The quartz crystal microbalance, or the QCM, operates by measuring the change in frequency of a quartz crystal resonator as material is deposited on its surface, and is used to measure masses as low as $\sim 10^{-8} g$. The basic principle of operation is that the resonance frequency of the quartz crystal is partially dependent on the thickness (or mass) of the crystal; it can be considered similar to a spring-mass system. The resonance frequency of such system can be given as $\omega_0 = \sqrt{k/m}$, where k is the spring constant, and m is the mass connected to the spring.

When the QCM is exposed to the flux, a portion of it gets deposited on the quartz crystal, changing the total mass of the crystal. During normal operation, other influencing variables such as geometry and material properties of the crystal remain constant, and only the mass changes; an increase of mass by Δm corresponds to a decrease in resonance frequency by $\Delta\omega \approx -\omega_0\Delta m/2m$. The quartz crystal used in the assembly is usually cut at $\sim 35^\circ$ with respect to the c-axis and has an initial resonance frequency of $\sim 5 MHz$. With the knowledge of quartz crystal geometry, resonance frequency constant ($\sim 1656 kHz\cdot mm$), and the mass density of the material being deposited, along with the measured change in frequency, the total mass accumulated over a period of time can be calculated. By converting mass density to atomic number density, this accumulated mass yields information about the number of atoms reaching the substrate position per unit of time.

In the MBE chamber, the QCM is mounted on a retractable bellow system, so as to allow the flux measurement at the same position as the substrate for an

increased accuracy, Fig. 2-10; the growth stage is raised and the QCM is moved into the substrate space. The QCM is electrically connected to a control unit; by inputting the source element, its mass density, and the Z-ratio (measure of the film's density and shear modulus with respect to quartz, typically ~ 1), the flux value can be read out.

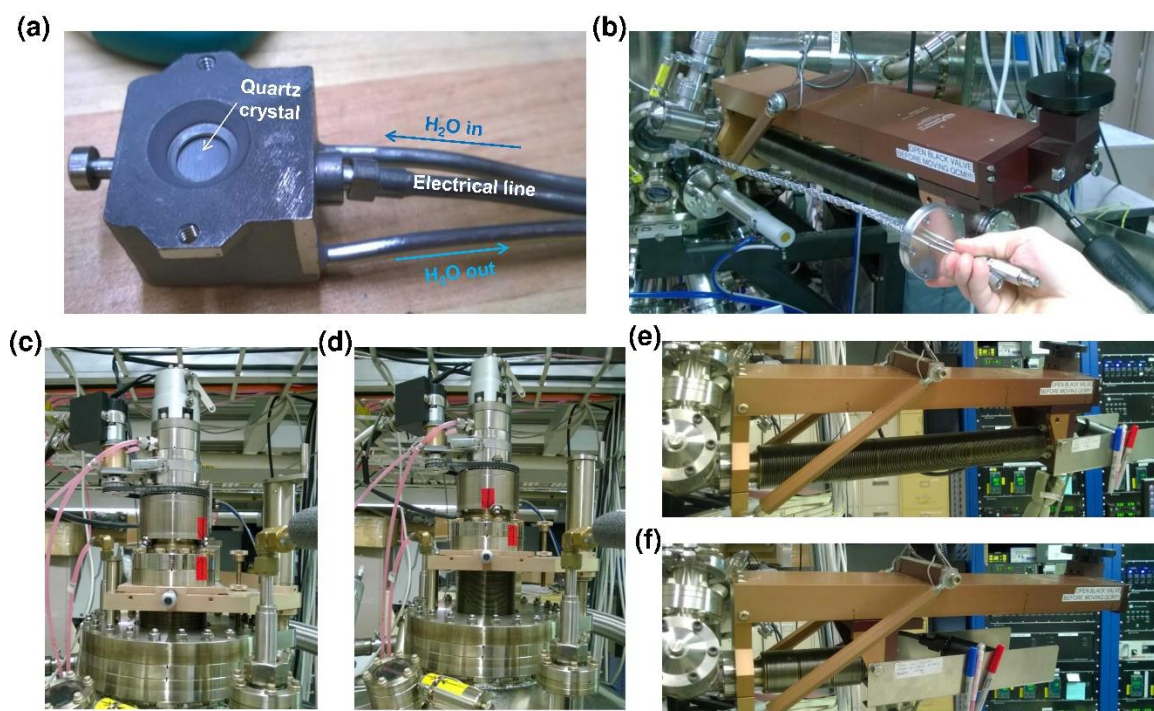


Fig. 2-10. Images of the QCM mounted in the MBE system. **(a)** Image of the measurement head where the quartz crystal is mounted, and is connected to the electrical line and the water cooling lines. **(b,e,f)** The QCM is mounted on a conflat feedthrough flange, which in turn is mounted on a retractable baffle system. **(c,d)** To measure the flux reaching the substrate, the growth stage is raised and the QCM is moved to the substrate position. (Adapted from ¹Brahlek, 2014)

The QCM is highly temperature sensitive, and any temperature gradient gives rise to an internal stress, which in turn causes a shift in the oscillation frequency. The QCM control unit is unable to distinguish this shift in frequency due to radiative heating from the source thermal cell and the heat transferred from the material being

deposited, from the shift in frequency due to the mass of the material being deposited, and thus giving an erroneous flux value. To minimize this effect, the quartz crystal is mounted in a cooled housing (Fig. 2-10a), and connected to a dedicated chiller.

To further take into account any geometric effect and thermal effect, the flux value is recalibrated against RBS data. Prior to growing the film, the individual fluxes for each element are measured and are then compared to the flux values obtained by RBS.

2.3.2 *Ex-situ* Rutherford Backscattering Spectroscopy

Rutherford Backscattering Spectroscopy, or RBS, is used to determine both the structure and the composition of a sample by measuring the backscattering of a beam of high energy ions impinging on the target sample. The origin of this technique lies in the Geiger-Marsden experiment where backscattering of alpha particles (He^{2+}) impinging on a thin gold foil revealed the existence of a dense nuclear core.

The Laboratory for Surface modification at Rutgers University hosts a 1.7 megavolt Tandetron accelerator, which accelerates the ions for RBS measurements. The ions, usually alpha particles, are impinged on the sample surface at a normal incidence, and the backscattered ions are then detected by a silicon detector at an angle of 165° relative to the incoming beam. The ions scatter off of the target atoms by simple Coulomb reaction, thus conserving the total energy and momentum. This interaction can be quantified as $E_{measured} = kE_0$, where $E_{measured}$ and E_0 are the energy of the particle after and prior to scattering. The kinetic factor, k , can be given as:

$$k = \frac{\left(\sqrt{m_1^2 - m_2^2 \sin^2 \theta} + m_1 \cos \theta\right)^2}{(m_1 + m_2)}$$

where θ is the backscattering angle, m_1 and m_2 , and Z_1 and Z_2 are the mass and nuclear charge of the ion and the nuclei in the film respectively. The coulomb potential between the nuclei give the Rutherford cross-section as:

$$\sigma = \left(\frac{Z_1 Z_2 e^2}{4E_0}\right)^2 \frac{1}{\sin^4 \theta/2}$$

The cross section and the kinetic factor are sensitive to the target ion, thus yielding a chemical composition profile. The penetration depth of these high energy incoming ions is greater than $1 \mu m$, much larger than the sample film thickness. As the ion penetrates into the film, small-angle scattering from the electrons in the film causes the incoming ion to continuously lose energy; similarly, after backscattering, the ion again loses energy as it emerges out of the sample. This loss in energy of the backscattered ion gives information about the depth profile. This backscattering spectra is analyzed and fitted to yield film composition using SIMNRA, a computer simulation program for ion beam analysis methods.

2.4 Reflection High Energy Electron Diffraction

The Reflection High Energy Electron diffraction, or RHEED, technique complements the MBE growth in that it offers atomic scale information in real-time during the growth, and yields unambiguous surface morphological details. A distinct advantage of using RHEED to monitor the growth over ex situ characterization techniques, such as X-ray diffraction or atomic force microscopy, is that RHEED allows to modify

growth parameters such as substrate temperature or even interrupt the growth, in case of unsatisfactory film growth.

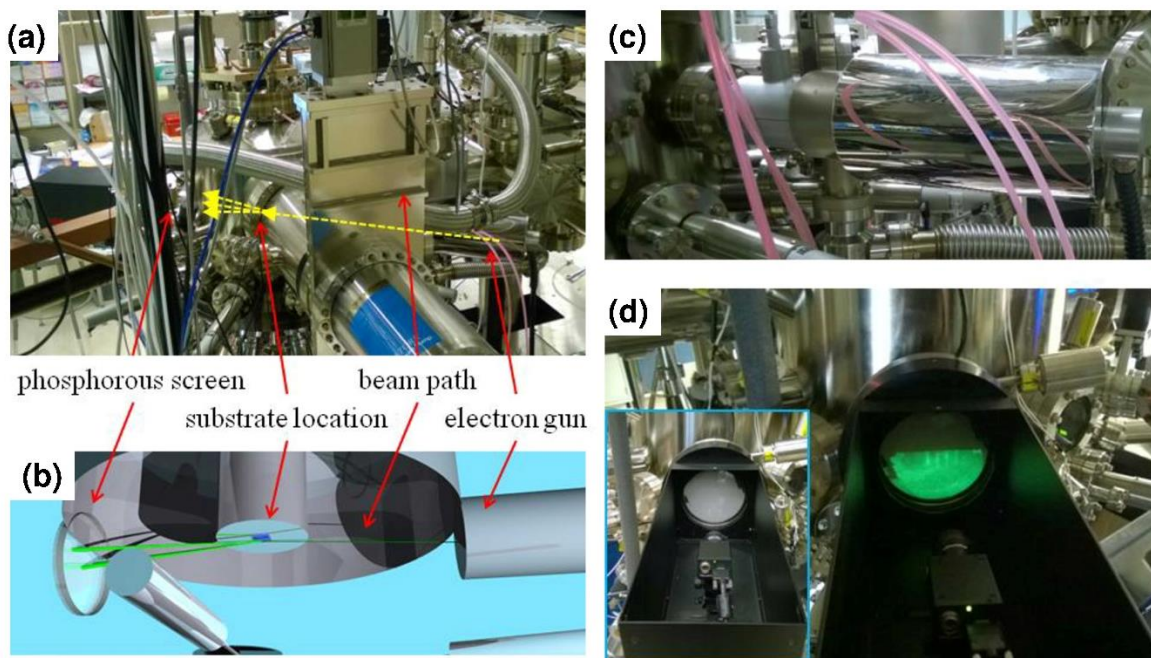


Fig. 2-11. Images and schematics for in situ reflection high energy electron diffraction system mounted on the growth chamber. **(a,b)** The experimental geometry for RHEED. **(c)** The electron gun, used to generate electron beam, is mounted using a conflat flange. A differential pumping line is seen connected to the preparation chamber and is used to minimize oxidation of the filament when the growth chamber is filled with oxygen. **(d)** A CCD camera in a light proof box is mounted around the phosphorus coated RHEED screen to capture the diffraction pattern. The inset shows when the blank screen when the electron gun is beamed off. (Adapted from ¹Brahlek, 2014)

Figure 2-11 shows the RHEED system mounted in the MBE chamber at Rutgers, and a schematic of such set-up (Fig. 2-11b). The electron gun generates a beam of electrons with energy of $\sim 5 - 20 \text{ keV}$, which then impinges on the sample at a very shallow angle ($\sim 1^\circ$), making RHEED very sensitive to surface morphology and roughness. For the sake of uniformity during a growth, and between multiple growths, the energy of the electron beam was set to 10 keV for all our work. These incident electrons diffract from the different surface atoms, and form patterns on the

detector as a function of time and surface morphology. The detector is simply a phosphorus screen mounted between a conflat viewport and the growth chamber (Fig. 2-11d). A CCD camera, housed in a light-proof box and mounted outside of the viewport, captures the image projected on the phosphorus screen and sends it to computer, where it is analyzed using a commercially available RHEED software. The beam width is $\sim 1\text{ mm}$, and thus, the diffraction pattern observed is the average over a large surface area.

The electron strike the sample surface at a glancing angle of $\sim 1^\circ$; thus, the normal component of kinetic energy comes to be $10\text{ keV} \times \sin 1^\circ \approx 100\text{ eV}$. The mean free path of electrons at this energy, almost independent of the material, is to the order of ~ 5 to 10 \AA ; this sample depth represents only a few monolayers, making RHEED highly surface sensitive.

Chapter 3. ELECTRICAL MEASUREMENT

In previous chapter, we discussed the epitaxy process used to synthesize thin films and various in-situ and ex-situ characterization techniques. However, synthesis of high quality thin films is only half the process; our preeminent goal in this work is to understand the physics of the novel states residing on the surface of topological materials. To study this interesting manifestation of non-trivial topology, we use transport measurements as our investigative probe. In this chapter, we briefly discuss the transport theory to enable us to understand the basic physics of transport through 3D topological insulators.

3.1 Electrical Transport

3.1.1 Drude Model

Transport measurements study the response of a material, in terms of resistance, carrier density, mobility etc., to an applied perturbation, electric field in this case. In the early 20th century, predating quantum mechanical theory, Drude model was put forth in an effort to understand and analyze the transport process, under a classic approximation of electrons in a solid behaving as a sea of freely moving electrons that bounce and re-bounce off of immobile positive ions or impurities in the lattice.

Electric current is the flow of electrons in a material in response to an applied electric field, and thus, the current density can be given as:

$$\vec{J} = qN\vec{v}_d$$

where, q is the electron charge, N is the charge per unit volume, \vec{v}_d is the drift velocity.

The electrostatic force, \vec{F} , experienced by a free electron on applying an external electric field, \vec{E} , is given as: $\vec{F} = d\vec{p}/dt = q\vec{E}$. This constant force implies that an electron should experience a corresponding constant acceleration, resulting in an unbounded increase in velocity with time, which further implies a constant increase in the current density with time; giving a linear dependence of current density on the applied field. However, a discrepancy is observed experimentally – initially, the current density increases with time, but it quickly saturates to some value, with the material beginning to dissipate heat. This heat dissipation is attributed to the electron releasing excess energy in the system through inelastic scattering.

Taking the scattering into account, the linear relation between current density and the applied field needs to be modified. The momentum of an electron at time t is $\vec{p}(t)$, thus at an infinitesimal time, dt , later, the momentum can be given as $\vec{p}(t + dt)$. Since it is impossible to know the precise initial momentum, nor the definite time elapsed between each collision, we can only use the average time between collisions, known as relaxation time, τ . Thus, the probability of an electron taken at random at t having a collision before $t + dt$ is dt/τ ; the probability of the electron not experiencing any collision is $(1 - dt/\tau)$. After collision, the momentum is randomly directed, giving the average momentum at $t + dt$ as zero. In case of no dissipation of

energy in absence of any collision, the momentum of the electron at $t + dt$ can be given as, $\vec{p}(t) + e\vec{E}dt$. Thus, it follows that the change in momentum over the infinitesimal time, dt , can be given as:

$$\vec{p}(t + dt) = (1 - dt/\tau)(\vec{p}(t) + e\vec{E}dt)$$

Applying the correction due to those electrons that do have a collision in the interval, dt , and taking the limit as $dt \rightarrow 0$, we can rewrite above equation as,

$$\frac{d\vec{p}}{dt} = -\frac{\vec{p}}{\tau} + e\vec{E}$$

In a steady state, the equation further reduces to $\vec{p} = e\tau\vec{E}$. Taking into account the n electrons per unit area, and $\vec{p} = m\vec{v}$, we get,

$$J = Nev = \frac{e^2 N \tau}{m} E = \sigma E$$

where, σ is the electrical conductivity, with mobility defined as: $\mu = e\tau/m$. According to this model, the mobility of an electron can be defined as the measure of how the electron's motion is disrupted because of scattering by crystal defects, and is thus very sensitive to the concentration of defects.

Taking into account the change in electron mass from material to material due to the effects of the lattice on the mass of the charge, the free electron mass, m , can be replaced with the effective mass, m^* ; making the Drude model suitable for the transport analysis.

3.1.2 Hall Effect

In simplest terms, Hall effect is the generation of a voltage difference transverse to an electric current in a material under the application of a magnetic field perpendicular to the current; this generated voltage drop being highly dependent on the type, number and properties of the charge carriers. In the presence of a perpendicular magnetic field, the charge particles experience a force, called the Lorentz force, and their paths curve based on the right hand rule, resulting in equal and opposite charge (holes and electrons) accumulating across the Hall element. This separation of charge establishes an electric field, which on reaching a steady value, prevents further migration of charge; this potential drop is known as Hall voltage.

Consider a bar of width, w , and thickness, t , as shown in Fig. 3-1; on applying a magnetic field in z – direction (coming out of page) and a current flow in x – direction, then as per the right hand rule, the charge will deflect towards the y – direction. As more and more electrons drift towards the $+y$ -direction, the electric field generated, E_y , counters the Lorentz force, and prevents further charge accumulation along the length of the Hall bar. The net force experienced by an electron is $F = eE - evB$, where eE is the electrical force, and evB is the Lorentz force; in the steady state, $eE_y = evB$.

The Hall voltage is given as: $V_{Hall} = \int_0^w E_y dy = wE_y = wv_d B$, and the Hall resistance can be computed by simple application of Ohm's law, $R_H = V_{Hall}/I$. In terms of current density, $I = JA = J(wt) = qNv_d(wt)$, which then gives, $R_H =$

$\frac{wv_d B}{qNv_d(wt)} = B/qNt = B/qn$, where, $n \equiv n_{2D} = Nt$, is the areal carrier density. Besides obtaining the carrier density, the slope of Hall resistance, R_H , gives the information about the charge-carrier types; negative slope indicates majority negative charge carriers.

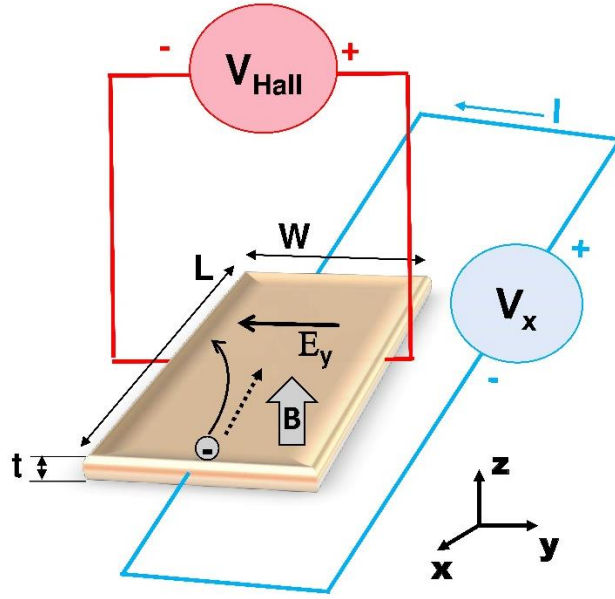


Fig. 3-1. A schematic of the Hall effect measurement on a sample of width, W , and thickness, t .

3.1.3 Van der Pauw and Hall Bar Geometries

The two most commonly used geometries for dc transport measurements are the Van der Pauw or the Hall bar, Fig. 3-2. Due to its simplicity, most of the measurements in this work were carried out in the Van der Pauw geometry. Both Hall bar and Van der Pauw geometries are four-terminal measurement techniques, where different pairs of metallic leads are attached to direct electric field into the sample, and read the resistivity values. The advantage of using 4-wire sensing is that, unlike 2-wire sensing, it does not include the lead resistance and the contact resistance in the resistance of

the sample. This is due to the high input impedance of a voltmeter, thus drawing negligible current through the voltage leads.

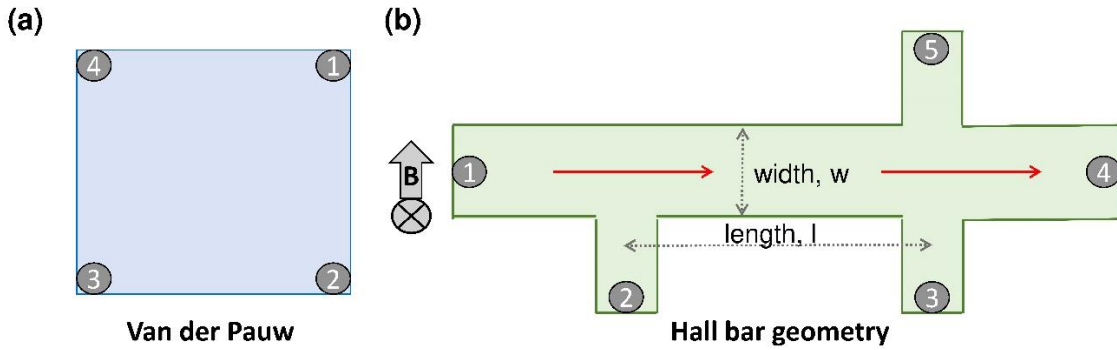


Fig. 3-2. A schematic for different geometries used for dc transport measurement. **(a)** Van der Pauw geometry, and **(b)** Hall bar geometry.

The Van der Pauw model, Fig. 3-2a, assumes an isotropic sample of uniform thickness, where the lead contacts are made at the corners of the sample, and that the lead contact areas is much smaller than that of the sample size. The longitudinal resistance is first measured by sourcing current through leads 1 and 2, and measuring the voltage drop across leads 3 and 4; the resistance is defined as: $R_{12,34} = V_{34}/I_{12}$. Next, the leads are shifted by 90° , giving $R_{14,23} = V_{23}/I_{14}$. Van der Pauw then showed that the sheet resistance, R_S ($\rho = R_S t$), can be given as: $e^{-\pi R_{12,34}/R_S} + e^{-\pi R_{14,23}/R_S} = 1$. Under the assumption of an isotropic material, $R_{12,34} \approx R_{14,23}$, and the Van der Pauw equation reduces to $R_S \approx \pi/\ln(2) R_{xx}$, where R_{xx} is the average of the experimentally measured values of $R_{12,34}$ and $R_{14,23}$, and $\pi/\ln(2)$ is a geometric factor. The Hall resistance is obtained by applying current through leads 1 and 3, and measuring the potential drop across leads 2 and 4. This geometry is susceptible to slight errors based on the placement of contact leads.

Similar data can be obtained by measuring the sample in Hall bar geometry, Fig. 3-2b; the longitudinal resistance is simply measured as $R_{14,23}$, and the Hall resistance as $R_{14,53}$. To obtain the sheet resistance, the geometric factor is simply the aspect ratio of the rectangle separating leads 2 and 3, giving $R_S = R_{14,23}(l/w)$. In this configuration, because the contacts are placed away from the active material, it minimizes the uncertainty introduced by the contacts.

3.2 Transport Measurement

Large thermal fluctuations destroy coherent quantum phenomenon, thus, to observe such effects, transport measurements have to be carried out at low temperatures. Most of the measurements in this work have been carried out at $\sim 1.5\text{ K}$ and upto 9 T magnetic field, or at $\sim 6\text{ K}$, in upto 0.6 T magnetic field.

3.2.1 Magnet Systems

The liquid helium cryostat, as shown in Fig. 3-3, designed and manufactured by American Magnetic Incorporated (AMI), uses liquefied nitrogen (LN, boiling point of 77 K) and liquefied helium (LHe, boiling point of 4.2 K) to achieve low temperatures down to 1.5 K . Both LN and LHe are bought in supply Dewers, and then transferred manually into the system. As shown in Fig. 3-3b, the outermost section of the system is a vacuum panel used to thermally isolate the inner cryogenic sections from the room temperature outside walls. The next section is a liquid nitrogen belly used to further thermally isolate the liquid helium stored in the inner chamber, and below LN belly. A 9 T superconducting magnet is situated inside the LHe belly with a

space for inserting the sample at its center. The sample space is again isolated from LHe belly using vacuum to minimize heat leakage. The sample is mounted at the end of a variable temperature insert, Fig. 3-3e, that can be taken out of the cryostat to change the measurement samples.

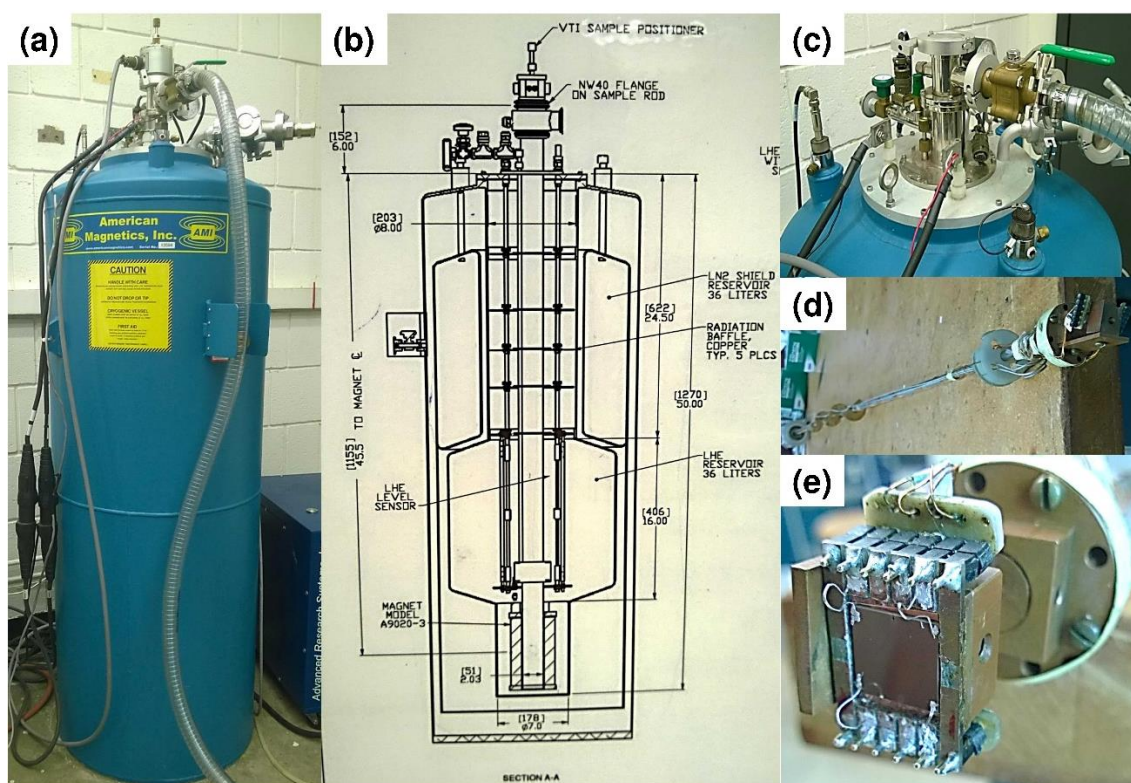


Fig. 3-3. Images of the liquid helium cryostat used to perform transport measurements at a temperature as low as ~ 1.5 K, and at up to 9 T of magnetic field. **(a,c)** Image of the cryostat, **(b)** with its schematic. **(d)** The variable temperature insert, taken out to mount a sample for measurement. **(e)** The end of the insert showing the sample holder, with a 1 cm x 1 cm sized sample mounted, ready for measurement. (Adapted from ¹Brahlek, 2014)

Once the sample is inserted into the system, LHe is slowly introduced into the sample space through a needle valve, which brings the sample temperature down to LHe boiling temperature of ~ 4 K. To further cool the sample, significant amount of LHe is first introduced into the sample space, and then after closing the needle valve,

the sample space is then opened to a vacuum line to pump out the LHe. This evaporation of LHe, by pumping, cools the sample to 1.5 K, for a few hours.

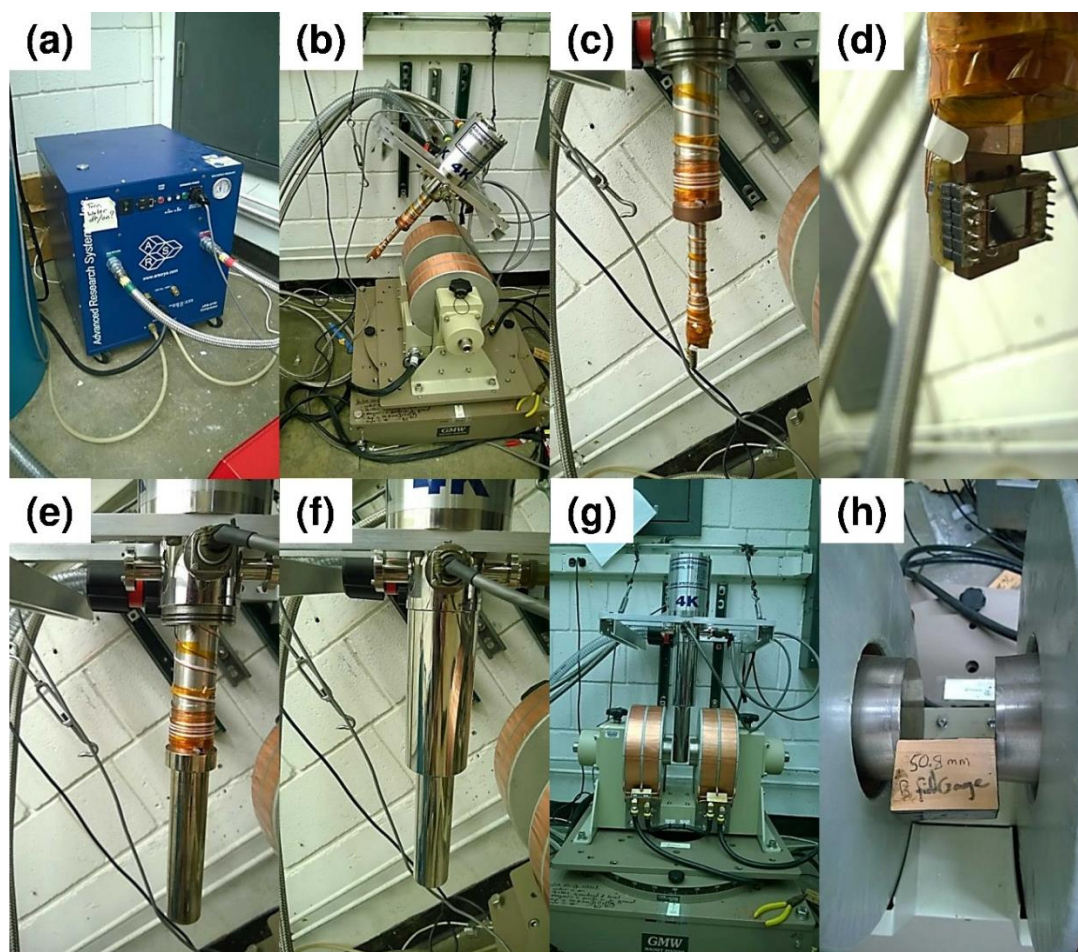


Fig. 3-4. Images of the Advanced Research System cryostat used to perform transport measurements at a temperature of ~ 5 K, and at up to 0.6 T of magnetic field. **(a)** The helium compressor, where the supply line (marked green) provides compressed helium, and the return line (marked red) contains the expanded gas. **(b,c)** The cold head rotated out of the magnet bore to mount the sample. **(d)** The mounted sample. **(e)** The nickel coated copper radiation is thermally locked onto 20 K stage. **(f)** The shroud that slides over, which is later pumped to isolate the sample space from room temperature. **(g)** The cold head rotated down in the position to start the measurement. **(h)** The bores of the electromagnet are separated by 50.8 mm. (Adapted from ¹Brahlek, 2014)

LHe is pretty expensive, and costs $\sim \$1000$ for a 100 l dewer; to reduce operating costs, we use another cryogenic system, designed and manufactured by

Advanced Research Systems (ARS) that doesn't require any cryogenic liquid, shown in Fig. 3-4. This system operates by compressing and cooling, and then re-expanding dry helium as a refrigerant gas. Externally compressed He gas is introduced into the chiller head, where the gas is expanded using a refrigeration cycle, and then sent back to the compressor. The sample is mounted on a cold head and reaches a temperature of $\sim 5\text{ K}$; this sample mount is isolated from room temperature outside walls by a nickel coated copper can (Fig. 3-4e) that is thermally locked to 20 K , and a vacuum shroud (Fig. 3-4f). The entire system is wall-mounted such that the sample can be rotated inside the bore of an external electromagnet that provides a field of $\sim 0.6\text{ T}$. The advantage of this configuration is that it allows an application of in-plane magnetic field.

The AMI system uses a niobium-titanium alloy superconducting magnet, and has a factory-installed firmware to control current, which in turn, controls the ramping field of the magnet. The system allows a maximum ramping rate of $\sim 0.024\text{ T/s}$; beyond which the magnet may quench, ie. transit into a non-superconducting resistive state. The ARS system uses a GMW Associates electromagnet, and can be controlled through a self-built LabVIEW program.

As discussed in later chapters, one feature of the topological surface states emerges in the transport properties in the form of Weak anti-localization (WAL) effect. The WAL effect appears at very low temperatures, in the form of sharp increase in resistance on applying very small magnetic field, thus it requires a very slow magnetic field ramping rate around zero magnetic field.

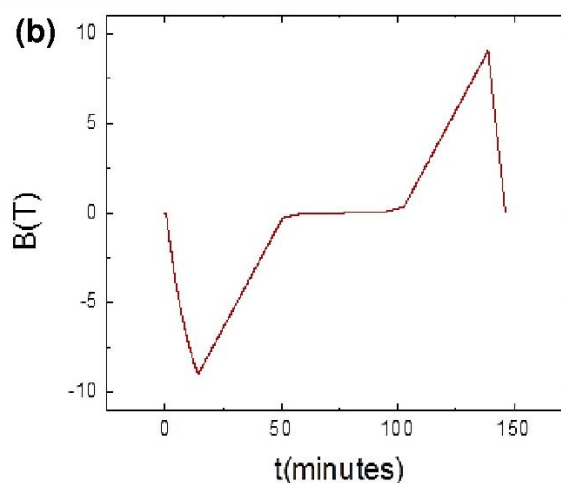
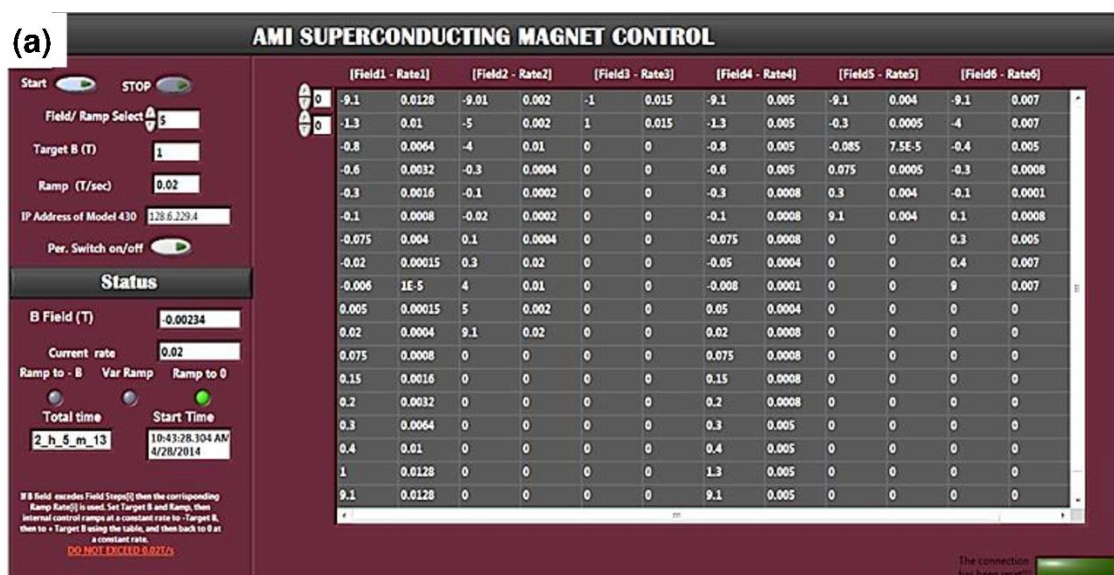


Fig. 3-5. Variable magnetic field ramp rate program. **(a)** A screenshot of the LabVIEW program used to control the AMI magnet ramping rates. Different ramping rates for different magnetic field ranges can be set in the spreadsheet. **(b)** A plot of magnetic field vs time achieved using the program.

For careful measurements, we developed a LabVIEW program, where we can adjust ramp rates in different magnetic field ranges, as shown in Fig. 3-5a; a similar program is used for GMW electromagnet. As seen in Fig. 3-5b, first magnetic field is ramped up to -9 T using the maximum allowed ramping rate. In the next section, where field changes from -9 T to $+9\text{ T}$, different ramp rates are used as set in the

program spreadsheet. Finally, a constant ramp rate is used to reduce applied field to 0 T, at which point, the measurement stops.

3.2.2 Instrumentation

To minimize air doping, as soon as the sample is taken out of the MBE growth chamber, it is transferred to the measurement system. The sample holder was designed such that the same holder can be fitted into both AMI and GMW magnet systems. The first step in measuring the transport properties of the grown film is to ensure a good thermal contact between the sample and the sample holder. A double-sided copper tape (3M 1182) made from 1 cm wide soft copper foil of thickness $\sim 0.002''$ was used. The sample holder is cleaned using isopropyl alcohol (IPA) to make sure there is no glue residue or any other scum remaining on the surface, and then the copper tape is pressed onto the sample holder. The copper tape is cut into a size slightly less than the sample size of $1\text{ cm} \times 1\text{ cm}$, and while pressing onto the holder, care must be taken to ensure no air bubble is formed between the two. The sample is then firmly pushed into the tape by pressing down the sample edges using tweezers.

The next step is to make proper electrical contact, and after making contacts, it is important to check if the contact is Ohmic before putting the sample in the measurement system. For topological insulator, Bi_2Se_3 thin films, indium was found to make Ohmic contacts. Indium is a very soft and ductile metal, that allowed easy manipulation to form contact wires. Indium pellets were roughly flattened using pliers; a portion of which was then placed on a glass slide, where it was flattened using a copper rod (or any other smooth cylinder) to form very thin foil, thickness $< 0.005''$

(Fig. 3-6a). A sharp blade is then used to cut the foil into thin wires that can be picked up with fine tweezers. One end of the wire is gently placed on the sample, and the other on the sample holder's contact pad (Fig. 3-6). On pressing it with a toothpick, the indium wire sticks to the surface well enough to make a good thermal and electric contact. The leads are tested mechanically by gently nudging to ensure they are not coming off, and then tested electrically by measuring 2-point resistance using a multimeter; for Bi_2Se_3 samples, the typical resistance values are to the order of few hundreds of Ω to a few $k\Omega$.

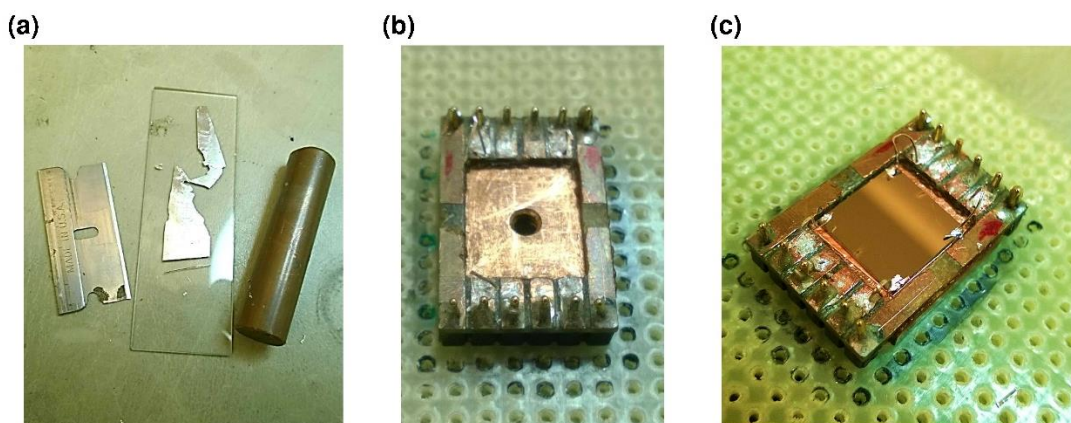


Fig. 3-6. Sample preparation for transport measurement. **(a)** Indium pellets are flattened, using a copper rod, to form a thin foil on a glass slide. A blade is then used to cut thin wires. **(b)** The sample holder used. **(c)** The sample attached to the holder, contacts are formed using Indium wires, and is ready for measurement.

The electrical measurements are conducted using a source meter in combination with an electrical switch system. Source meters used were single channel Keithley 2400, and dual channel Keithley 2626. Keithley 7001 was used as a electrical switch matrix, allowing a change in lead configuration in ~ 0.1 s. In the switch matrix, all the rows are electrically connected to all the columns via electro-mechanical relays; the sample leads were connected to the columns, and the source-

meter leads were connected to the rows. Depending on the resistance being measured, the LabVIEW program sends out a signal to the appropriate relays, thus allowing measurement of R_{xx} , R_{yy} , and R_{xy} , within one magnetic cycle, without needing to remake contacts on the sample itself.

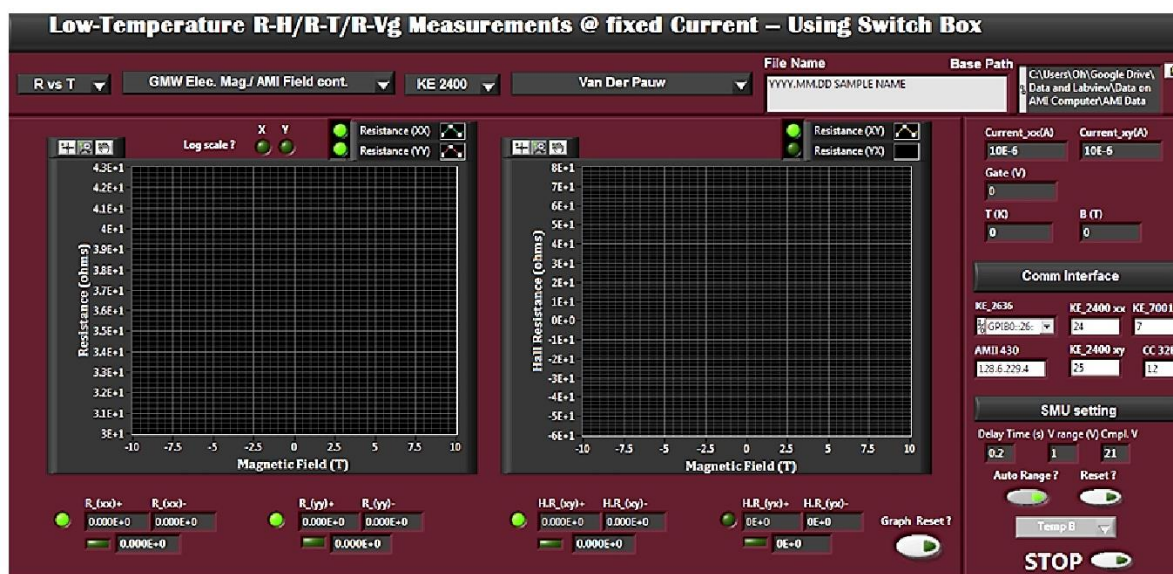


Fig. 3-7. A screenshot of the LabVIEW program designed to communicate with the source meters and switch matrix to perform transport measurements.

The various magnet control unit, source-meters, and switch matrix communicated with the computer via GPIB lines; a LabVIEW program (Fig. 3-7) was designed to communicate with the individual units and to automate the transport measurement process. The LabVIEW program was written in a way to provide various options for measurement of longitudinal and Hall resistance vs temperature, magnetic field, or gate voltage, and allowing to choose the magnet system and sample geometry.

3.2.3 Data Analysis

A very convenient method used in transport measurements is the reverse-field reciprocity relation, stating that for resistance measurements in $+B$ magnetic field, one can obtain the resistance for the reversed field ($-B$) by simply switching the voltage and current leads. For example, in $+B$ field, the measured resistance is $R_{12,34} = V_{34}/I_{12}$; if the resistance in an applied magnetic field of $+B$ is given as $R_{12,34}(+B)$, on reversing the magnetic field, the resistance becomes $R_{12,34}(-B)$, then the reciprocity theorem states that $R_{12,34}(-B) = R_{34,12}(+B)$. Using a switch matrix, such as Keithely 7001, switching the voltage and current leads is more convenient and less time consuming than reversing the magnetic field.

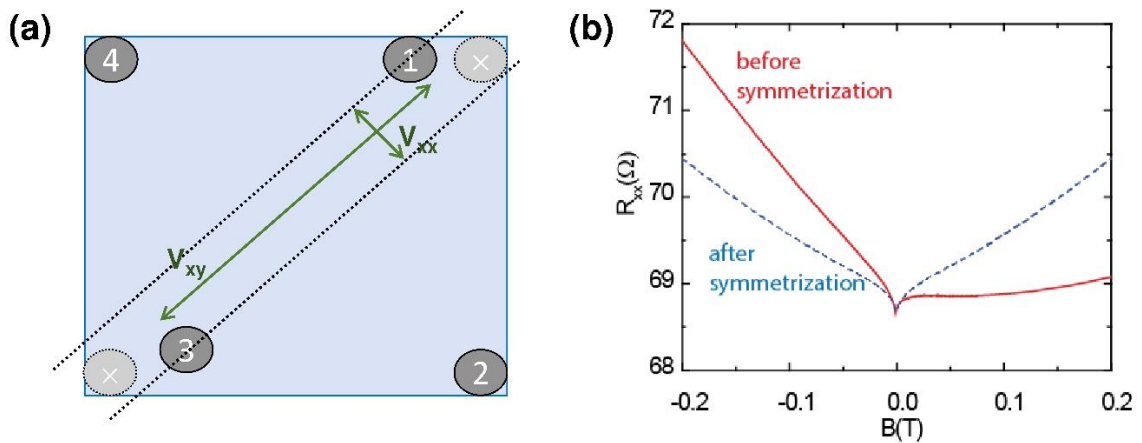


Fig. 3-8. A pictorial representation of the need for data symmetrisation. **(a)** A schematic showing how any unintentional mis-positioning of the contacts 1 and 3 leads to mixing of the longitudinal and Hall resistances. **(b)** Raw data (solid red curve) and symmetrized data (dashed blue curve) for R_{xx} vs B .

While measuring a sample in Van der Pauw geometry, although macroscopically the contacts are made on the sample corners, there is an inevitable misplacement of the leads, as seen in Fig. 3-8, resulting in an unavoidable mixing of

the longitudinal resistances, R_{xx} and R_{yy} , and the Hall resistance, R_{xy} . Thus, the experimental data contains a mix of transverse and longitudinal components of the resistance:

$$R_{Hall,measured} = aR_{xy} + bR_{xx(yy)}, \quad R_{xx(yy),measured} = cR_{xy} + dR_{xx(yy)}$$

where, coefficients a and d are close to unity, and coefficients b and c are non-negligibly small. In absence of magnetic field, the Hall resistance, $R_{xy}(= B/ne)$, is negligibly small, and $R_{xx(yy),measured}(B = 0) \approx R_{xx(yy)}$. However, as magnetic field increases, this Hall resistance component can no longer be ignored, resulting in a skewed data, as shown in Fig. 3-8b, thus, requiring a post-measurement data symmetrisation. The longitudinal resistance is an even function of the magnetic field, while the Hall resistance changes sign on reversing the field, thus, we can write:

$$R_{xx(yy),measured}(+B) = cR_{xy}(+B) + dR_{xx(yy)}(+B)$$

$$R_{xx(yy),measured}(-B) = cR_{xy}(-B) + dR_{xx(yy)}(-B) = -cR_{xy}(+B) + dR_{xx(yy)}(+B)$$

Assuming the coefficient, d , to be close to unity, we get:

$$R_{xx(yy)}(B) = (R_{xx(yy),measured}(+B) + R_{xx(yy),measured}(-B))/2$$

Similarly, for Hall data, we have: $R_{xy,measured}(+B) = aR_{xy}(+B) + bR_{xx(yy)}(+B)$, and

$$R_{xy,measured}(-B) = -aR_{xy}(+B) + bR_{xx(yy)}(+B).$$

Assuming $a \approx 1$, we get:

$$R_{xy}(B) = (R_{xy,measured}(+B) - R_{xy,measured}(-B))/2$$

Actual data for R_{xx} , R_{yy} , and R_{xy} is taken at certain B values; while sweeping the magnetic field, from $+9\text{ T}$ to -9 T , it is possible for exact field values to be slightly off for positive and negative fields. Thus, to symmetrize the experimental data, first we need to obtain corresponding resistance values at the negative magnetic field, as if magnetic field was swept from -9 T to $+9\text{ T}$. This is done by writing a numerical interpolation function script in the data analysis program, Origin.

Chapter 4. FLUX STABILITY AGAINST OXIDATION IN OXIDE - MBE ENVIRONMENT

Growth of multi-elemental structures in a required stoichiometry using MBE requires precise control of each source flux. However, in an oxide environment, this becomes a challenging task when the source materials have significantly different oxygen affinities, as in cuprate superconductors and multi-elemental transition metal oxides (²⁸Hellman *et al.*, 1994). Many of these oxides are composed of both alkaline-earth elements such as Sr, that oxidizes easily in low level molecular oxygen ($\sim 10^{-8}$ Torr) (²⁹Lettieri *et al.*, 2002) and transition metal elements such as Copper (Cu) which requires upto $\sim 10^{-5}$ Torr of ozone or atomic oxygen (³⁰Bozovic *et al.*, 1995; ³¹Oh *et al.*, 2006; ³²Oh *et al.*, 2005; ³³Locquet *et al.*, 1994). However, for easily oxidized elements such as Calcium (Ca), Strontium (Sr), Barium (Ba), Titanium (Ti), exposure to the highly reactive atomic oxygen or ozone oxidizes the source material so much that it leads to flux instability. Theis and Schlom studied the flux rate for a Ti source and found that while it remains fairly stable when subjected to an ozone background pressure of 2×10^{-6} Torr, it dropped by 2.5%/h when the ozone pressure was increased to 5×10^{-5} Torr (³⁴Theis *et al.*, 1996). Similarly, Ba was observed to show more than 50% flux drop under similar oxidation conditions (³⁵Theis *et al.*, 1997).

For a reliable growth, real-time flux monitoring scheme such as atomic absorption spectroscopy (AA) is required to control the flux variation to less than 1% (³⁶Klausmeier-Brown *et al.*, 1992; ³⁷Kasai *et al.*, 1997). However, as the number of elements grows, the complexity of the growth process increases and also becomes cumbersome to implement.

Sr being the primary alkaline earth element in various complex oxides, we use Sr as a probe to investigate the flux-stability issue over several hours of projected growth in harsh oxidation condition. In this chapter, we focus on finding the optimal source conditions for easily oxidized elements to achieve less than 1% flux variation.

4.1 Flux, Geometry, and Pressure Dependence¹

The source port was modified from SVTA's standard design to allow two source-to-substrate distances: 21 cm for the standard and 42 cm for the extended port geometry as measured between the substrate to the orifice of the source crucible (Fig. 4-1a). The effusion cell axis was at an angle of 33° to the substrate normal. Stability of the source temperature was better than 0.1 °C, and flux drift was less than 1% over several hours when no oxygen was introduced, except right after the sources were charged.

Fig. 4-1b shows the effect of source temperature, source- to-substrate distance, and source type (unmelted and pre- melted) on flux, measured by QCM. The flux depends exponentially on cell temperatures. The extended port, having twice the

¹ This section is based on the work published in ⁴⁷Y-S. Kim, N. Bansal *et al.*, Journal of Vacuum Science & Technology A **28**, 271 (2010).

distance between the source and the substrate as compared to the standard port, provided four times less flux value. The larger effective surface area of the unmelted source as compared to the pre-melted one contributed to an increase in flux. The flux stability of all these configurations was studied under various oxygen conditions.

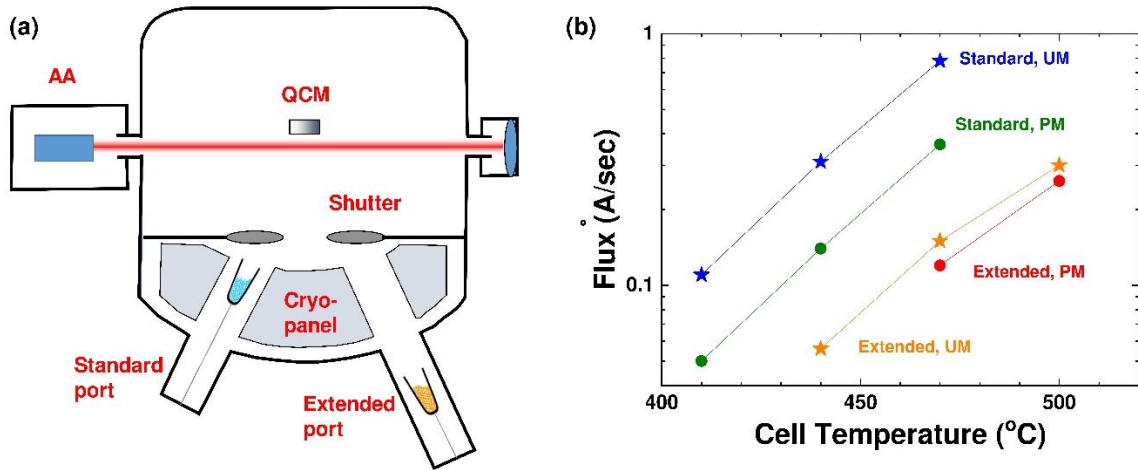


Fig. 4-1. (a) Schematic diagram of the oxide-MBE system. The source port allows two different source-to-substrate distances: 21 and 42 cm. (b) Sr flux (measured without oxygen) vs temperature for all configurations. PM stands for premelted and UM, unmelted. The effects of source temperature, source-to-substrate distance, and source type (unmelted and premelted) on flux can be seen.

Figs. 4-2a and 4-2b show the effect of flux scattering in an argon environment.

The source-to-substrate distance was a key factor in determining the extent of the flux scattering from the surrounding gas – the longer the distance, the more the scattering. This process can be well described by the Beer–Lambert law. The transmission probability of a beam of flux through a gas environment can be written as

$$\frac{I}{I_0} = e^{-\sigma n L} = e^{-L/\lambda} = e^{-\sqrt{2}\pi d^2 P/k_B T}$$

where I_0 and I are the intensities of the flux at the base pressure and the measurement pressure, respectively. σ is the effective cross sectional area of the colliding gas species, n is the number of gas particles per unit volume, λ is the mean free path (³⁸Herman *et al.*, 1989), L is the distance between the source and the substrate, k_B is the Boltzmann constant, T is the temperature, and d is the diameter of the gas particles. The result of this theoretical model, with $d=(r_{Ar}+r_{Sr})=3.1$ Å and $T=300$ K, is consistent with the measured QCM-flux data in Ar environment (Figs. 4-2a and 4-2b). Even in the absence of any source oxidation, the measured short-term flux-stability curves (the pressure dependence) shown in Figs. 4-2a and 4-2b could never be higher than the Ar curve from the same source geometry because beam scattering would still exist regardless of source oxidation. In other words, the difference between each oxygen curve and the corresponding Ar curve should be considered the source oxidation effect.

Interestingly, QCM and AA provided quite different flux values at higher gas pressures: AA tends to overestimate the flux as compared to the value given by QCM. The crystal sensor of QCM is mounted at the growth position and the flux collecting area (diameter of 0.8 cm) is similar to that of a standard substrate. Thus, QCM provides the actual amount of Sr being deposited on the substrate. But AA detects all Sr atoms present in the path of the light even those outside the substrate area. If the atomic beam coming from the source broadens due to scattering by gas molecules, it can still contribute to the AA flux signal, thus resulting in larger value than what QCM would provide. The magnitude of this overestimated flux value in AA depends on the details of geometrical alignment between the light and the source beam. This

suggests that care should be taken in interpreting AA signal as proportional to the beam flux. We then introduced molecular oxygen to study short-term and long-term flux stabilities in an oxidizing environment for both the standard and the extended ports.

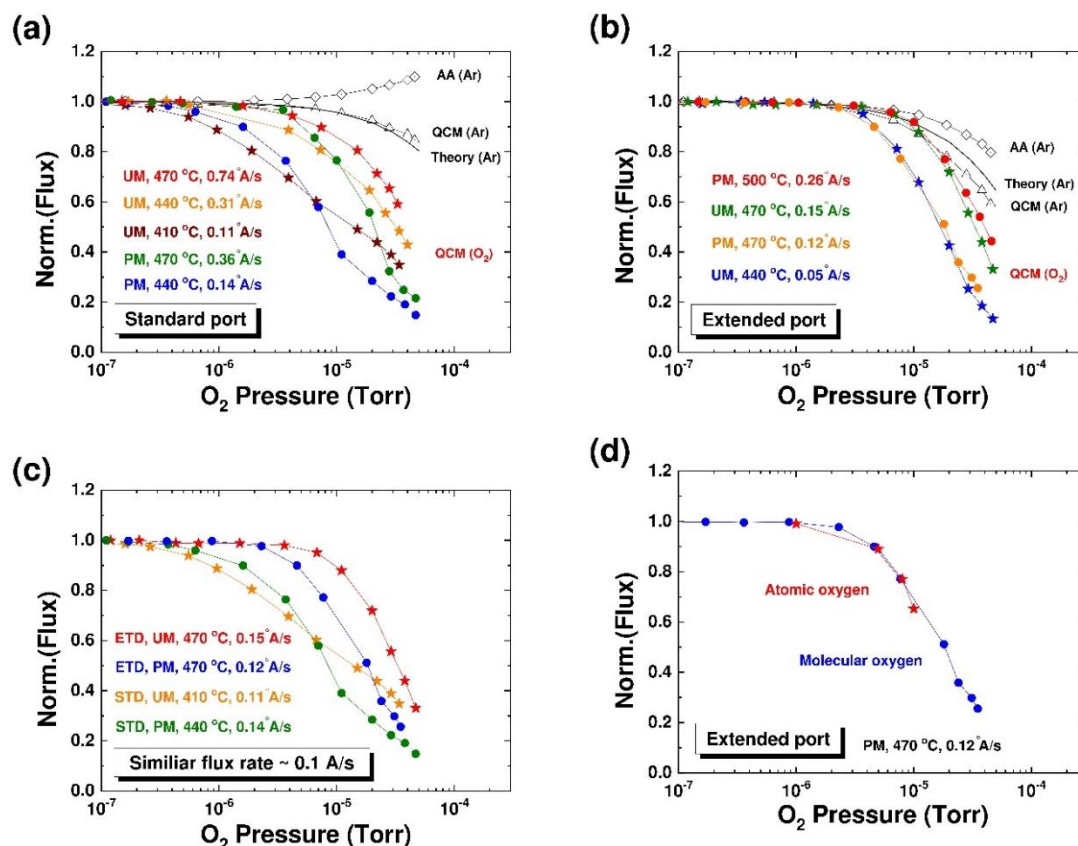


Fig. 4-2. Short-term flux stability in argon and oxygen environment for **(a)** standard port, **(b)** extended port, and **(c)** similar flux conditions: the flux values in the legend were measured at base pressures. Pressure dependence of the argon curves is completely due to beam scattering, and source oxidation accounts for the difference between the oxygen curves and each argon curve. Higher flux resulted in superior short-term stabilities. AA tends to overestimate the flux as compared to QCM at higher gas pressures. **(d)** Comparison of atomic and molecular oxygen: all other conditions were the same. There is no observable difference between the two.

For the short-term stability, oxygen pressure was increased from 1×10^{-7} to 5×10^{-5} Torr in steps and the corresponding flux was recorded for 1.5 min at each pressure. Lettieri et al. studied the degree of oxidation of Sr as a function of oxygen

partial pressure and found that the Sr being deposited on the substrate, at a deposition flux of 7×10^{13} Sr atoms/cm²s (~ 0.4 Å/s), starts to partially oxidize at pressures less than 3×10^{-9} Torr and completely oxidizes at a pressure of $\sim 8 \times 10^{-8}$ Torr (²⁹Lettieri *et al.*, 2002). For most of our measurements, the Sr flux was less than this, so the Sr being deposited at the substrate was fully oxidized in our oxygen pressure range. The long-term source stability was tested by continuously monitoring the flux over 4 h, keeping the oxygen pressure constant at 1×10^{-5} Torr, a common pressure toward high side for oxide-MBE growth. The source shutter was opened after oxygen was introduced into the chamber. We started recording the data an hour after opening the source shutter, allowing the crystal sensor to reach its thermal equilibrium.

As shown in Fig. 4-2, Sr flux decreases on increasing the oxygen pressure. It can be explained by the oxide layer formed at the source surface. The vapor pressure of the oxide (SrO) is negligible at temperatures below 1600 K (³⁹Lamoreaux *et al.*, 1987), so once the Sr source becomes oxidized, its vapor pressure starts to drop. This is also consistent with a previous report by Hellman and Hartford (²⁸Hellman *et al.*, 1994), who found that the flux of Mg, Ca, and Sr decreases exponentially with increasing oxygen pressure because of source oxidation. But in the case of Ba, its flux increases linearly with increasing oxygen pressure, implying that Ba surface oxide is unstable unlike the other alkaline earth oxides.

In either case, source oxidation for alkaline earth elements results in significant changes in their flux, and thus has to be minimized in order to maintain stable fluxes. Irrespective of the geometrical configuration and source type, higher

flux resulted in superior short-term and long-term stabilities. For the long-term stability, when the flux was higher than 0.3 \AA/s , the flux drift was less than 1%, our target value (Fig. 4-3a). If we compare the cases with similar flux values, the unmelted and the premelted showed similar long-term stabilities (Fig. 4-3a) even if the former was a little better in the short-term stability as shown in Fig. 4-2c.

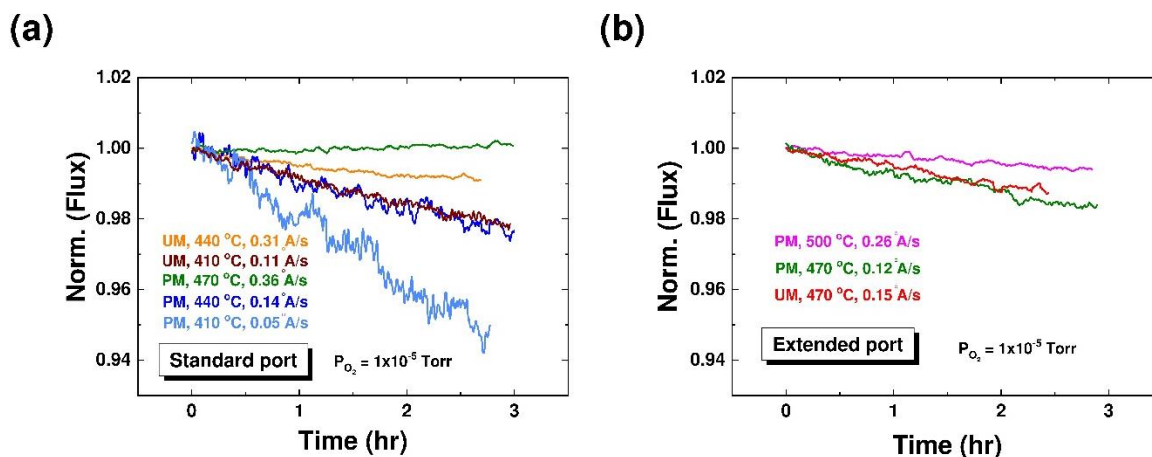


Fig. 4-3. Long-term flux stability for **(a)** standard port, and **(b)** extended port. The extended port showed better stability than the standard port at comparable fluxes.

The extended port performed better in both short-term and long-term stabilities than the standard port. In the long-term test with a flux of $\sim 0.1 \text{ \AA/s}$, the extended port suffered from only 1.5% drop in flux, compared to 2.5% in the standard port (Fig. 4-3). A number of factors are responsible for this difference. First, the larger source-to-substrate distance for the extended port requires a higher vapor pressure at the source level to maintain a similar flux at the substrate, and this in turn contributes to reduced source oxidation at the source level. Second, unlike in the standard port, in the extended port Sr atoms are continuously deposited on the port wall of length of 23 cm and diameter of 6 cm in front of the source (Fig. 4-1a) and they work as an effective oxygen getter. As a result, the oxygen partial pressure near the

source should be lower for the extended port than for the standard port. Thus, the higher source vapor pressure in coalition with the lower oxygen pressure near the source makes the Sr flux more stable for the extended port as compared to the standard port.

Additionally, we investigated the difference in source oxidation between atomic and molecular oxygen with the extended port, at a flux of 0.12 \AA/s . Quite surprisingly, there was no difference between the two (Fig. 4-2d), although we initially expected that atomic oxygen would result in more noticeable source oxidation considering its stronger reactivity. This observation implies that oxygen atoms transform almost completely into molecular oxygen by the time they reach the Sr source, which is not in direct line of sight of the atomic source. We confirmed this scenario by a residual gas analyzer (RGA): when the RGA was located outside the line of sight of the atomic source, both molecular and plasma oxygen exhibited an identical spectrum; a line-of-sight measurement from a similar unit showed up to 70% dissociation efficiency (⁴⁰Kearns *et al.*, 2001). This is in contrast to the other popular strong oxygen source, ozone, which does not completely transform to the molecular oxygen even after multiple scattering from the chamber walls according to our previous experience.

Furthermore, depth of the source inside the crucible, defined as the distance from the top surface of the source material to the crucible orifice, influenced the short-term flux stability. Fig. 4-4a shows the dependence of the short-term stability at comparable fluxes on the depth of the source. Overall, source oxidation occurred more significantly at larger depths. This phenomenon can be understood by the

following scenario. Sr flux being deposited on the substrate (or QCM crystal) is composed of two contributions: one directly from the source surface and the other bounced from the crucible wall above the source surface. In other words, the crucible wall works as a secondary source with much larger surface area than the primary source area. As the depth of the source increases, the contribution from this secondary source becomes more pronounced. Large surface area of the secondary source increases the probability of Sr meeting the incoming oxygen molecules leading to easy oxidation of these Sr atoms.

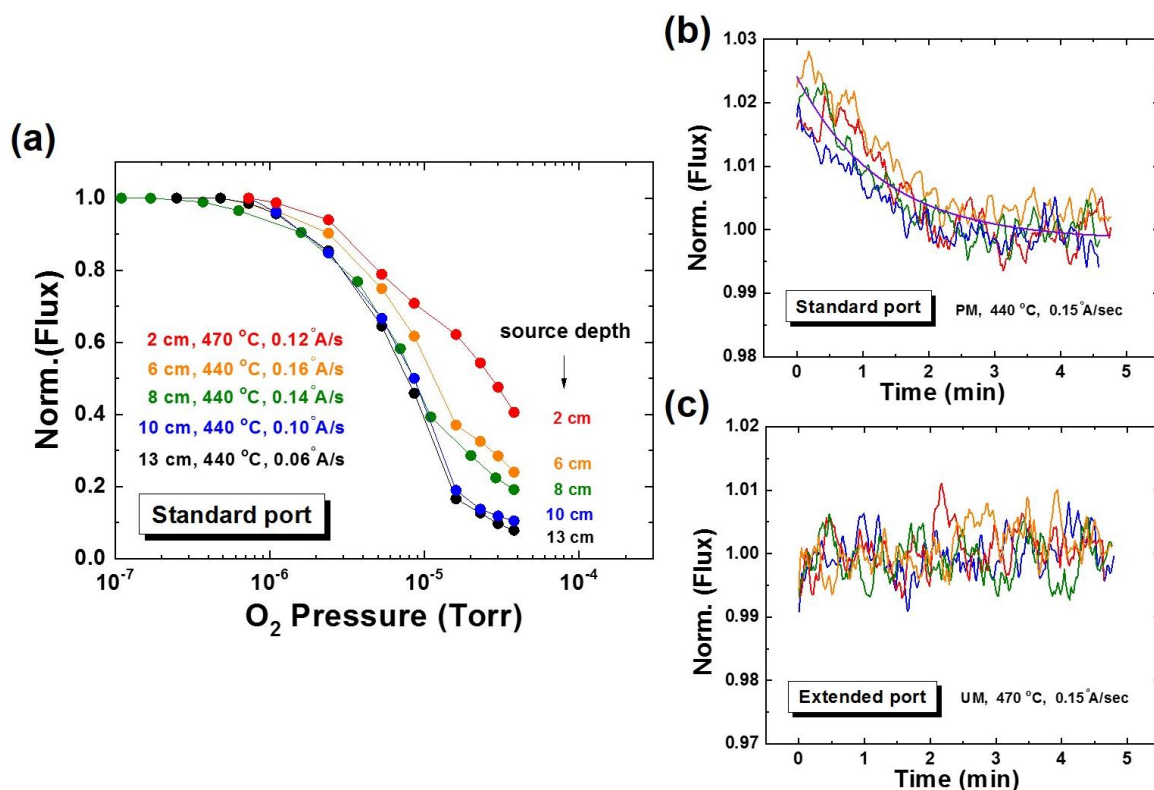


Fig. 4-4. (a) Short-term flux stability at comparable fluxes for different depths of the source. Source oxidation became more pronounced with increased source depth, suggesting that there is preferential oxidation on the crucible wall of the source. Flux transient at (b) standard port and (c) extended port. The standard port showed ~2% shuttering transient, whereas the extended port did not show any observable transient.

This explains why the oxygen-pressure- dependent Sr flux drop is more significant for larger source depths. It also implies that in an oxide-MBE environment, even regular source consumption will lead to a faster long-term flux drop than is expected from source consumption alone. Any solution for the source oxidation problem should properly handle this crucible wall issue as well.

Finally, we studied the flux transient effect related to source shuttering using atomic absorption spectroscopy (AA): AA is a better technique than QCM for this type of measurement because AA does not suffer from the thermal transient as QCM does. Opening and closing the source shutter is the primary method to control the amount of source material deposited on a substrate in MBE. But on/off control of the shutter introduces flux transients (⁴¹Miller, 1992;⁴²Turner *et al.*, 1990) resulting in a poor control of composition when frequent shuttering is required. A closed shutter reflects the thermal radiation from the source back into the source, increasing the net source temperature. Due to this radiation and consequent rise in the temperature, the initial flux is always higher than the steady state value. To minimize such flux transient, ⁴³Maki *et al.* (1986) used a conical insert in the source crucible and ⁴⁴Celii *et al.* (1993) modified the cell temperature before and after opening the shutter. Our source shutter is designed to have an angle with the cell in order to reflect most of the radiation away from the source. Still, there was an observable flux transient associated with the standard port because of the short distance between the source and the shutter (4cm). The initial flux right after shutter opening was 2% (0.003 Å/s) higher than the steady state value (0.15 Å/s) at a cell temperature of 440 °C (Fig. 4-4b). The time constant of this flux transient was 1.3 min and it took ~2 min to reach

the steady state after opening the shutter. The extended port did not exhibit such a flux transient because of the long shutter-to-cell distance (25 cm) (Fig. 4-4c).

4.2 Crucible Aperture²

Based on our understanding of the source oxidation problem from the study so far, as mentioned in the previous section, we devised a simple crucible aperture scheme as a way to minimize the source oxidation. The aperture insert is a disk having a hole at the center. It minimizes the source area that is exposed to the oxygen species and blocks out most of those coming directly to the source. So far, various kinds of crucible inserts have been proposed for different purposes in conventional semiconductor MBE systems. ⁴³Maki *et al.* (1986) proposed a conical insert to eliminate the flux transients, ⁴⁵Thorpe *et al.* (1991) used a tilted conical insert to improve thickness uniformity of GaAs epitaxial layers, and ⁴⁶Sacks *et al.* (1996) reported stacked disk inserts to reduce visible defect densities. However, no such studies have been reported for an oxide-MBE process, and in this section, we study the crucible aperture as an easily implemented and very effective way to minimize source oxidation in the oxide-MBE environment.

We employed various types of apertures to study the effect of the crucible aperture on flux stability. Two different materials (alumina and tantalum) and three different aperture diameters (1.5, 3.1, and 5.0 mm) were employed, alumina apertures were provided by SVTA, and tantalum apertures were homemade. The

² This section is based on the work published in ¹²⁸Y.-S. Kim, N. Bansal *et al.*, *Journal of Vacuum Science & Technology A* **28**, 600 (2010).

thickness of alumina aperture was 1 mm and that of tantalum was 25 μm . The tantalum apertures had small cuts approx. 2 mm apart and 5 mm deep around the circumference for flexibility and thus could be positioned at almost any depth in the crucible; see Fig. 4-5. For alumina apertures, two alumina rings were used to fix the aperture insert at a desired position, and because of their rigidity, the mounting position of the alumina aperture was relatively limited compared to the tantalum one.

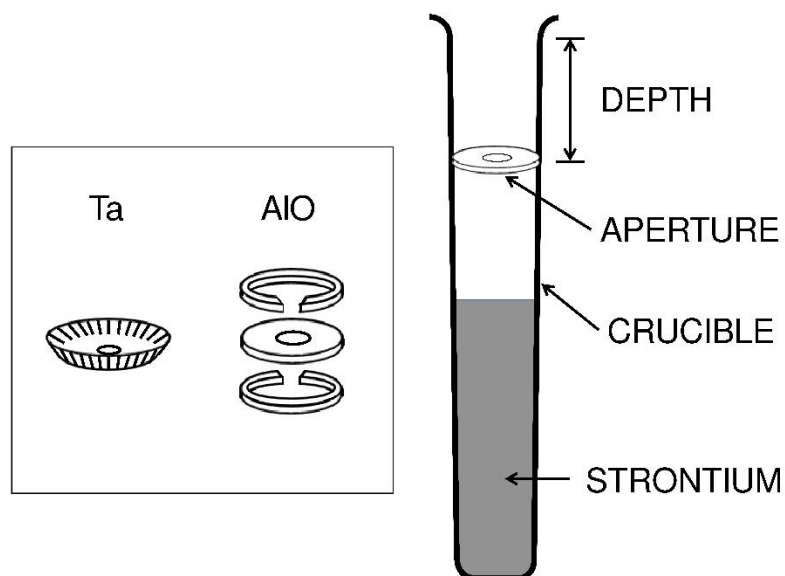


Fig. 4-5. Schematic diagram of the alumina and tantalum aperture inserts. While the alumina insert was mounted with two rings, the tantalum insert was fixed into a position by its elastic force.

Fig. 4-6a shows the effect of the aperture depth and its size on short-term flux stability. First, we note that at a fixed aperture depth of 3.5 cm, the source temperatures necessary to provide similar flux values strongly depend on the insert type. With the alumina insert, the source temperature had to be significantly raised to obtain a flux value comparable to the one without any aperture, and this can be easily explained by the reduced source area due to the small aperture. But with the tantalum insert, the flux remained almost unchanged from the value of a non-

apertured crucible at the same source temperature. This implies that tantalum, being a metal, reflects most of the thermal radiation from the hot source back to the source surface and raises its effective temperature, resulting in enhanced flux, and this effect offsets the reduced source area. Fig. 4-6a also shows that with the same insert type, as the insert got closer to the crucible orifice, maintaining comparable fluxes required higher source temperatures; this is because the temperature of the insert drops near the orifice. Obviously, smaller aperture size also resulted in reduced flux. In terms of oxygen pressure dependence, Fig. 4-6a shows that the aperture depth is the most critical factor – the deeper the aperture is, the more sensitive the flux is to the oxygen pressure. As reported in the previous section, as the insert depth increases, the flux contribution from the crucible wall as a secondary source also increases and this results in a more severe short-term source oxidation.

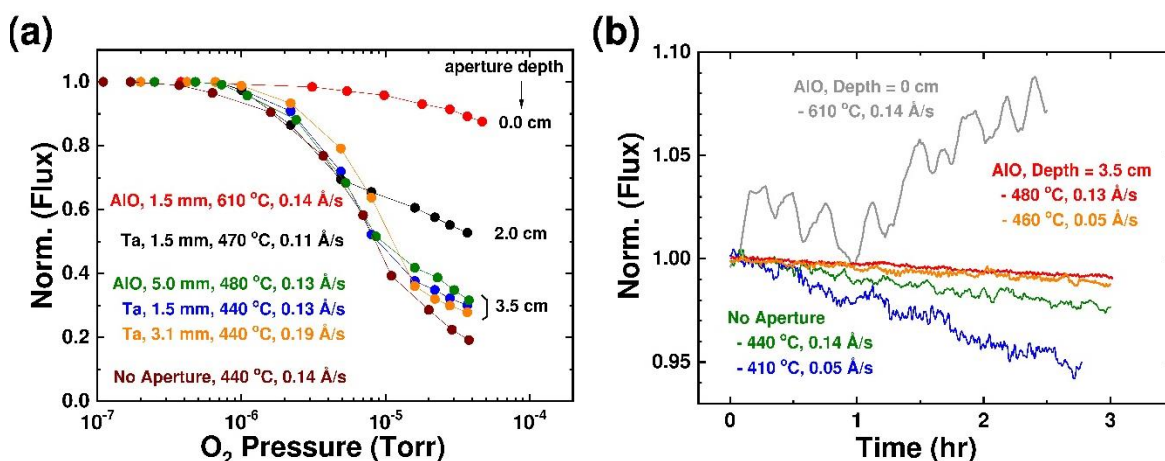


Fig. 4-6. (a) Dependence of the short-term stability on the aperture depth at comparable flux values. Source oxidation occurred more significantly as the insert depth increased. But when the insert was mounted near the crucible orifice, material build-up occurred underneath the aperture, as shown in (b). (b) Long-term flux stability for crucibles with and without an aperture insert. The crucible with an aperture insert, positioned at an optimal depth, exhibited significantly better stability than the one without an insert. But when the insert was positioned too close to the orifice, the flux became unstable as the topmost curve shows.

With respect to the source oxidation, Fig. 4-6a shows that the insert positioned at the crucible orifice gives the best performance. In this case, however, severe material build-up occurred underneath the aperture. Lower temperature of the crucible orifice than that of the source surface is the main cause for this problem. This material build-up choked the aperture and induced serious fluctuation and drift in the source flux, as shown in Fig. 4-6b. The fluctuation amplitude was about 2% of the flux value and the drift was more than 8% during 3 h operation. Furthermore, the build-up required a significantly higher source temperature to maintain a similar flux value. But the increase in the source temperature worsens the situation because higher temperature accelerates the build-up process. After finishing many hours of long-term stability test, we found that the entire Sr source in the crucible was condensed underneath the aperture insert. With our hot-lip cell, the aperture insert had to be positioned deeper than 3 cm to prevent this problem. But when it is too deep, the crucible wall above the aperture works as an easily oxidizing secondary source as mentioned above. Because the best source stability requires no material build-up and minimum source oxidation, 3.5 cm was chosen as the optimal depth of the aperture insert. With this optimal aperture configuration, we tested long-term flux stability over 3 h, as shown in Fig. 4-6b. The crucible with an aperture insert (alumina, opening diameter=5 mm, depth=3.5 cm) exhibited significantly better flux stabilities than the one without an aperture. For example, in 10^{-5} Torr of molecular oxygen, while the crucible without an insert exhibited 5.5% decrease in Sr flux at a growth rate of $\sim 0.05 \text{ \AA/s}$, the one with an insert showed only 1.2% reduction over the same period (Fig. 4-6b). This implies that the insert improved the flux stability

more than four times. At a higher growth rate of $\sim 0.13 \text{ \AA/s}$, which is still slower than a typical growth rate, the flux variation was less than 1% over a 3h period. Considering that source oxidation becomes weaker as the growth rate increases, the aperture scheme will provide flux stabilities much better than 1% at typical growth rates.

4.3 Self-gettering Differential Pump³

Based on the results as discussed in the previous sections, we came up with a more powerful and effective scheme to enhance the flux stability, by using a collimator in an extended port geometry. The collimator minimizes the source area exposed to oxygen species like the crucible aperture and its long walls act as an effective oxygen getter like the extended port geometry.

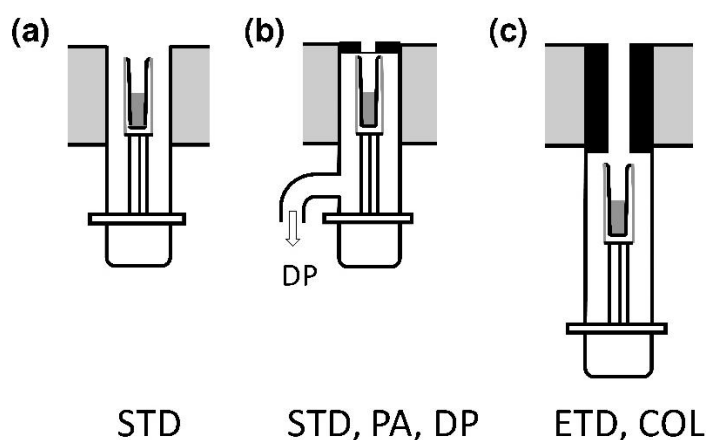


Fig. 4-7. Cross sections of **(a)** STD, **(b)** STD with PA and DP, and **(c)** ETD with collimator (COL).

³ This section is based on the work published in ¹²⁹Y.-S. Kim, N. Bansal *et al*, Journal of Vacuum Science & Technology A **29**, 041505 (2011).

This self-gettering differential pump uses the source itself as a pumping medium to eliminate the source oxidation problem and stabilize the flux even when the flux is as low as $\sim 0.01 \text{ \AA/s}$, which is an order lower than the typical growth rate. Two source ports designed with different geometry were used: the standard port (STD) (Fig. 4-7a), which is typical in most MBE systems, and the extended port (ETD) which is 21 cm longer than standard port (Fig. 4-7c). One of the standard ports was modified for differential pumping (DP) using a port aperture (PA), mounted in front of the source, and connected to turbo pump on side of the source port (Fig. 4-7b). The purpose of this differential pumping is to minimize the oxygen partial pressure near the source by mechanically pumping it through the turbo pump, as discussed later in detail. The port aperture with an inner diameter of 1.5 cm and a thickness of 3 mm is designed for easy insertion/ removal using a few screws. A gate valve is inserted between the source port and the turbo pump to enable or disable differential pumping. In addition, an ion-gauge is mounted on the source port to read the gas pressure near the source. In the extended port geometry, a homemade collimator (inner diameter: 1.5 cm and length: 19 cm) is mounted in front of the source. We investigated flux stability against oxygen rich conditions for all of these port geometries to find out the most effective configuration for minimizing source oxidation issues.

Short-term flux stability for the standard port and the extended port with various geometrical configurations, as discussed above, is shown in Fig. 4-8. These measurements were done in both oxygen and argon environment, because the measured flux signals are affected not only by the source oxidation but also by the

scattering effect (⁴⁷Kim *et al.*, 2010). From the flux scattering measurements conducted in the argon environment, it was found that the source scattering was dominated by the source-to-substrate distance (standard port: 21 cm, extended port: 42 cm), and not affected by other parameters such as flux rate, port aperture, collimator, and differential pumping.

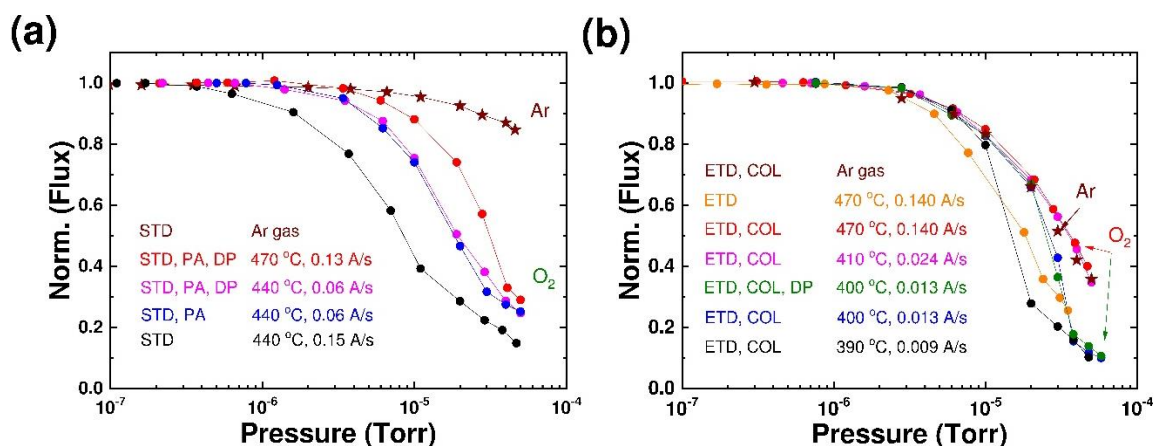


Fig. 4-8. Short-term flux stability for **(a)** standard port with/without PA and DP and **(b)** extended port with/without COL and DP at various flux rates.

This scattering process can be well described by the Beer–Lambert law (⁴⁷Kim *et al.*, 2010). Introducing oxygen gas into the chamber resulted in serious source oxidation in the standard port configuration and the flux decreased significantly at higher oxygen pressures (Fig. 4-8a). After mounting a PA in front of the source, it was observed that the flux rate dropped from 0.15 to 0.06 Å/s. Even at this low flux rate, an enhancement in the short-term flux stability was observed. Using differential pumping through the turbo pump, connected to the back end of the source port, provided almost no additional improvement. In order to achieve similar flux rates to give a better comparison with the standard port, the source temperature was increased; it was observed that even though a significant improvement in flux

stability was achieved at lower oxygen pressures, the problem still exists as the oxygen pressure is increased beyond 3×10^{-6} Torr. The short-term flux stability for the extended port with/without collimator and differential pumping is shown in Fig. 4-8b. At a similar flux rate, the extended port resulted in a comparable trend to that of a standard port with port aperture and the differential pumping. When the collimator is added to the extended port, interestingly, it was seen that the source was free from source oxidation issues even at an oxygen pressure as high as 5×10^{-5} Torr. The short-term flux stability in this configuration was limited by the scattering of flux at higher pressures in a confined space along the collimator length, as seen by the measurements in Ar environment. At an O_2 pressure of $\sim 1 \times 10^{-5}$ Torr, the flux was seen to be fairly stable with flux rates, as low as 0.01 \AA/s , which is considerably lower than the typical growth rate in an MBE process.

To investigate long-term flux stabilities, we monitored both Sr flux and oxygen partial pressure in the source port for several hours, keeping oxygen pressure in the main chamber to be 1×10^{-5} Torr. In a standard port without PA and DP, upon introducing oxygen in the growth chamber, the oxygen pressure inside the source port increased suddenly resulting in an abrupt, followed by a continuous, drop in the flux rate. A port aperture on the source port lowered the oxygen conductivity and the O_2 partial pressure in the source port increased slowly to its equilibrium value; a similar trend is observed for the drop in the flux rate (Figs. 4-9a and 4-9c). It took ~ 30 min (~ 1.5 h) for O_2 partial pressure and the flux rate to reach an equilibrium state with (without) differential pumping at the source port (Figs. 4-9a and 4-9c).

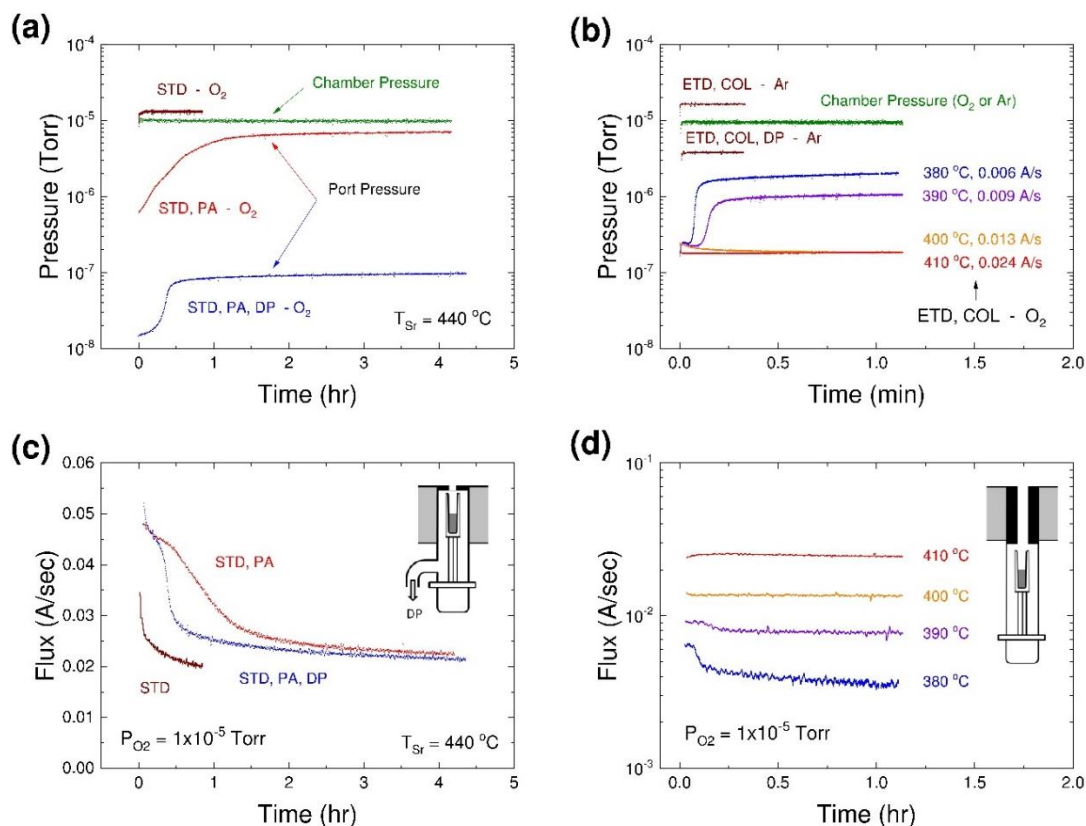


Fig. 4-9. Time dependence of oxygen pressure near Sr source at **(a)** standard port and **(b)** extended port with various geometrical configurations when the oxygen partial pressure in main chamber is kept 1×10^{-5} Torr. Long-term flux stability of **(c)** standard port and **(d)** extended port.

Beyond this, the oxygen pressure still increased without reaching a saturation point, causing the flux to decrease continuously. Considering that our goal is to make the flux drift less than 1% over several hours of growth, this long time delay to reach the equilibrium state and the continuous decrease of flux are not desirable. This result implies that even if the oxygen molecules in the source port were pumped out mechanically through the turbo pump, the oxygen partial pressure near the source was not low enough to prevent the source oxidation problem.

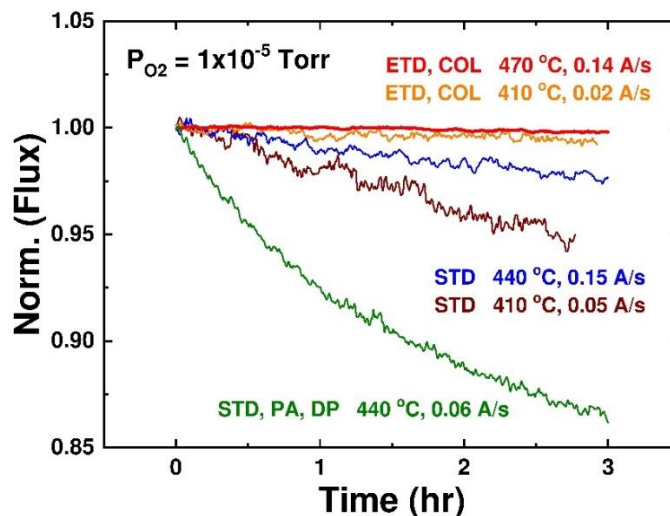


Fig. 4-10. Normalized long-term flux stability for the extended port with collimator and the standard port with/without port aperture, differential pumping. In extended port with collimator, the flux variation over 3 h is less than 1% even if the flux rate is much slower than typical growth rate while that of standard port is more than 2% even with higher growth rate. The standard port with PA and DP shows the worst performance; over 3 h, flux drops by more than 10%, implying any improper differential pumping is worse than having none.

To the contrary, in the extended port with a collimator, good long-term flux stabilities were observed, even without mechanical pumping; oxygen pressure near the source quickly saturated within minutes to an equilibrium value even at very low flux rate $\sim 0.013 \text{ \AA/s}$, which is ~ 10 times lower than typical growth rate (Figs. 4-9b and 4-9d). The flux had to be extremely low (below 0.009 \AA/s) to observe source oxidation, at a much reduced scale compared to a standard port with port aperture and differential pumping. This powerful enhancement in flux stability for a collimator mounted extended port can be explained in the following way: once the source is heated, the source atoms are deposited continuously on the wall of the collimator. Because of the long length and the large surface area of the collimator, most of the oxygen species coming into the source port stick to the collimator wall, due to a chemical reaction with Sr (forming strontium oxide), without reaching the source

itself. This gettering effect reduced the effective oxygen conductance through the collimator by a factor of 1000 compared to its geometric conductance for our chosen geometry (inner diameter: 1.5 cm and length: 19 cm) resulting in an effective oxygen partial pressure near the source well below the source oxidation regime and stabilizing the source flux over a long period of time, even at high oxygen pressures in the growth chamber. As shown in Fig. 4-10, the flux drift was negligible, less than 1%, for 3 h which is a typical operating time in an oxide-MBE process.

A trade-off would be required between achieving this high level of source stability and deposition uniformity over large samples and the exact dimensions of the collimator would have to be optimized. However, for a collimator of this dimension, no sign of choking was observed on the collimator wall even after more than 100 h of operation, further demonstrating its effectiveness. This self-gettering pump scheme was tested with Sr but it should work in a similar way for any other easily oxidizing elements and provide a powerful solution for the source oxidation problem in an oxide-MBE system.

Chapter 5. MBE GROWTH & TRANSPORT PROPERTIES OF Bi_2Se_3 ON Si (111)

Amongst the materials being pursued as TI, Bi_2Se_3 stands out because it has almost the largest bulk band gap of 0.3 eV, and a simple surface state structure of a well-defined single Dirac cone at the momentum zero point in k-space (⁴⁸Cheng *et al.*, 2010; ⁴⁹Zhang *et al.*, 2009; ⁵⁰Moore, 2009; ⁵¹Peng *et al.*, 2010;²⁴Xia *et al.*, 2009). In this chapter, we discuss an atomically sharp epitaxial growth of Bi_2Se_3 films on Si(111) without a disordered interfacial layer. Further, we will discuss the dependence of the bulk and surface transport properties in Bi_2Se_3 on the thickness of the sample covering up to three orders of sample thickness.

5.1 Epitaxial Growth of Bi_2Se_3 on Si(111)⁴

The sequence of Se–Bi–Se–Bi–Se forms a stack or quintuple layer (QL) along the c-axis direction of the Bi_2Se_3 rhombohedral structure. The bonding between different quintuple layers is weak van der Waals type, commonly associated with layered

⁴ This section is based on work published in ⁸⁹N. Bansal *et al.*, Thin Solid Films **520**, 224 (2011).

structures. However, the bonding within the stack or the Bi–Se bonding is stronger (⁵²Lind *et al.*, 2005; ⁵³Okamoto, 1994), enabling the film to grow QL-by-QL. Earlier methods to prepare Bi₂Se₃ films, such as electrodeposition (⁵⁴Torane *et al.*, 2001), solvo-thermolization (⁵⁵Wang *et al.*, 1999), successive ionic layer adsorption and reaction (⁵⁶Sankapal *et al.*, 2000), chemical bath deposition (⁵⁷Nkum *et al.*, 1998) etc. generally produce polycrystalline films; though suitable for thermoelectric studies, these are unsuitable for study as a thin film topological insulator; thus, making a need for a single crystal Bi₂Se₃ thin film acute.

Several molecular beam epitaxy (MBE) growth processes to obtain single crystalline Bi₂Se₃ films have been reported earlier on a variety of substrates such as Si(111) (⁵⁸Zhang *et al.*, 2009), vicinal Si(111) (⁵⁹Li *et al.*, 2010), graphene (⁶⁰Song *et al.*, 2010), SiC (⁶¹Zhang *et al.*, 2010), sapphire (⁶²Liu *et al.*, 2011), GaAs (⁶³Richardella *et al.*, 2010), SrTiO₃ (⁶⁴Chen *et al.*, 2010) etc. Among these, however, the growths on Si, the most important substrate in microelectronics, have been accompanied by disordered layers at the interface; one of the main problems being the reactivity of the Si surface. Si(111) substrates were un-doped with a room-temperature resistivity of $>10^3 \Omega\text{cm}$. Native oxide layer was removed from the Si(111) substrates by heating using graphite filaments. The substrate temperature was calibrated at the 7×7 to 1×1 Si(111) surface reconstruction temperature of 860 °C. To ensure uniform coverage, we rotated the substrate at 5 rpm during the growth and subsequent annealing in Se-atmosphere.

5.1.1 Substrate Preparation

The order and cleanliness of the substrate is an important parameter to consider when establishing the optimal MBE growth conditions, since any surface contamination would result in crystal defects or second phases in the epitaxial layers (⁶⁵Koma, 1992; ⁶⁶Ishizaka *et al.*, 1986). Since the beginning of Si MBE growth, most common method employed to clean the Si substrate has been a multi-cycle high-temperature flashing process or annealing up to ~ 1200 °C (⁶⁶Ishizaka *et al.*, 1986; ⁶⁷Becker *et al.*, 1977; ⁶⁸Bean, 1983; ⁶⁹Wei *et al.*, 2002); and all previous reports to grow thin films on Si used such high temperature cleaning methods (⁵⁸Zhang *et al.*, 2009; ⁷⁰Wang *et al.*, 2010). However, outgassing during the high temperature step can easily result in contamination of the reactive Si surface (⁶⁶Ishizaka *et al.*, 1986). Thus, this method of cleaning the substrate imposes a stringent requirement of very high vacuum of the chamber. During this work, we found that clean Si(111) surface can be obtained at a much lower temperature, with an aid of an ex situ UV (Ultra-Violet) ozone cleaning step. Highly reactive radical oxygen formed in the presence of UV light burns off the majority of organic compounds from the surface (⁶⁹Wei *et al.*, 2002). A substrate UV cleaned for 5 min before mounting in the ultra-high vacuum (UHV) chamber yielded a clean Si (111) 7×7 surface, as shown in Fig. 5-1a, after being heated for ~ 2 min in vacuum at a temperature below 900 °C, which is about ~ 300 °C lower than the more common flash desorption method; considering that substrate stages rated only up to 1000 °C are much more common than those rated up to 1200 °C, this lower temperature cleaning method has a big advantage on its own.

Another MBE growth concern is the presence of dangling bonds on Si surface, which act as active sites for adsorption of contaminants (⁶⁶Ishizaka *et al.*, 1986), and the reactivity of the silicon surface itself, which leads to a high probability of formation of second phases such as SiSe₂ at high temperatures, leading to a rough interface (⁵⁹Li *et al.*, 2010; ⁶⁰Song *et al.*, 2010). To chemically saturate the dangling bonds at the Si surface and to achieve better epitaxial growth, Wu *et al.* treated the interface by depositing Bi and then annealing it to form $\beta\text{-}\sqrt{3}\text{-Bi}$ surface (⁵⁸Zhang *et al.*, 2009). Besides them, many other groups have also used this technique to grow thin films on Si (⁵⁹Li *et al.*, 2010; ⁷¹Sakamoto *et al.*, 2010; ⁷²Hirahara *et al.*, 2010). Xie *et al.* deposited an initial thin seed layer of Bi₂Se₃ at a cryogenic temperature prior to further high temperature growth, but this resulted in the formation of a few nm-thick amorphous film at the interface and twinned domains (⁵⁹Li *et al.*, 2010).

To suppress the surface effect, we implemented a very simple scheme. Inspired by the report that Se atoms can be used as a passivation layer for the surface dangling bonds on GaAs (⁶⁵Koma, 1992), we exposed the Si substrate to Se flux over a span of few seconds prior to the growth; obtaining the unreconstructed Si(111) surface; however, the substrate temperature was critical for the success of this process. At too high temperatures, SiSe₂ phases develop, whereas at too low temperatures amorphous selenium layer grows (⁷³Bringans *et al.*, 1989). At a substrate temperature of ~ 100 °C, the deposition of Se on the Si surface was found to be self-limited without either forming thick Se or SiSe₂ layer; Se atoms bond only to the top Si atoms and after that no further Se gets deposited on the substrate, as verified by RHEED and TEM. Within seconds of exposure to Se, Si surface changed

from 7×7 reconstruction to 1×1 structure, as observed by RHEED; and no further change in the RHEED pattern occurred even if the substrate was further exposed to Se, implying that no further reaction between Se and Si or accumulation of Se occurs at this temperature. At temperatures below $\sim 70^\circ\text{C}$, Se accumulation occurred, and at temperatures above $\sim 200^\circ\text{C}$, Se started to react with Si substrate.

5.1.2 Basic Bi_2Se_3 Recipe

The next step in optimizing our MBE growth of Bi_2Se_3 was to find the temperature that favors good growth and at the same time limits the decomposition of the already deposited Bi_2Se_3 layers. On exposing the surface to Se flux at the right temperature described above, a monolayer of Se is formed on the surface. This monolayer of Se atoms provides a passivated coverage on the Si surface and also acts as the base for the Se–Bi–Se–Bi–Se stack. Owing to the high vapor pressure of Se at relatively low temperatures (⁷³Bringans *et al.*, 1989), the first attempt was made by growing Bi_2Se_3 films at a comparatively low temperature. Bi_2Se_3 growth for ~ 2.5 min in a temperature range of 100°C to 130°C resulted in weak streak-like diffraction patterns, indicative of poor crystalline structure as shown in Fig. 5-1b. Further growth at this low temperature resulted in a streaky diffraction pattern accompanied by a polycrystalline ring-like pattern, as shown in Fig. 5-1c. Thermally annealing the sample up to $\sim 250^\circ\text{C}$ resulted in brightening the specular spot, suggesting that annealing of Bi_2Se_3 aids in further crystallization of the film. However, growing directly on the higher end of this temperature range resulted in an even poor quality

of the film, implying that the substrate temperature was too high. In various other attempts on one-step growth, several substrate temperatures were used.

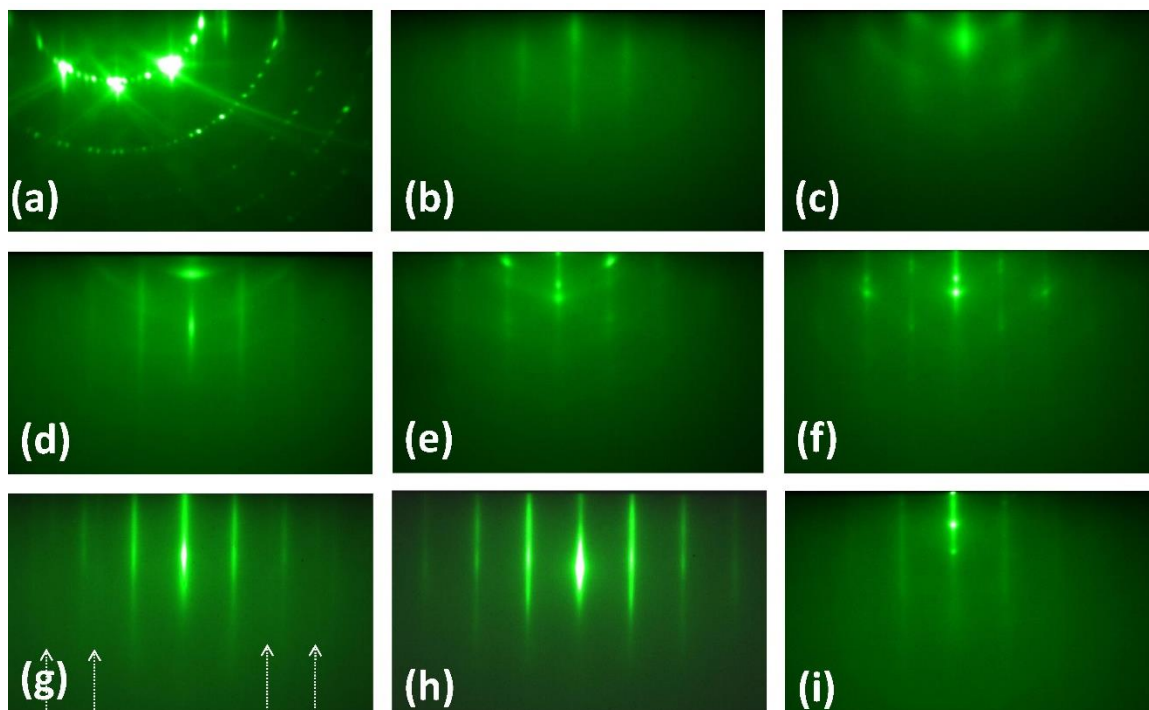


Fig. 5-1. RHEED patterns for different growth procedures. **(a)** Si 7×7 surface obtained by UV-ozone cleaning and heating in UHV chamber. **(b)** Low temperature growth at 110 °C for 2.5 min. **(c)** Continued low temperature growth for another 10 min. **(d-f)** Initial growth of ~ 2.5 min at high temperatures of 190 °C, 250 °C and 350 °C, respectively. **(g-i)** Two temperature growth with initial 2–3 QL deposition at 110 °C and higher temperature growth at 190 °C, 230 °C and 300 °C, respectively.

As shown in Fig. 5-1f, on depositing the initial film for ~ 2.5 min at a high substrate temperature of 350 °C, the surface of the grown film showed 3D spot-like features along with the diffraction streaks indicating that islands of second phases such as Bi_3Se_4 or SiSe_2 coexist with the crystalline-like Bi_2Se_3 film. Lowering the growth temperature to 250 °C to deposit Bi_2Se_3 resulted in similar island/cluster formation, shown in Fig. 5-1e. On lowering the temperature further to 190 °C and growing Bi_2Se_3 film for ~ 2.5 min, though no 3-D clusters were formed and sharper

streaks were achieved, it was accompanied with concentric ring-like patterns shown in Fig. 5-1d, indicating the crystallographic orientation of the film was highly disordered. Thus, we found that two-step growth temperatures were necessary to achieve second-phase-free high quality Bi_2Se_3 films on Si substrates right from the beginning. With a single-step high temperature growth, second phase clusters were formed, and with a low temperature growth, the crystalline quality of the films was poor even if the second phase was absent. Therefore, to avoid reaction with the silicon surface at higher temperatures, a very thin film ($\sim 2\text{-}3$ QL) is grown at a lower temperature ($100\text{ }^\circ\text{C} - 120\text{ }^\circ\text{C}$) at the initial stage and then to improve the crystallinity of the film, the rest of the growth is continued at a higher substrate temperature ($190\text{ }^\circ\text{C} - 250\text{ }^\circ\text{C}$). Fig. 5-1g shows the RHEED pattern for a Bi_2Se_3 film grown by the two-temperature process with the high temperature growth at $190\text{ }^\circ\text{C}$. Although the diffraction pattern shows crystalline growth, presence of faint streaks, as indicated by arrows, along with the main ones suggest that the film may have formed a twin structure, which has also been observed by other group previously (⁵⁹Li *et al.*, 2010). However, depositing Bi_2Se_3 at $220\text{ }^\circ\text{C}$ after initial low temperature growth resulted in very sharp streaky pattern, Fig. 5-1h, indicating that the film has an atomically flat surface morphology, and no indication of twinning was observed. Further increasing the growth temperature to $300\text{ }^\circ\text{C}$ resulted in the formation of second phase, as shown in Fig. 5-1i. Thus, using our two-temperature growth, we were able to obtain a twin-free atomically sharp interfaces, as verified by RHEED.

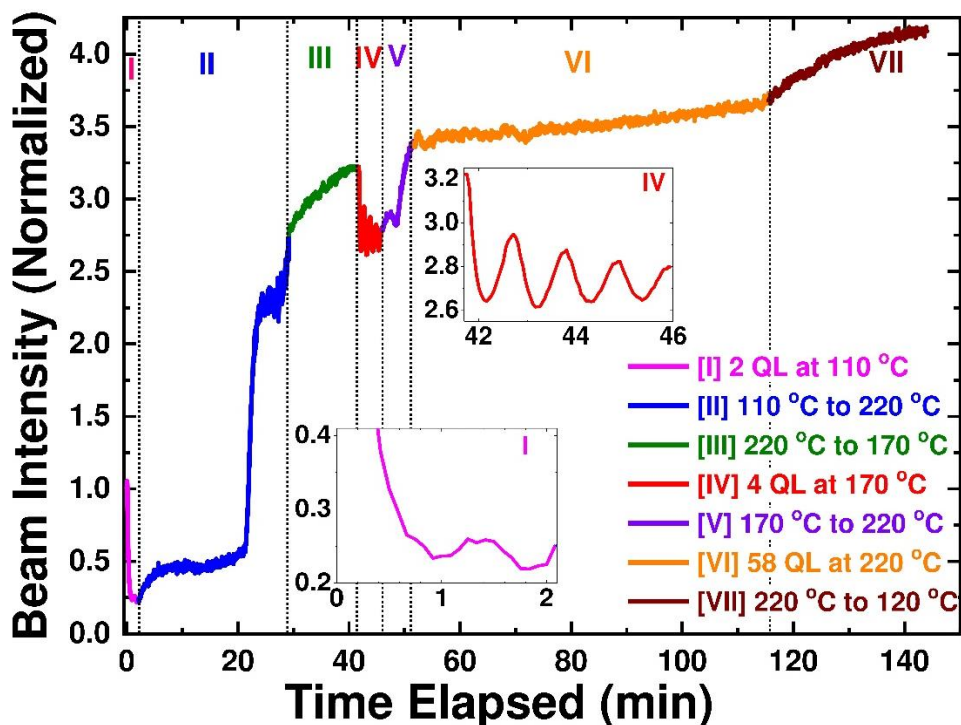


Fig. 5-2. Evolution of the specular beam intensity during Bi_2Se_3 growth at different temperature. After 2 QL deposition is done at 110 °C, the film is slowly heated to 220 °C. The temperature is reduced to 170 °C and another 4 QL are deposited. In the inset, clear RHEED oscillations can be seen for 170 °C growth and even for 110 °C growth. Specular beam intensity again increases on annealing to 220 °C, where it slowly increases during the 58 QL deposition without RHEED oscillation, implying that the growth occurs through step-flow mode at this temperature. Further increase in the specular beam intensity is observed on cooling the sample in Se atmosphere, indicating the Debye – Waller effect.

Fig. 5-2 shows the change in the spectral beam intensity during different growth steps as a 64 QL film is deposited on Si at different temperatures, starting from the Se-terminated surface. It was found that at low and intermediate temperatures, the growth occurs in layer-by-layer mode, evident by the observed RHEED intensity oscillations of the diffraction beam. One period of oscillation corresponds to a deposition of 1 QL of Bi_2Se_3 . It is seen in Fig. 5-2 insets that the relative starting position for the beam intensity variation during 170 °C growth is the same as the end position during 110 °C growth, indicating that the growth indeed

occurs QL-by-QL. From the RHEED oscillation period, the growth rate of Bi_2Se_3 QL was found to be $\sim 1 \text{ QL min}^{-1}$, which was confirmed by TEM. On increasing the growth temperature to 220°C , RHEED oscillation is no longer observed, indicating that the growth occurs in a step-flow mode, which is a better growth mode than the layer-by-layer type. Following the low/intermediate temperature growth, the crystallinity of the film is further enhanced on annealing the sample, as indicated by brightening of the specular beam spot as sample temperature is increased to 220°C . The sudden jump in the intensity during annealing the film from 110°C to 220°C occurs around 180°C showing that higher temperatures assist in crystallization of the film. Besides substrate temperature, Bi:Se flux ratio is also a key parameter in order to obtain good growth. As reported earlier by Xue et al., it was noticed that the growth was self-limited (⁶¹Zhang *et al.*, 2010; ⁷⁴Li *et al.*, 2010); i.e., growth rate was determined completely by Bi flux with excess Se species around. The Bi:Se flux ratio, measured by QCM, was kept $\sim 1:15$, with the Bi flux varied over a range from $0.87 \times 10^{13} \text{ cm}^{-2} \text{ s}^{-1}$ to $2.3 \times 10^{13} \text{ cm}^{-2} \text{ s}^{-1}$. The Se source was kept open at all times during the entire growth and annealing process. Within the growth temperature range, Se atoms have a non-zero coefficient only in the presence of other atoms (Bi, in this case) (⁷³Bringans *et al.*, 1989), so having the Se shutter open didn't cause any excess Se layers to be deposited on the films. Abundance of Se also minimizes the formation of Se vacancy, evident by the low carrier concentration in our films, and annealing the film in Se atmosphere further helps in crystallization of the film as observed by the brightening of the specular beam spot.

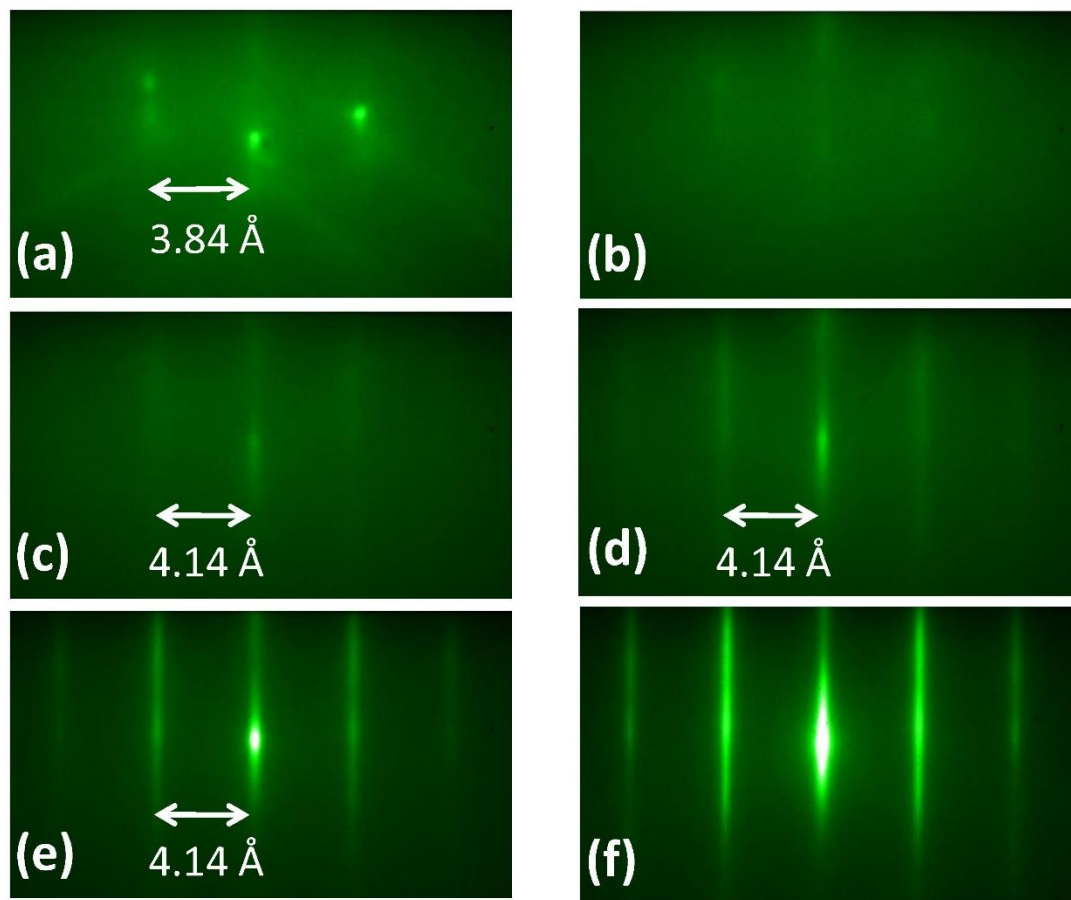


Fig. 5-3. Evolution of RHEED pattern on the surface from Si(111) 1×1 structure obtained by Se exposure at low temperature to the Bi_2Se_3 layers. (a) Surface after a monolayer of Se makes bonding with Si and removes the 7×7 reconstruction. (b) Structure midway the first QL deposition after ~ 0.5 QL of Bi_2Se_3 . (c) After deposition of 1 QL of Bi_2Se_3 . Streaky pattern indicative of single-crystalline structure can be seen. (d) The diffraction pattern improves on deposition of another QL. (e) RHEED pattern gets much brighter and sharper after annealing the 2 QL Bi_2Se_3 film to 220°C . (f) Final RHEED pattern of a 16 QL film grown by the two-temperature growth process.

Fig. 5-3(a–c) shows the evolution of the RHEED patterns from Se-terminated 1×1 Si surface to deposition of 1 QL of Bi_2Se_3 at 110°C . Except for the weak streaky pattern, any second phase or poly crystalline-ring is not observed, suggesting the onset of epitaxy right away with a single-crystal Bi_2Se_3 structure. Although the film is only 1 QL thick, the spacing of the Bi_2Se_3 streaks is less than that of Si, as shown in Fig. 5-3c. For several similar growths, the in-plane lattice constant of the 1 QL film

was found to be 4.14 ± 0.05 Å, compared with 3.84 Å of Si(111) plane, which is identical to the bulk lattice constant of Bi_2Se_3 . This relaxation of the Bi_2Se_3 lattice constant to its bulk value during the deposition of the first quintuple layer implies the absence of strain at the interface between the substrate and the film. The diffraction pattern becomes increasingly sharper on deposition of another QL, shown in Fig. 5-3d. Again from RHEED, it is evident that the film quality increases as the sample temperature is increased to a higher temperature, ~ 220 °C, as can be seen in Fig. 5-3e. The substrate temperature is ramped up slowly (~ 5 °C min^{-1}) to the higher growth temperature. It is critical to ramp the substrate temperature slowly as decomposition of the thin film has been observed on ramping the temperature too fast. Fig. 5-3f shows the sharp twin-free RHEED pattern of a 16 QL Bi_2Se_3 film grown by this two- temperature growth process. Thus, we developed a recipe with low temperature, 100 °C – 130 °C, initial 2-3 QL growth followed by a high temperature, 190 °C – 220 °C, growth, to obtain highly crystalline, second-phase-free and atomically sharp interface between Bi_2Se_3 and Si substrate, as verified by RHEED, XRD and TEM.

5.1.3 Film Structural Analysis

To study the interface between the grown Bi_2Se_3 film and Si surface and to confirm that the growth was epitaxial right from the first quintuple layer as seen in RHEED, we conducted TEM measurements on two films grown by our two-temperature growth process. One of the samples (12 QL thick) was in atmospheric conditions for a month before TEM measurement was carried out. At the interface, an amorphous

silicon dioxide layer, ~ 4 nm thick, was observed, but this layer was formed due to diffusion of oxygen through the grown film while the sample was kept in ambient condition. EDX and EELS analysis showed that the amorphous layer is composed of only silicon and oxygen, confirming that it is not amorphous Bi_2Se_3 , as observed by others (⁵⁹Li *et al.*, 2010). To further verify that it is not due to the growth process, we conducted TEM measurement on another sample (32 QL), which had a thick 300 nm Se capping layer to prevent oxygen diffusion from air. As shown in Fig. 5-4a(i), the cross-sectional TEM study reveals a full epitaxial structure of Bi_2Se_3 film down to the first quintuple layer without any amorphous layer. Both images clearly show the individual Bi_2Se_3 QLs with single crystalline structures. The difference in contrast of the two images is due to crystallographic orientations. Fig. 5-4a(ii) was oriented more to emphasize the QL spacing, while Fig. 5-4a(i) was oriented more to emphasize the Si- Bi_2Se_3 interface. The TEM also confirms the self-limited process of the low temperature Se deposition step on Si surface. This observation is consistent with the literature that selenide formation on Si occurs only at significantly higher temperatures (⁷³Bringans *et al.*, 1989). By growing the initial layer at the low temperatures followed by higher temperature annealing and further growth, we were able to avoid both SiSe_2 and amorphous Bi_2Se_3 formation, getting an atomically sharp interface. The sharp 1×1 RHEED pattern is consistent with the STM observation of atomically flat film with long terraces.

From the STM image of the surface of a 100 QL-thick Bi_2Se_3 , Fig. 5-4b, it is seen that triangular terraces are formed, reflecting the three-fold symmetry of

the bulk Bi_2Se_3 along hexagonal $[001]$ direction and each terrace step is ~ 1 nm, i.e. 1 QL along the c-axis, indicating that the growth occurs 1 QL-by-1 QL.

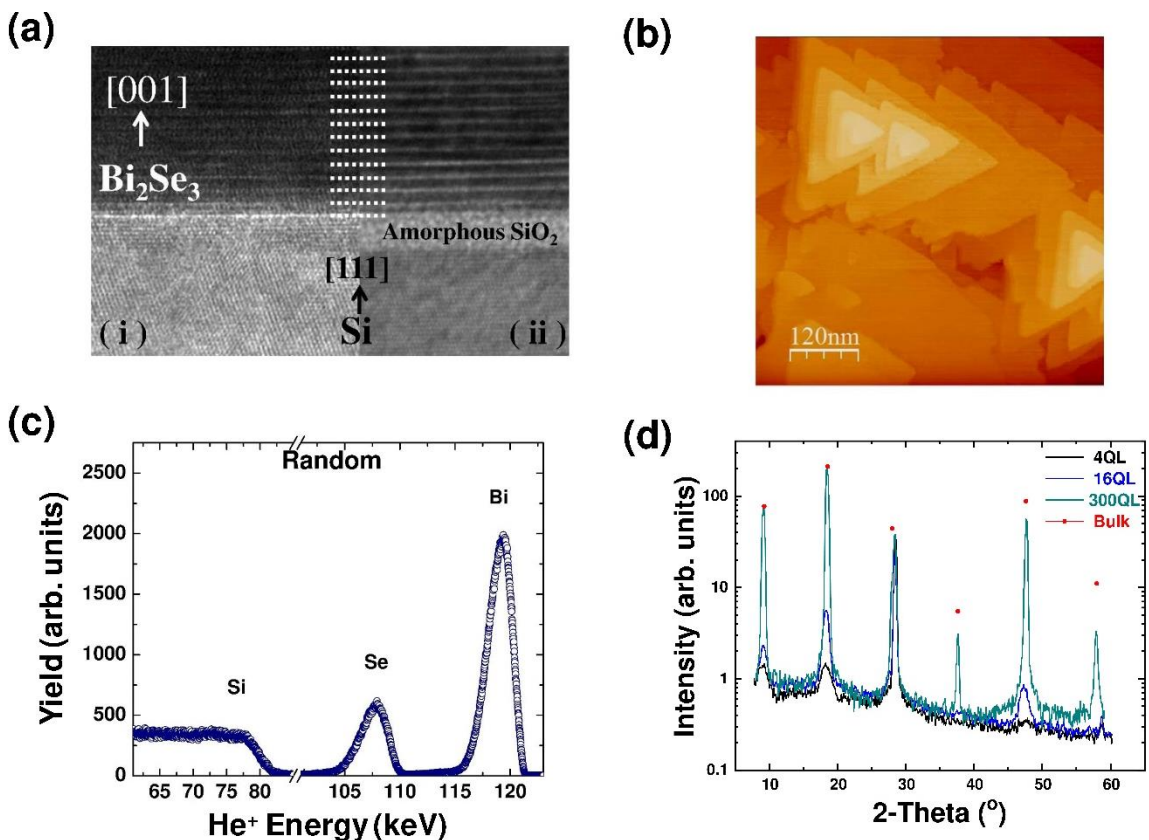


Fig. 5-4. (a) (i) TEM cross-section showing the sharp interface between the Bi_2Se_3 film and the Si(111) substrate for the sample with a 300 nm thick Se-capping. (ii) TEM cross-section of a Bi_2Se_3 sample without a capping layer, which was kept in ambient condition for weeks before the TEM measurement was done. Due to oxygen diffusion through the grown film, an amorphous layer of SiO_2 is formed at the interface, as verified by EDX and EELS. Due to the difference in sample orientations, contrast is clearer for silicon ordering and interface in (i) and Bi_2Se_3 QLs in (ii). The spacing between two consecutive dotted lines represents 1 QL, which is about 1 nm thick. The samples are prepared with the standard Ga-ion focused ion beam process. (b) STM image of a 100 QL sample grown on Si(111) substrate. The triangular terraces are indicative of the tri-fold symmetry of the Bi_2Se_3 (111) plane. (c) MEIS data for a 5 QL thick Bi_2Se_3 film. From MEIS, we see that our films are stoichiometric with the composition of Bi:Se=2.0:3.0. (d) XRD measurements for Bi_2Se_3 thin films of different thicknesses; the peak position provides quintuple layer spacing of ~ 9.6 Å along the c-axis.

The chemical stoichiometry was confirmed by MEIS for the grown Bi_2Se_3 films as thin as 3 QL. Fig. 5-4c shows MEIS data for a thin 5QL Bi_2Se_3 film; the films were found to be stoichiometric with $\text{Bi}:\text{Se} = 2.0:3.0$. XRD provides the quintuple layer spacing of $\sim 9.6 \text{ \AA}$, consistent with that of bulk samples, as shown in Fig. 5-4d. By inspecting the details of the XRD peaks, we see that our thin films, as thin as 4 QL, are c-axis oriented along the growth direction and have the same structure as bulk samples.

5.2 Thickness – dependence of Bulk Transport Properties⁵

The transport measurements were carried out with the standard van der Pauw method with indium contacts on four square corners in a cryostat with magnetic field up to 9 T and a base temperature of 1.5 K; measurement errors due to the contact geometry are estimated to be less than 10%. The following measurements were all taken at a fixed temperature of 1.5 K with each sample exposed to air for less than 20 min to minimize air contamination; at this temperature, the undoped Si substrates were completely insulating and did not contribute to the transport measurements.

5.2.1 Basic Transport

For all films except for 3 QL, the R vs T curves in Fig. 5-5a showed metallic behavior at high temperature, but as the temperature dropped below 30 K, the resistance tended to increase slightly either due to strong electron-electron interaction in the

⁵ This section is based on work published in ⁹⁶Y.-S. Kim, N. Bansal *et al.*, Physical Review B **84**, 073109 (2011).

two-dimensional (2D) limit (⁶²Liu *et al.*, 2011) or due to an impurity band in the bulk (⁷⁵Analytis *et al.*, 2010)

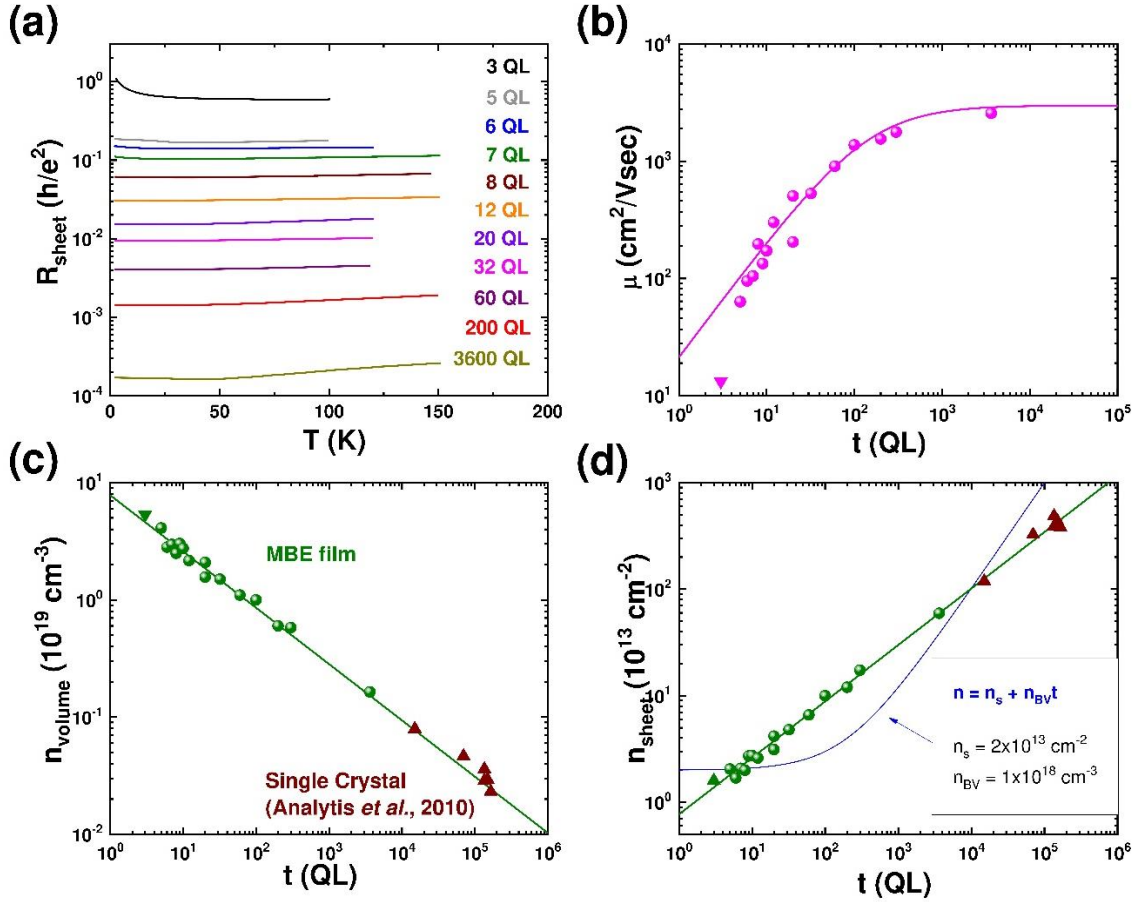


Fig. 5-5. Thickness dependence of the transport properties of Bi₂Se₃. **(a)** Resistance of Bi₂Se₃ films as a function of temperature with thickness ranging from 3 to 3,600 QL. Data above ~ 150 K are not shown here because they are affected by the parallel conduction of thermally excited carriers in the undoped silicon substrates. **(b)** Mobility. **(c)** and **(d)** Carrier density of electrons in Bi₂Se₃ films obtained by Hall measurement at 1.5 K. The solid curve in (b) is $\mu(t) = 3,000/(1 + 140/t)$, and the straight lines in (c) and (d) are illustrative guides.

It is well known that the mobility of conventional thin films depends on the film thickness as $\mu = \mu_{\infty}/(1 + 2(\lambda/t)(1 - p))$, where μ_{∞} is the mobility of the film when the thickness, t , is much larger than the mean free path, λ , with p representing the fraction of carriers reflecting specularly from the surface (⁷⁶Elshabini *et al.*, 1998);

this mobility drop originates from the reduction in the effective mean free path caused by diffuse scattering from the surfaces. Fig. 5-5b shows that the mobility vs thickness data, obtained from Hall effect measurements, are in good agreement with this standard theory with $\mu_{\infty} \approx 3,000 \text{ cm}^2/\text{Vsec}$ and $\lambda(1 - p) \approx 70 \text{ nm}$, except for the 3 QL data marked with a triangle. If the bulk of the film is insulating and the transport is entirely confined to the surfaces, the mobilities should be thickness independent except for very thin samples in which quantum tunneling between the top and bottom surfaces can degrade the surface states (⁶¹Zhang *et al.*, 2010; ⁷⁷Linder *et al.*, 2009; ⁷⁸Lu *et al.*, 2010). The very observation of the conventional thickness dependence implies that the observed mobilities are dominated by the bulk instead of the surface transport.

While the thickness dependence of the mobilities can be well understood by the standard surface scattering theory, the thickness dependence of the volume and sheet carrier densities plotted in Figs. 5-5c – 5-5d is puzzling and unexpected. The volume carrier density (defined as the total sheet carrier density, obtained from the Hall measurement, divided by the sample thickness) decreases monotonically as the thickness increases and scales as $t^{-0.5}$ over three orders of thickness range, from $5.3 \times 10^{19} \text{ cm}^{-3}$ for 3 QL to $1.6 \times 10^{18} \text{ cm}^{-3}$ for 3,600 QL. Little change occurred in these values even after the films were annealed in high selenium vapor pressures, up to six orders of magnitude higher than the normal growth conditions; this implies that the observed carrier densities are close to the absolute minimum values that are experimentally achievable in these pure Bi_2Se_3 films. We examined published data obtained from single crystal samples (⁷⁵Analytis *et al.*, 2010), and surprisingly these

data points fell on the same curve, extending the trend up to five orders of thickness (3 nm – 170 μm) with $2 \times 10^{17} \text{ cm}^{-3}$ for 170- μm -thick single crystal (⁷⁵Analytis *et al.*, 2010). Considering that two completely different sample formation processes, one through MBE growth and the other through peeling of bulk samples (⁷⁵Analytis *et al.*, 2010), result in the same thickness dependence suggests some fundamental mechanism behind this anomalous thickness dependence of the carrier densities. Another view of this anomaly is through the thickness dependence of the sheet carrier density. If we assume constant bulk volume carrier density (n_{BV}) and constant surface carrier density (n_s), the total sheet carrier density (n_{sheet}) should scale linearly with the sample thickness (t) such that $n_{\text{sheet}} = n_s + n_{BV}t$. In Fig. 5-5d, the theoretical curve with $n_s = 2 \times 10^{13} \text{ cm}^{-2}$ and $n_{BV} = 1 \times 10^{18} \text{ cm}^{-3}$ was plotted for comparison with the experimental data. The observed data can in no way be explained by this simple model, and instead the total sheet carrier density scales as $t^{0.5}$. This implies that the bulk volume carrier density is not constant but varies monotonically with its thickness over five orders of magnitude. Considering that either the TI surface state (⁷⁷Linder *et al.*, 2009) or the surface band-bending effect (⁷⁹Bianchi *et al.*, 2010) can never extend more than tens of nanometers, while the observed anomaly extends far beyond the micrometer scale, associating this observation with such an electronic mechanism seems unphysical. Because the volume carrier density mainly originates from the selenium vacancies (⁸⁰Hor *et al.*, 2009), this observation nominally implies that the volume density of selenium vacancies gradually increases as samples get thinner. The formation of selenium vacancies through diffusion seems to continuously occur even at room temperature, as confirmed by other group with x-

ray photoelectron spectroscopy (⁸¹Kong *et al.*, 2011). These observations suggest that formation of selenium vacancies in Bi₂Se₃ is thermodynamically favorable at room temperature, yet it occurs through a slow diffusion process, which is inevitably thickness dependent. This also implies that the measured carrier density of a sample depends on the time between sample fabrication and measurement, and so in order to maintain consistency, almost all samples reported here were measured on the day they were fabricated. In other words, the exact thickness dependence of the carrier densities, especially in the thin limit, may depend on when they are measured.

5.2.2 Weak Anti - Localization

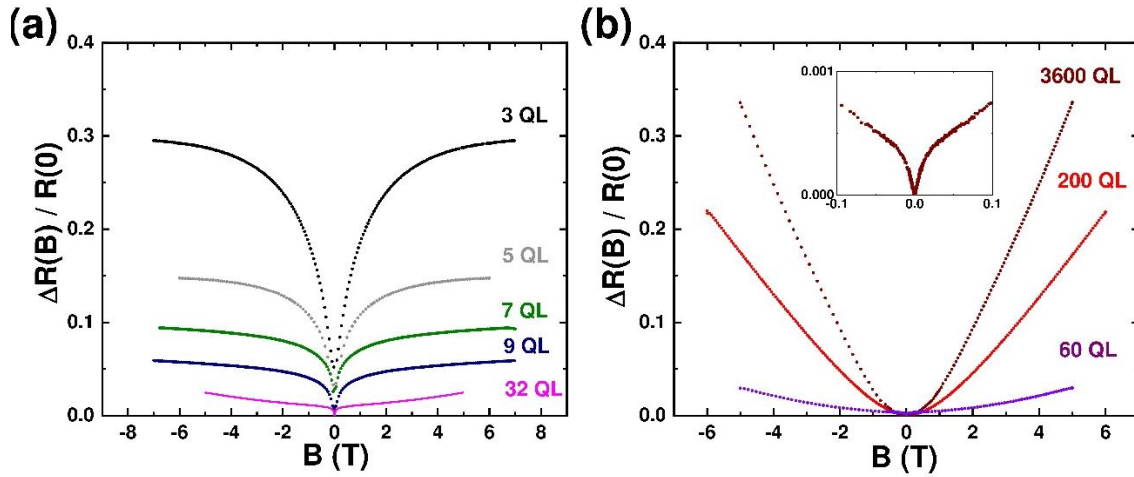


Fig. 5-6. Normalized magnetoresistance. The magnetic field dependence of resistance at 1.5 K of **(a)** thin film from 3 to 32 QL, and **(b)** thick film from 60 to 3,600 QL. Deep cusp in low-field regime is characteristic of the WAL effect. Parabolic field dependence is dominant in thick films. Inset of (b): zoomed-in view of the 3,600 QL data near zero field showing robustness of the WAL effect.

The magnetoresistance (MR) measurements provide another means to probe the TI properties. In Figs. 5-6a – 5-6b, the MR, defined as $(R(B) - R(0))/R(0)$, in the high-field regime is dominated by the parabolalike (B^2) dependence, originating from

the Lorentzian deflection of carriers under perpendicular magnetic field (⁸²Ziman, 1960) (recall that the electron executes cyclotron orbits, thereby shortening the mean free path, and thus increasing the resistance). The fact that this B^2 dependence is more pronounced in thicker samples suggests that it is a bulk-dominated effect.

In the low-field regime (< 0.5 T) for thinner samples, the magnetoconductance (MC), as shown in Fig. 5-7a, decreases sharply as the magnetic field is increased, which is typical of the weak antilocalization (WAL) effect (⁶⁴Chen *et al.*, 2010; ⁸³Checkelsky *et al.*, 2011). This WAL effect is the result of the strong spin-orbit coupling, which puts backscattering at the minimum when there is no magnetic field due to the time-reversal symmetry. As magnetic field increases, thus breaking the time-reversal symmetry, backscattering increases and leads to a sharp reduction in conductance. The low-field MC, $\Delta G(B) = G(B) - G(0)$, can be well fitted to the standard Hikami-Larkin-Nagaoka (HLN) theory for WAL (⁸⁴Hikami, 1980):

$$\Delta G(B) = A(e^2/h) [\ln(B_\phi/B) - \Psi(1/2 + B_\phi/B)]$$

where A is a coefficient predicted to be $1/2\pi$ for each 2D channel, B_ϕ is the dephasing magnetic field, and $\Psi(x)$ is the digamma function. The dephasing magnetic field is related to the phase coherence length l_ϕ via (⁶²Liu *et al.*, 2011) $B_\phi = \hbar/(4el_\phi^2)$. Figs. 5-7b – 5-7c show the fitting parameters as a function of thickness for 3–100 QL. Except for 3 QL, the fitting parameter A remains approximately constant around $1/(2\pi)$, while the parameter l_ϕ monotonically increases as samples get thicker. The parameter A being closer to $1/(2\pi)$ than $1/\pi$ nominally implies that the WAL effect over 5–100 QL is dominated by a single 2D channel (⁸⁵Chen *et al.*, 2011; ⁸⁶Steinberg *et al.*, 2011).

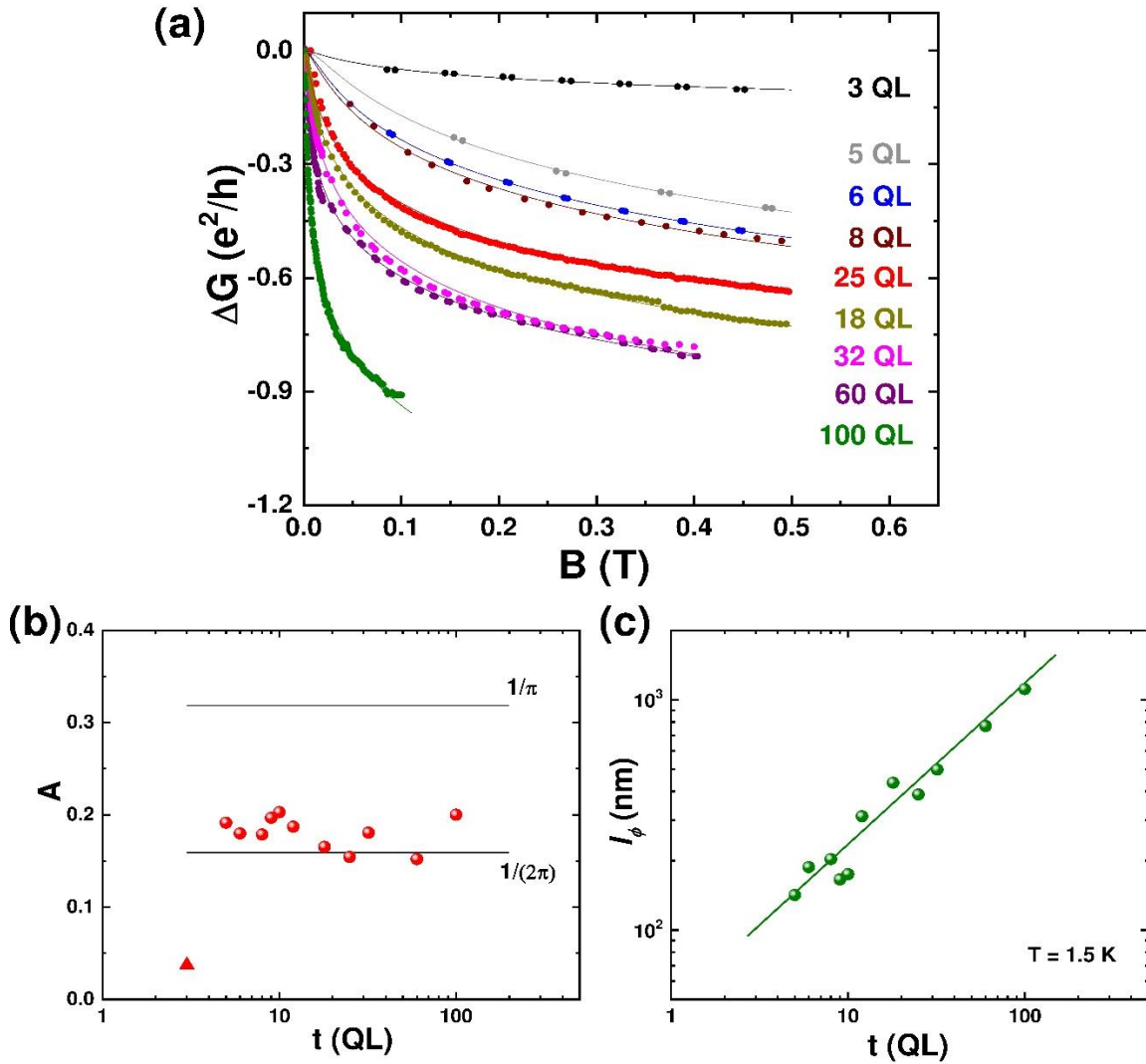


Fig. 5-7. Weak antilocalization effect. **(a)** The HLN fitting of the change in conductance in low-field regime from 3 to 100 QL. **(b)** Above 5 QL, the coefficient A is almost thickness independent, close to a single channel WAL contribution, that is $1/(2\pi)$. **(c)** The phase coherence length increases as $t^{0.7}$ with the sample thickness.

There are two possibilities for this observation. The first is that the WAL effect originates entirely from the reduced dimensionality of the metallic bulk state without any contribution from the surface states. The other is that the surface states contribute, but they couple strongly with the metallic bulk state and behave together as a single 2D system. We will show below that the thickness-dependence analysis of

l_ϕ supports the latter. The WAL signal became too small to be of quantitative relevance as the thickness increased beyond 100 QL, but the spike in ΔG was still visible up to 3,600 QL as shown in the inset of Fig. 5-6b, suggesting the robustness of the WAL effect.

Fig. 5-7c shows that the phase coherence length l_ϕ scales as $t^{0.7}$. If the WAL effect originated entirely from the geometrically confined bulk state of the film without any surface state contribution, then l_ϕ should scale linearly with thickness in the thin film limit, just as the bulk-dominated mobility – a quantity proportional to a mean free path – presented in Fig. 5-5b scales almost linearly with the thickness over 5–100 QL. Therefore, the sublinear thickness dependence of l_ϕ suggests that there should be a considerable surface state contribution to the WAL signal and that the observed single channel effect must be due to strong coupling between the surface and bulk states. Now if the bulk of the film were insulating, then l_ϕ , being a surface property, had to be independent of the thickness – the surfaces should not change when the thickness changes. However, with conducting bulk states, the surfaces and bulk can interact with one another and lead to a thickness-dependent scattering mechanism. In other words, the thickness-dependent coherence length is a natural result of the metallic bulk states. According to this analysis, the thickness dependence of l_ϕ , denoted by α in $l_\phi \sim t^\alpha$, could be used as a figure of merit to tell how close certain TI materials are to an ideal TI; α should be zero for an ideal TI with the insulating bulk state, one for a topologically trivial strongly spin-orbit-coupled metal, and between zero and one for a non-ideal TI with the metallic bulk state, approaching zero as the material gets closer to an ideal TI.

5.3 Conclusions

To summarize, we found that the key parameters for obtaining single crystalline Bi_2Se_3 film on silicon substrates without any interfacial layers are the substrate preparation prior to growth and the two-temperature growth process. Contrary to the common belief found in literature that either Bi, amorphous Bi_2Se_3 or some other buffer layer is required to grow single-crystalline Bi_2Se_3 heteroepitaxially on Si, we have shown that these films can be grown with an atomically abrupt interface on Si without any interfacial layers using our two-temperature growth process. The high quality of MBE-grown Bi_2Se_3 films with precise layer thickness control and interfacial abruptness on Si(111) substrate will make it a strong candidate for further study of topological insulators.

Furthermore, extensive thickness-dependent studies of the Bi_2Se_3 transport properties have led to a number of unexpected findings. The volume carrier density, which is commonly assumed to be thickness independent, decreased by more than two orders of magnitude over five orders of thickness, suggesting that selenium diffusion is highly thickness dependent and active even at room temperature. The mobility increased linearly with thickness in the thin film regime and saturated as the samples got thicker, suggesting that the surface scattering effect limits the mean free path in the thin limit. The WAL effect was dominated by a single 2D channel over two decades of thickness. The sublinear thickness dependence of the phase coherence length supports the presence of the surface states and provides a figure of merit, characterizing the level of interaction between the surface and bulk states. Our

observations suggest that interactions between the bulk and surface states have profound effects on their transport properties.

Chapter 6. THICKNESS – INDEPENDENT TRANSPORT CHANNELS IN Bi_2Se_3 THIN FILMS⁶

Owing to the strong coupling between the surface and bulk transport channels, to the extent that the two cannot be distinguished, in the Bi_2Se_3 films grown on Si, it is imperative that the quality of the Bi_2Se_3 films be improved to minimize the bulk conduction. Despite Al_2O_3 having a much larger lattice constant ($\sim 4.785 \text{ \AA}$), and a larger lattice mismatch ($\sim 14\%$) with Bi_2Se_3 as compared to Si, it is expected that higher quality Bi_2Se_3 will be grown due to chemical inertness of Al_2O_3 and relaxation of Bi_2Se_3 lattice constant to its bulk value within first QL deposition. In this chapter, we will focus on the growth and measurements on Bi_2Se_3 films grown on Al_2O_3 with varying thickness, and discuss the behavior of different transport channels. The Bi_2Se_3 films used for this study were grown on c-axis Al_2O_3 substrates ($10 \times 10 \times 0.5 \text{ mm}^3$) with molecular beam epitaxy (MBE); the films were grown using the two-step scheme, as discussed in the section 5.1.2.

⁶ This chapter is based on work published in ⁹⁶N. Bansal *et al.*, Physical Review Letters **109**, 116804 (2012).

6.1 Bi₂Se₃ Film Growth on Al₂O₃

To start with a clean Al₂O₃ (0001) (sapphire) substrate surface, we exposed the substrate to an ex situ UV ozone cleaning step before mounting it in the growth chamber to burn off majority of the organic compounds that may be present on the surface. To further remove any possible contaminants from the substrate surface, the sapphire substrate was heated to 700 °C in oxygen pressure of 10⁻⁶ Torr for 10 min (⁸⁷Gota *et al.*, 1999). The substrate surface was observed with RHEED before and after the treatment, and a bright specular spot and Kikuchi lines were observed after heating and then cooling the substrate. Figs. 6-1a,b indicate that this procedure helped improving the surface conditions.

Evolution of the film surface during growth was monitored by RHEED, shown in Fig. 6-1(c-f). One might assume that due to chemical inertness of Al₂O₃ surface, Bi₂Se₃ may be directly deposited as a single step at higher temperature, but due to minimal sticking coefficient for Se/Bi at higher temperatures, the single step growth leads to disordered growth at the interface. Once initial layer is uniformly deposited at lower temperatures (Fig. 6-1c), annealing to the higher temperature in Se ambient improves crystal quality (Fig. 6-1d). After deposition of 3 QL of Bi₂Se₃ at 110 °C, a sharp streaky pattern was observed, indicating single-crystal Bi₂Se₃ structure. The film was then slowly annealed to a temperature of 220 °C, which helped further crystallization of the film as seen by the brightening of the specular spot. The diffraction pattern and the Kikuchi lines became increasingly sharp on further Bi₂Se₃

deposition (Fig. 6-1f). This shows that the grown films have atomically flat morphology and high crystallinity.

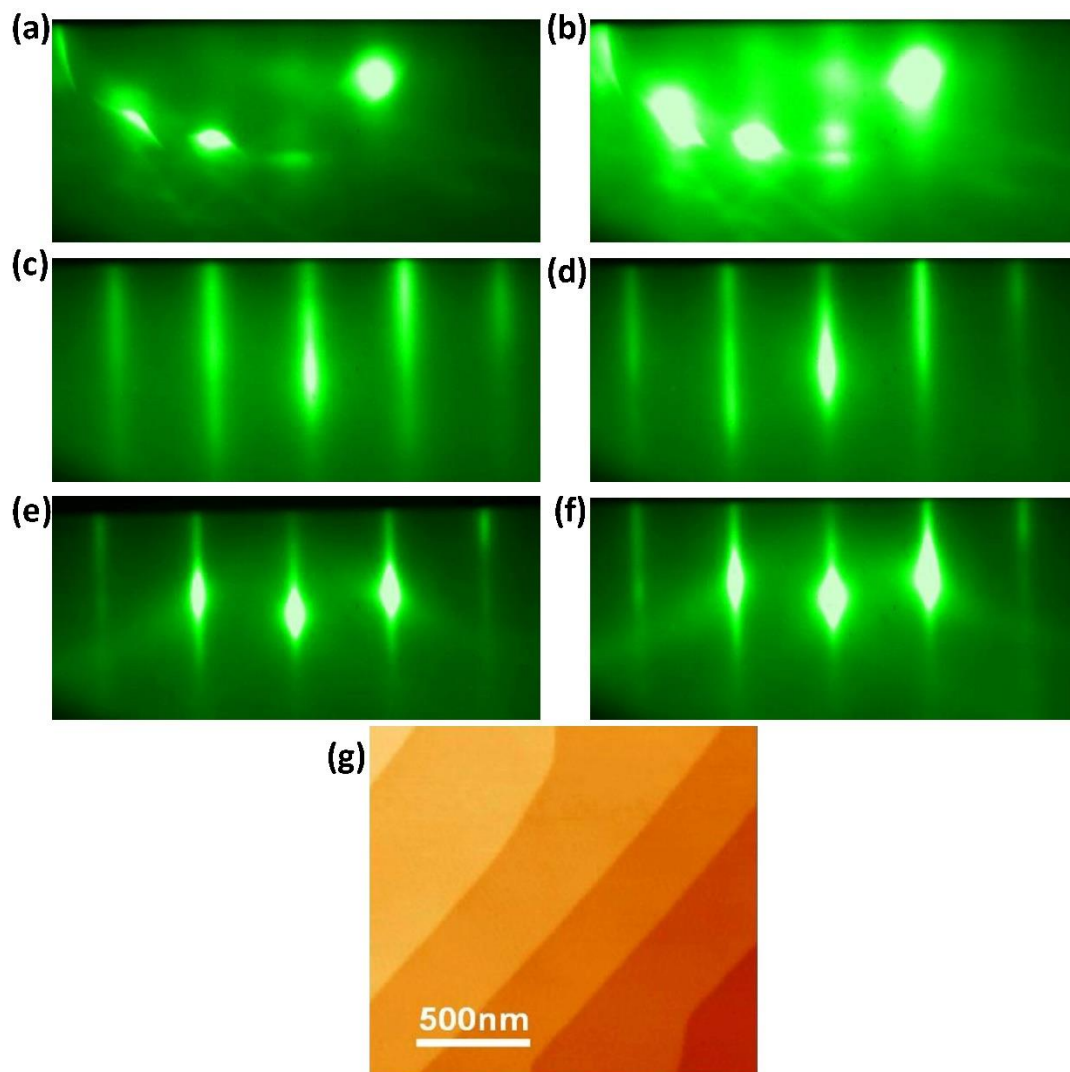


Fig. 6-1. RHEED images showing the steps of Bi_2Se_3 growth on sapphire substrates. **(a)** Sapphire substrate mounted in the UHV growth chamber after UV-cleaned for 5 min. **(b)** On heating to 700 °C in an O_2 pressure of 1×10^{-6} Torr for 10 min. **(c)** After deposition of 3 QL of Bi_2Se_3 film at 110 °C. **(d)** Specular beam spot gets brighter on annealing the film to 220 °C. **(e)** RHEED pattern gets much brighter and sharper on subsequent growth of another 29 QL at 220 °C. **(f)** Final RHEED pattern of the 32 QL film after being annealed at 220 °C for an hour. **(g)** $1.5 \times 1.5 \mu\text{m}^2$ scanned atomic force microscopy image of a 300 QL thick Bi_2Se_3 film grown on $\text{Al}_2\text{O}_3(0001)$. Large terraces (largest ever reported for Bi_2Se_3 thin films) are observed, further verifying the high quality of the grown films.

The film quality was further improved by annealing the sample in Se-environment at 220 °C for an hour after the growth. This process led to high quality single crystalline films with large terraces as seen in AFM image (Fig. 6-1g). On both Si and Al₂O₃ substrates, deposited Bi₂Se₃ has the lowest surface energy when epitaxial growth deposits in triangular shapes. However, due to high reactivity of the Si-surface, there are more nucleation centers and thus rougher growth, as compared to that on Al₂O₃. On Al₂O₃, the nucleation probably starts from the edges and extends from there, resulting in atomically flat terraces (Fig. 6-1g) much larger than any previous reports on Bi₂Se₃ thin films (⁴⁸Cheng *et al.*, 2010; ⁶³Richardella *et al.*, 2010; ⁸⁸Li *et al.*, 2010; ⁸⁹Bansal *et al.*, 2011), representing the high quality of these samples.

6.2 Two - Channel Transport

Fig. 6-2a shows that the resistance vs temperature (from 290 to 1.5 K) dependence is metallic down to ~30 K for all thicknesses 2 – 256 QL. Below ~30 K, the resistance remained almost constant, indicating static disorders as the dominant scattering mechanism, except for ultrathin films, which show slight resistance increase as temperature decreases. The first notable feature in Fig. 6-2a is that the low temperature resistance is quite thickness independent for samples between ~8 and 256 QL in thickness. This can be seen more clearly in the plot of conductance (G_{xx}) at 1.5 K versus sample thickness in Fig. 6-2b. Within small error bars, G_{xx} is nominally constant for samples between ~8 and 256 QL thick. This observation suggests that the conductance in this thickness range is dominated by some surface transport channels.

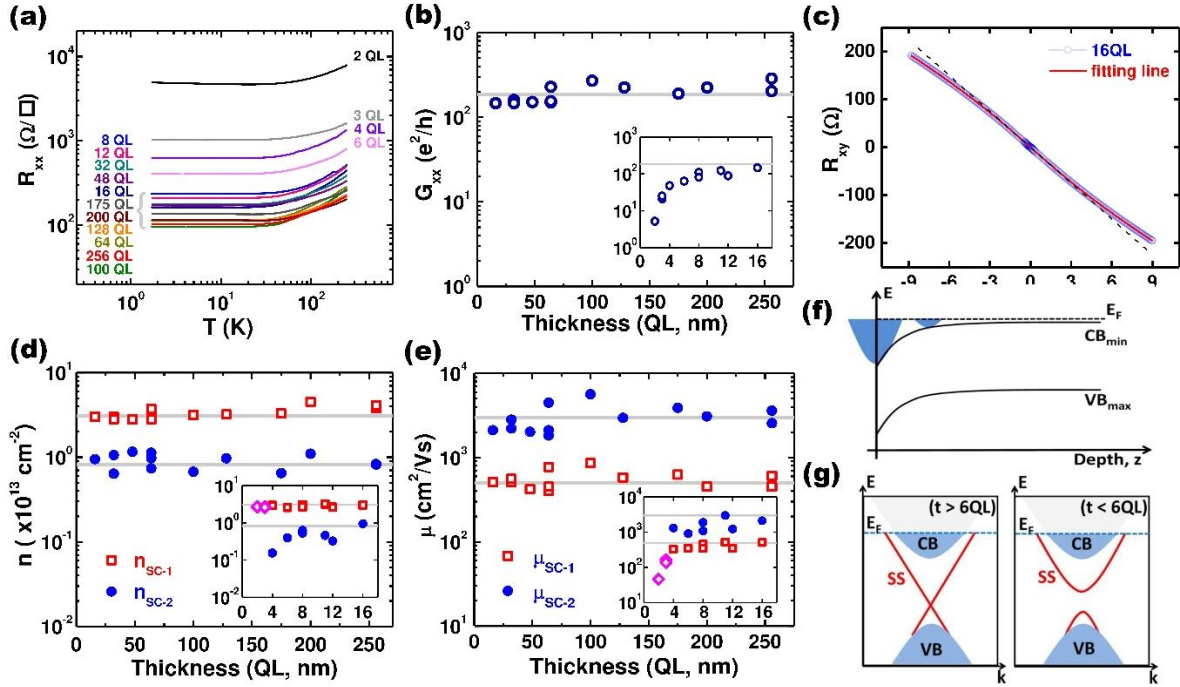


Fig. 6-2. Transport properties of Bi₂Se₃ films. **(a)** Resistance vs temperature for each thickness. **(b)** Conductance at 1.5 K as a function of thickness. **(c)** Hall resistance vs magnetic field for a 16 QL sample plotted together with the two-carrier model fitting curve described in section 6.2.1. **(d)** and **(e)** Sheet carrier densities and mobilities vs thickness. For 2 and 3 QL films (shown by a diamond in the inset), the sheet carrier density was directly read off from the linear R_{xy} vs B curve. In (b), (d), and (e), the horizontal straight lines are guides for illustration, and data for films thinner than 16 QL are plotted in the insets. **(f)** Conduction band minimum (CB_{min}) and valence band maximum (VB_{max}) along the depth of the sample, showing the downward band bending toward the surface. **(g)** Schematic surface band diagrams, depicting how the surface bands change through the critical thickness (6 QL) when the surface Fermi level is high: CB and SS stand for the bulk conduction band and the topological surface state, respectively.

The Hall effect measurement shown in Fig. 6-2c provides more insights regarding the origin of these surface channels. If all carriers had the same mobility, $R_{xy}(B)$ should appear as a straight line with the slope determined by $1/(n_{sc}e)$, with n_{sc} representing the total sheet carrier density. However, if there are multiple types

of carriers with different but comparable mobilities, nonlinearity shows up in the $R_{xy}(B)$ data; if some carriers have much lower carrier densities or mobilities than others, they do not contribute to the nonlinearity of $R_{xy}(B)$ either. Therefore, the nonlinearity in Fig. 6-2c suggests the presence of multiple carrier types with comparable mobilities.

6.2.1 Two - Carrier Model

With non-interacting, relaxation time approximation, under perpendicular magnetic field, the elements of the conductance tensor as a function of the two mobilities (μ_1, μ_2) and the corresponding sheet carrier densities (n_1, n_2) are given as:

$$G_{xx} = e \left(\frac{n_1 \mu_1}{1 + \mu_1^2 B^2} + \frac{n_2 \mu_2}{1 + \mu_2^2 B^2} \right); G_{xy} = eB \left(\frac{n_1 \mu_1^2}{1 + \mu_1^2 B^2} + \frac{n_2 \mu_2^2}{1 + \mu_2^2 B^2} \right)$$

Inverting this conductance tensor, we find the Hall resistance to be:

$$R_{xy}(B) = -\frac{G_{xy}}{G_{xx}^2 + G_{xy}^2} = -\frac{B}{e} \left(\frac{(n_1 \mu_1^2 + n_2 \mu_2^2) + B^2 \mu_1^2 \mu_2^2 (n_1 + n_2)}{(n_1 \mu_1 + n_2 \mu_2)^2 + B^2 \mu_1^2 \mu_2^2 (n_1 + n_2)^2} \right)$$

where B is the magnetic field.

It turns out that this two-carrier model nicely fits all our Hall resistance data as shown in Fig. 6-2c. This implies that the mobilities of all the significant conductance channels in our samples can be approximately grouped into two; in this model, carriers on opposite surfaces or on different bands will appear as part of the same channel if they have similar mobilities.

Although this formula can be used to fit the measured Hall resistance data, as shown in Fig. 6-2c, in order to maximize the fitting reliability, we used the Hall conductance, $G_{xy}(B) \equiv -R_{xy}/(R_{xx}^2 + R_{xy}^2)$, instead of $R_{xy}(B)$ for the fitting and also

reduced the number of fitting parameters to two by applying extra confinement from $G_{xx}(B)$. If we take the limiting ($B \rightarrow 0$) case of the $G_{xx}(B)$ and $G_{xy}(B)$ expressions, they reduce to:

$$\frac{G_{xx}(0)}{e} = n_1\mu_1 + n_2\mu_2 = C_1; \quad \lim_{B \rightarrow 0} \frac{G_{xy}(B)}{eB} = n_1\mu_1^2 + n_2\mu_2^2 = C_2$$

where e is the electronic charge, and C_1 and C_2 are constants that can be found directly from the measured data. $C_1 = \frac{G_{xx}(0)}{e}$ can be directly read off from the measured conductance data at zero field, and $C_2 = \lim_{B \rightarrow 0} \frac{G_{xy}(B)}{eB}$ can be found from the linear slope of the Hall conductance near zero magnetic field. Solving the above two equations, we find:

$$n_1 = \frac{C_1\mu_2 - C_2}{\mu_1\mu_2 - \mu_1^2}; \quad n_2 = \frac{C_1\mu_1 - C_2}{\mu_1\mu_2 - \mu_2^2}$$

This way, we can eliminate the two parameters, n_1 and n_2 , from the Hall conductance equation such that:

$$G_{xy}(B) = eB \left(\frac{C_1\mu_1 - C_2}{(\mu_1/\mu_2 - 1)(1 + \mu_2^2 B^2)} + \frac{C_1\mu_2 - C_2}{(\mu_2/\mu_1 - 1)(1 + \mu_1^2 B^2)} \right)$$

Because this is now just two-parameter fitting, fitting can be much more reliably performed than the original four parameter fitting. This fitting provides two mobilities for each sample and their corresponding sheet carrier densities are then calculated from the mobilities.

Because it is the resistances not the conductances that are directly recorded from instruments, in order to obtain Hall conductance data from the measured

resistance values, matrix inversion has to be done. In other words, the elements of conductance tensors are found from measured R_{xx} and R_{xy} as:

$$G_{xy}(B) = -\frac{R_{xy}}{R_{xy}^2 + R_{xx}^2}; \quad G_{xx}(B) = \frac{R_{xx}}{R_{xy}^2 + R_{xx}^2}$$

From this two parameter fitting, we extracted the four quantities, n_1 , μ_1 , n_2 , and μ_2 for each sample. These G_{xy} data are in good agreement with the two-carrier model, as shown Fig. 6-3.

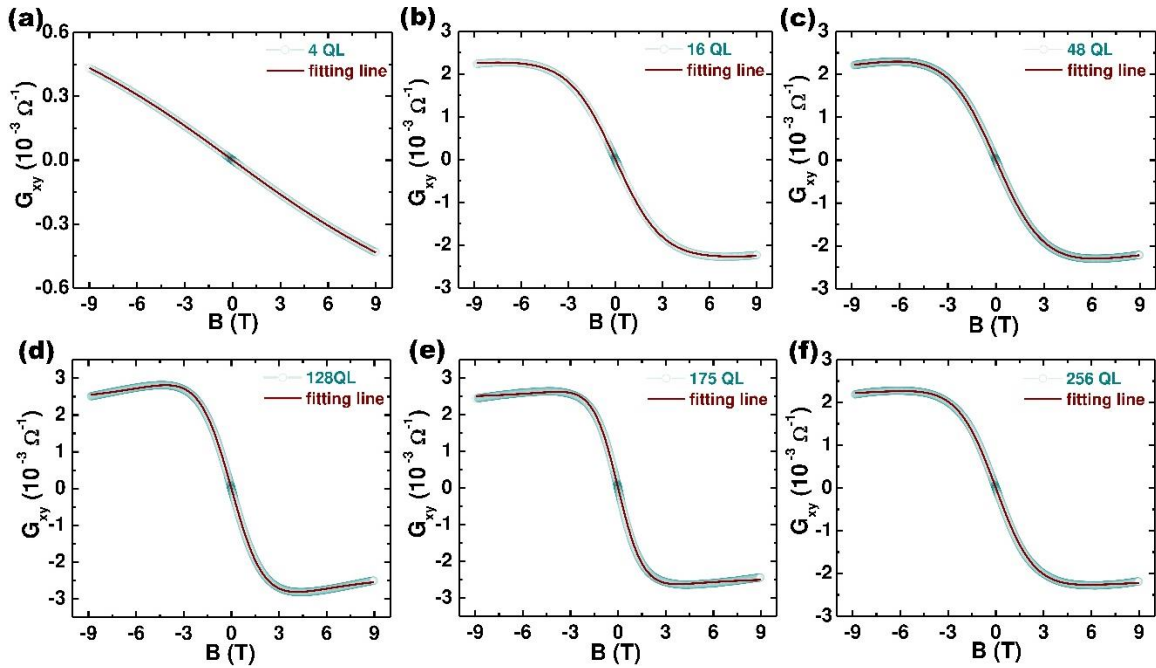


Fig. 6-3. Hall conductance data fitted with the standard two-carrier model. In these plots, $G_{xy}(B) \equiv \frac{R_{xy}}{R_{xx}^2 + R_{xy}^2}$ was used; note the absence of the ‘-’ sign.

6.2.2 Weak Anti-Localization

Fig. 6-4 presents another set of thickness-independent transport properties. In the normalized resistance vs magnetic field data in Fig. 6-4a, the cusp around the zero magnetic field is an indication of the weak antilocalization (WAL) effect. Although Fig. 6-4a gives the impression that the magneto- transport is highly thickness dependent,

the small magnetic field regime in Fig. 6-4b provides a surprisingly simple picture. On the surface of TI materials, backscattering is, at the minimum, due to time-reversal symmetry when the magnetic field is absent. With an increasing magnetic field, which breaks the time-reversal symmetry, backscattering increases and leads to a reduction in conductance as in Fig. 6-4b; this phenomenon is called the WAL effect (⁸⁵Chen *et al.*, 2011; ⁹⁰Kim *et al.*, 2011).

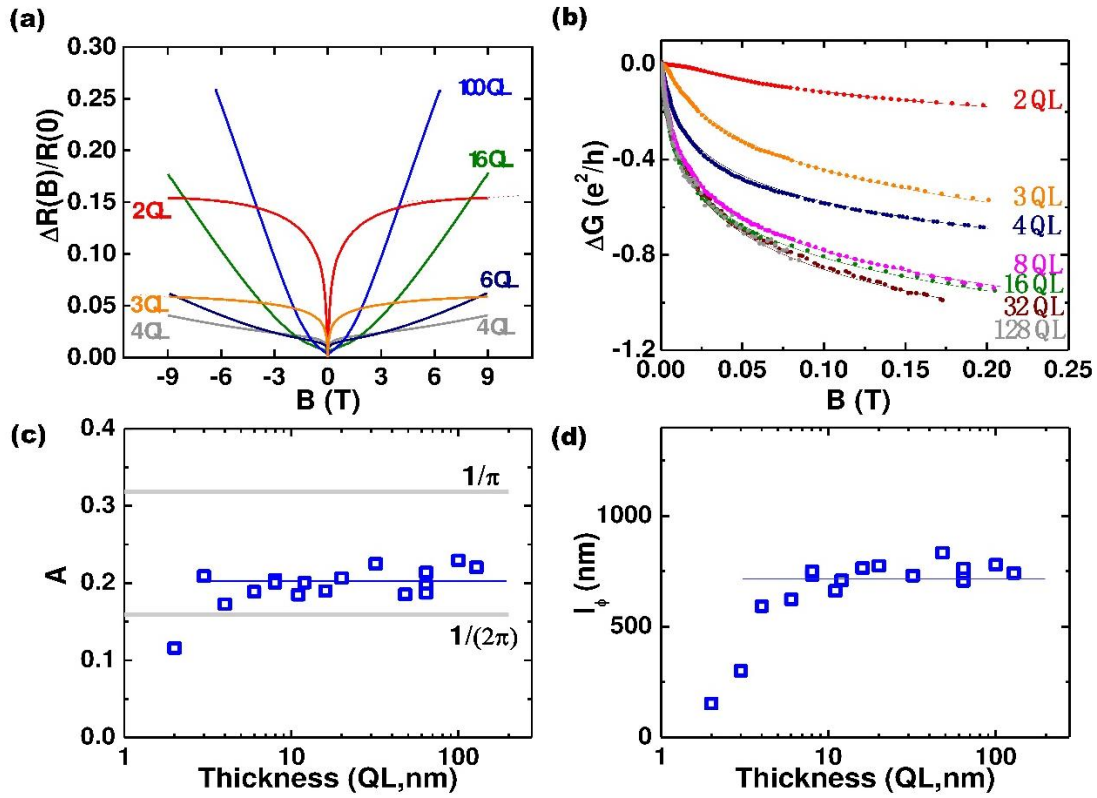


Fig. 6-4. (a) Normalized resistance change as a function of the magnetic field, measured at 1.5 K, where $\Delta R(B) \equiv R(B) - R(0)$. The deep cusp in low field regime is characteristic of the WAL effect. (b) Conductance change vs magnetic field in the low field regime: 8–128 QL curves are almost overlapping. The theoretical WAL fitting curves are plotted together for each data set. (c) and (d) The WAL fitting parameters, A and l_ϕ , vs the thickness, respectively. The horizontal lines are a guide for illustration.

Just like the other transport properties, this WAL effect also shows thickness independence for films thicker than ~ 8 QL. According to the standard WAL theory

(⁸⁴Hikami *et al.*, 1980), the 2D magnetoconductance, $G(B)$, is expected to change as $\Delta G(B) = A(e^2/h)[\ln(B_\phi/B) - \Psi(1/2 + B_\phi/B)]$, where A is a coefficient predicted to be $1/(2\pi)$ for each 2D channel, B_ϕ is the dephasing magnetic field, and $\Psi(x)$ is the digamma function. The dephasing magnetic field is related to the phase coherence length l_ϕ via $B_\phi = \hbar/(4el_\phi^2)$ (⁸⁵Chen *et al.*, 2011; ⁹⁰Kim *et al.*, 2011).

Fig. 6-4c shows that A remains almost constant from 3 through 128 QL, with a value between $1/(2\pi)$ and $1/\pi$. If the top and bottom surfaces were completely decoupled from each other with an insulating bulk state, A should be close to $1/\pi$. On the other hand, if the bulk of the film dominates and/or the bulk and two surfaces behave as a strongly coupled single entity, then the value should reduce to $1/(2\pi)$ (⁹⁰Kim *et al.*, 2011). Fig. 6-4c shows that our films are somewhere between these two extremes. However, if the bulk contribution to the WAL effect were significant, l_ϕ should grow with thickness (⁹⁰Kim *et al.*, 2011). Therefore, l_ϕ being almost thickness-independent between ~ 8 and 128 QL in Fig. 6-4d is a clear indication that the observed WAL effect originates mainly from surface channels (⁹⁰Kim *et al.*, 2011).

6.3 Quantum Confinement

The most notable feature in Fig. 6-2d is that one channel (n_{SC-1}) provided a nearly constant sheet carrier density of $\sim 3.0 \times 10^{13} \text{ cm}^{-2}$ all the way down to 2 QL, whereas the other channel (n_{SC-2}) stayed at $\sim 8 \times 10^{12} \text{ cm}^{-2}$ down to ~ 8 QL but gradually decreased for thinner samples. This observation suggests first that a strong pinning mechanism exists for the surface Fermi level and that there exist two well-defined surface transport channels with different mobilities and thicknesses.

Considering that angle-resolved photoemission spectroscopy (ARPES) studies consistently show that downward band bending develops on Bi₂Se₃ surfaces (see Fig. 6-2f) (⁷⁵Analytis *et al.*, 2010; ⁷⁹Bianchi *et al.*, 2010; ⁹¹Chen *et al.*, 2012; ⁹²King *et al.*, 2011), not only the topological surface states but also the two-dimensional electron gas (2DEG) states in the quantum confined accumulation layers can be the sources of these surface channels. The sheet carrier densities (n_{SC}) of the topological surface state and the 2DEG should be given by $n_{SC,TI} = k_{F,TI}^2/(4\pi)$ and $n_{SC,2DEG} = k_{F,2DEG}^2/(2\pi)$, respectively, where k_F stands for the Fermi wave vectors and the factor of 2 difference is due to spin degeneracy. Because $k_{F,2DEG} < k_{F,TI}$, we should always have $n_{SC,2DEG} < n_{SC,TI}$. Therefore, with $n_{SC-1} \sim 3.0 \times 10^{13} \text{ cm}^{-2}$ and $n_{SC-2} \sim 8 \times 10^{12} \text{ cm}^{-2}$, the inequality is satisfied only if n_{SC-1} is from TI band and n_{SC-2} is from the 2DEG, but not the other way round.

As seen in Fig. 6-2d, the sheet carrier densities corresponding to the two conducting channels remain constant up to a film thickness of 256 QL. Thus, the bulk contribution (scaling linearly with thickness) excluding the 2DEG channel must be lower than either of these two channels. From $n_{SC-2} \sim 1 \times 10^{13} \text{ cm}^{-2}$ for the 256 QL sample, we get $n_{bulk} < n_{SC-2}/t \Rightarrow n_{bulk} < 5 \times 10^{17} \text{ cm}^{-3}$. Now from $n_{bulk} = k_{F,bulk}^3/(3\pi^2)$, where $k_{F,bulk}$ is the Fermi wave number, we get $k_{F,bulk} < 0.025 \text{ \AA}^{-1}$. Using effective mass $m^* \sim 0.15m_e$ (⁷⁵Analytis *et al.*, 2010), this limits the bulk Fermi level (E_F) to less than 15 meV from the bottom of the conduction band, CB_{min} . According to our two-carrier model, if the surface states contribute equally on both surfaces, the spin non-degenerate carrier density due to SS is $n_{TI} \sim 1.5 \times 10^{13} \text{ cm}^{-2}$, giving a Fermi

wave number, $k_{F,TI} \sim 0.14 \text{ \AA}^{-1}$. On the other hand, the spin degenerate sheet carrier density for the 2DEG is given by $n_{2DEG} \sim 4 \times 10^{12} \text{ cm}^{-2}$, resulting in $k_{F,2DEG} \sim 0.05 \text{ \AA}^{-1}$, which implies that with $m^* \sim 0.15m_e$, E_F should be $\sim 60 \text{ meV}$ from the bottom of the 2DEG level.

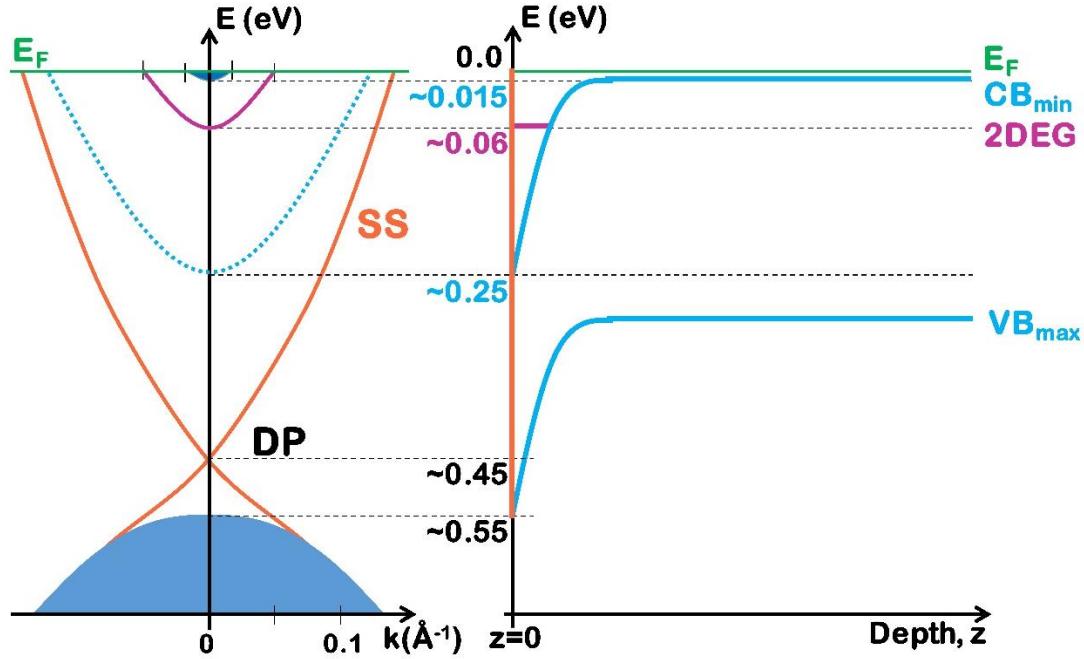


Fig. 6-5. Schematic of k-space energy dispersion and band-bending: the left schematic shows the k-space energy dispersion on a Bi_2Se_3 surface. Without 2DEG, surface electrons will occupy all the way to the bottom of the conduction band, but if the quantum confinement works effectively, 2DEGs will form and there will be a gap between the minimum occupied level and CB_{min} on the surface. Because the level of bend banding and quantum confinement depends on the bulk carrier density and the surface history, this schematic may not exactly match the ARPES spectra available in the literature. The right schematic describes the downward band bending near the surface.

These energy levels are shown together in Fig. 6-5. The dotted line is the bulk conduction band projected onto the surface. In ARPES spectrum, both the conduction band features and the 2DEG states may coexist. Most ARPES studies in the literature showing the band-bending effect were done on samples with much higher carrier

densities ($\gg 5 \times 10^{17} \text{ cm}^{-3}$) than ours, and considering that the band-bending effect is more severe for low carrier samples, it is plausible to expect that our samples have more severe band bending than the commonly available ARPES spectra in the literature.

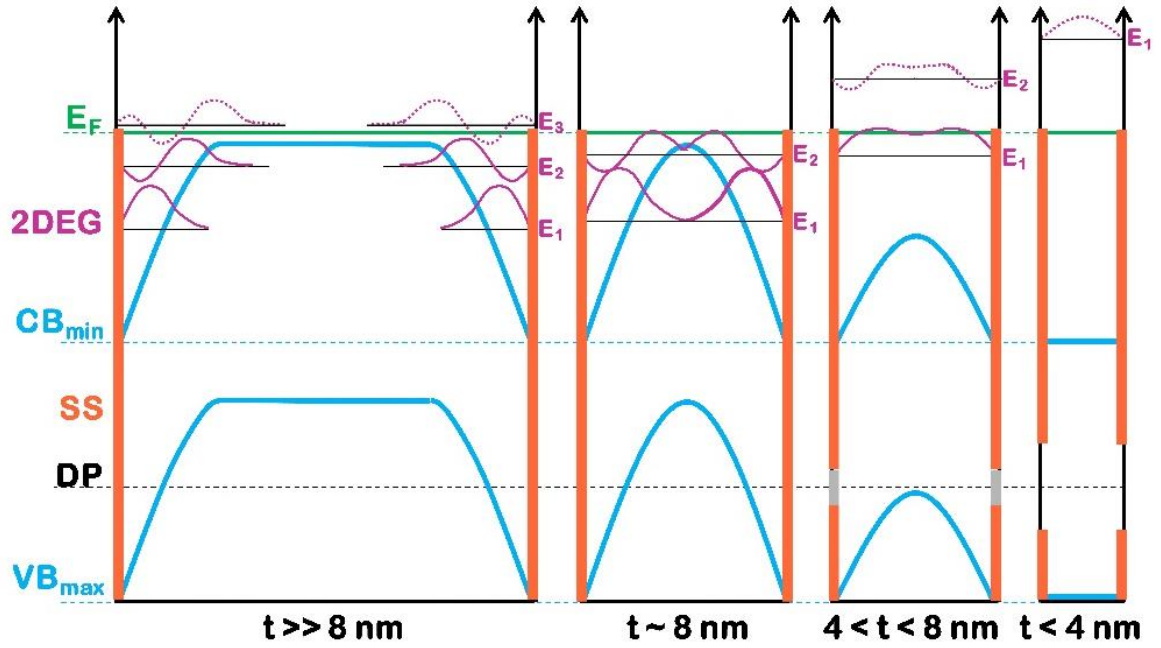


Fig. 6-6. Energy levels in the 2DEG: this schematic shows how the quantized 2DEG levels in the accumulation layers are affected by the film thickness when the surface Fermi level is pinned. The approximate wavefunctions corresponding to the 2DEG energy levels are shown in purple; the surface states are in orange; CB_{min} and VB_{max} are shown in blue. For simplicity, energy level splittings due to wavefunction overlap are ignored in these schematics. Gap formation at the Dirac point (for $t < 6 \text{ QL}$) is depicted as gray and black lines on the orange surface states.

When the thickness of the sample approaches that of the 2DEG, the confinement will start affecting the energy levels of the 2DEG. Because the film is confined by air on one side and the sapphire substrate on the other, the thickness confinement can be well approximated by the simple infinite square potential well model. This confinement along the z -direction (or the direction of growth) leads to

quantized energy levels as shown in Fig. 6-6. As seen in Fig. 6-2d-inset, the carrier concentration corresponding to the accumulation layer increases slowly up to a thickness of ~ 8 QL and then remains almost constant, within an error bar, all the way up to 256 QL. Assuming a symmetric band bending at both interfaces, the 2DEG thickness can be taken as ~ 4 QL thick at each surface. In this scenario, for thick films ($t \gg 8$ QL), the SS and the 2DEG on the opposite surfaces are well separated. As the film thickness is reduced, comparable to ~ 8 QL, the 2DEGs from opposite surfaces will start overlapping, and the thickness confinement will take over the band bending confinement as depicted in Fig. 6-6.

For an infinite well, the n^{th} energy level from the bottom of the well (the conduction band minimum in this case) is given by: $E_n = (n\hbar\pi)^2 / (2m^*t^2)$, where \hbar is the reduced Planck's constant, m^* is the effective electron mass ($\sim 0.15m_e$, where m_e is the bare electron mass), and t is the thickness of the film. For a film thickness of 8 nm, the three lowest energy levels are found to be 0.04 eV, 0.16 eV, 0.35 eV, while the lowest energy level for a 2 nm thick films is 0.63 eV from the surface CB_{min} . When compared with the typical band-bending energy of 0.1~0.3 eV reported in ARPES studies (⁷⁵Analytis *et al.*, 2010; ⁷⁹Bianchi *et al.*, 2010; ⁹¹Chen *et al.*, 2012; ⁹²King *et al.*, 2011), the 2DEG will start feeling the thickness effect by ~ 8 QL, and will be so severely affected by 2 QL that there will not be any allowed energy levels below the surface Fermi level, schematically shown in Fig. 6-6. These analyses suggest that $n_{\text{SC}-1}$, which is constant down to 2 QL, is unlikely to originate from the 2DEG, whereas $n_{\text{SC}-2}$, which starts to change at ~ 8 QL, is more consistent with the expected behavior of a 2DEG.

According to the standard TI theory, the thickness of a topological surface state (⁷⁷Linder *et al.*, 2009) is ~ 1 nm, which is given by $\hbar v_F / E_g$, where v_F ($= 4.5 \times 10^5$ m/s) is the Fermi velocity of the Bi₂Se₃ surface band and E_g ($= 0.3$ eV) is the bulk band gap of Bi₂Se₃ (²⁴Xia *et al.*, 2009; ⁹³Hsieh *et al.*, 2009); this implies that the thickness of the top and bottom surface states combined should be ~ 2 nm, which turns out to be exactly the thickness of the first channel, n_{SC-1} . If we assume that each of the top and bottom surfaces contribute equally to the observed carrier density of $\sim 3.0 \times 10^{13} \text{ cm}^{-2}$, n_{SC-1} provides $k_{F,TI}$ of 0.14 \AA^{-1} , and this value is within the range that ARPES reports on band-bent Bi₂Se₃ samples (⁷⁵Analytis *et al.*, 2010; ⁷⁹Bianchi *et al.*, 2010; ⁹¹Chen *et al.*, 2012; ⁹²King *et al.*, 2011). There is a subtle point to discuss here, though. It is known from an ARPES study that the Dirac point on the surface band disappears for films thinner than 6 QL (⁶¹Zhang *et al.*, 2010); however, if the surface Fermi level is far from the Dirac point, as depicted in Fig. 6-2g, the sheet carrier density, which is simply a measure of k_F^2 , should not be much affected by gap-opening at the Dirac point. Therefore, our observation of the constant sheet carrier density of the topological surface states down to 2 QL is not in contradiction with this gap-opening phenomenon at the Dirac point.

6.4 Shubnikov de Haas Oscillations

According to the above discussion, n_{SC-2} is likely from an ~ 8 nm thick surface 2DEG. If we assume symmetric band bending on both the top and bottom surfaces, the 2DEG corresponds to $n_{SC,2DEG}$ of $\sim 4 \times 10^{12} \text{ cm}^{-2}$ on each surface with half the thickness. With $n_{SC,2DEG} = k_{F,2DEG}^2 / (2\pi)$, this converts to $k_{F,2DEG}$ of 0.05 \AA^{-1} . Interestingly, this Fermi

wave vector is close to those obtained from Shubnikov–de Haas (SdH) oscillations of these samples, as discussed in the following section. However, no SdH oscillations were observed around k_F of 0.14 \AA^{-1} , the value associated with the topological surface band.

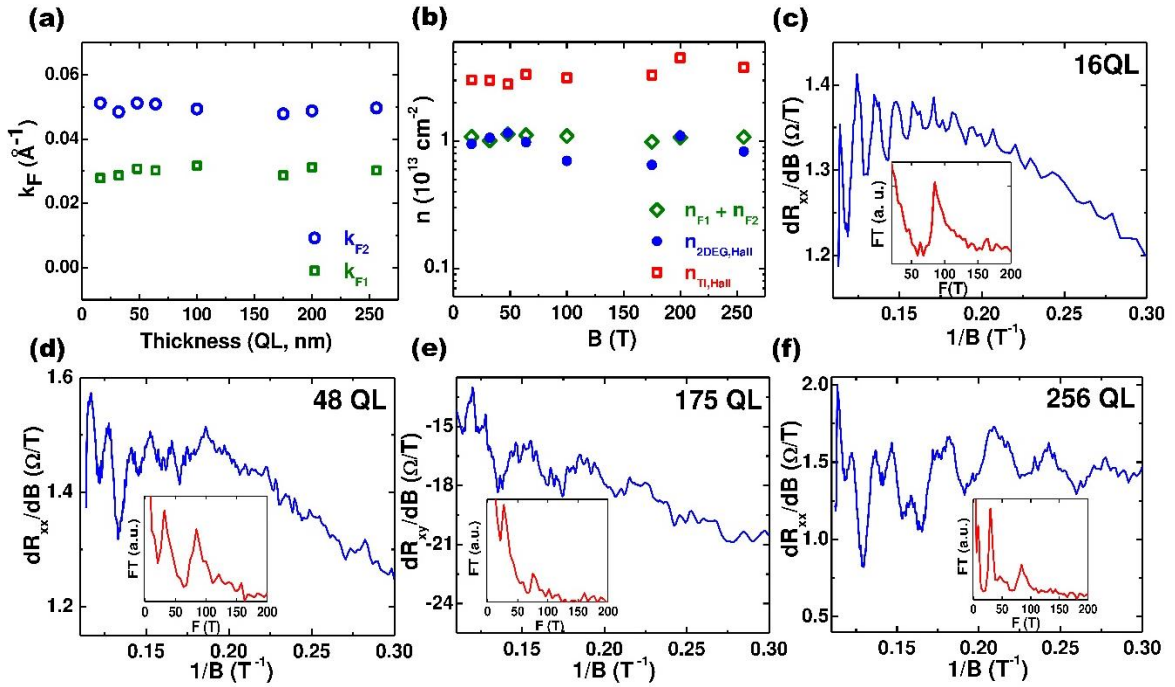


Fig. 6-7. SdH measurements. **(a)** SdH-measured Fermi wave vectors as a function of sample thickness. **(b)** Comparison of the sheet carrier densities obtained from the two-carrier fitting of the Hall effect and the equivalent sheet carrier densities estimated from (a) as a function of thickness. **(c-f)** SdH oscillations observed in dR_{xx}/dB and dR_{xy}/dB for various thicknesses; corresponding Fourier transforms are shown in the insets.

The mobilities in Fig. 6-2e also show thickness independence, within some error bars, down to $4 \sim 8$ QL. However, unlike n_{SC-1} , which remained constant down to 2 QL, its mobility, μ_{SC-1} , clearly degraded for ultrathin films. This difference can be understood by the fact that unlike the carrier density, which is simply a measure of the Fermi surface area, mobility is a measure of scattering time and thus susceptible to disorders and interactions, which is likely to become more significant

for ultrathin samples. Another notable feature is that μ_{SC-1} is substantially smaller than μ_{SC-2} over the entire thickness range. This observation may look puzzling according to the common expectation that the mobility of the topological surface band should be high due to absence of backscattering. However, this expectation should be taken with caution. First of all, the topological protection mechanism guarantees only the metallicity of the surface state, and the mobility should still depend on the details of interactions. Second, considering that the backscattering accounts for only a small fraction of the scattering (²⁵Roushan *et al*, 2009) and that the topological surface state is spatially more confined than the 2DEG, there is no fundamental reason that the topological surface state should have a higher mobility than the 2DEG.

It is well known that Shubnikov-de Haas (SdH) effect is highly sensitive to the mobility of the sample and $\mu B \gg 1$ is critical for the observation of SdH oscillations; thus, we may or may not observe SdH oscillations from any of these surface channels, even if both are metallic. From the Hall-effect measurements, with $\mu_{SC-1} \approx 0.05 \text{ m}^2\text{V}^{-1}\text{s}^{-1}$, $\mu_{SC-2} \approx 0.3 \text{ m}^2\text{V}^{-1}\text{s}^{-1}$, and $B_{max} = 9 \text{ T}$, we get $\mu_{SC-1}B_{max} \approx 0.5$ and $\mu_{SC-2}B_{max} \approx 3$. According to these numbers, we expect some SdH oscillations are more likely from SC-2 (2DEG) but none from SC-1 (topological surface band).

In fact, SdH oscillations were observed in many films with thickness of 16 QL or above. In all these samples, two SdH frequencies were observed (see Figs. 6-7c – 6-7f): $F_1 \sim 30 \text{ T}$ and $F_2 \sim 85 \text{ T}$. These frequencies relate to the size of the Fermi surface via the Onsager relation, $F = (\hbar/(2\pi e))(\pi k_F^2)$, where \hbar is the reduced Planck's

constant, e is the electron charge, and k_F is the Fermi wave number. These numbers correspond to the wave vectors $k_{F1} \sim 0.03 \text{ \AA}^{-1}$ and $k_{F2} \sim 0.05 \text{ \AA}^{-1}$, respectively. If the Fermi surface is two dimensional, its 2D carrier density is related to k_F as: $n_{2D} = k_F^2/2$. The 2D carrier densities corresponding to these Fermi wave numbers are $n_1 \sim 1 \times 10^{12} \text{ cm}^{-2}$ and $n_2 \sim 4 \times 10^{12} \text{ cm}^{-2}$; n_{F1} and n_{F2} plotted in Fig. 6-7b are twice these numbers taking into account top and bottom surfaces. As seen in Fig. 6-7b, the sum of these two carrier densities match very nicely the 2DEG channel value we identified from the Hall measurement.

The very observation that the two very different measurements, the SdH oscillation and the two-carrier Hall effect fitting, provide very similar carrier densities for one of the Hall effect carriers strongly supports the reliability of our two-carrier model. As for the dominating SdH channel ($k_{F2} \sim 0.05 \text{ \AA}^{-1}$ with $n_2 \sim 4 \times 10^{12} \text{ cm}^{-2}$), if we assume a 3D Fermi surface with thickness-independent 3D carrier density, it is impossible to match with the Hall measurement, and so it definitely has to be of 2D nature, most likely a 2DEG as discussed above.

However, the story can be a little different for the smaller channel ($k_{F1} \sim 0.03 \text{ \AA}^{-1}$ with $n_1 \sim 1 \times 10^{12} \text{ cm}^{-2}$). Because the 2DEG is almost dominated by k_{F2} channel, although k_{F1} channel could also originate from another 2DEG level (say, E2 from Fig. 6-6), we cannot completely rule out the possibility of it being a 3D channel. Based on the carrier density analysis of the thickest film (256 QL) in section 6.3, we estimated that $k_{F,bulk} < 0.025 \text{ \AA}^{-1}$, and so $k_{F1} \sim 0.03 \text{ \AA}^{-1}$ could be within this limit, considering the

error bars in our measurement. Detailed angle dependent studies of each channel up to higher magnetic field will be needed to resolve this issue completely.

6.5 Conclusion

In summary, the channel with $k_F \approx 0.05 \text{ \AA}^{-1}$ observed in both SdH oscillation and Hall effect is best described by the 2DEG; and the smaller channel with $k_F \approx 0.03 \text{ \AA}^{-1}$ detected in SdH oscillation could be either a higher-level 2DEG or a residual bulk channel; but the channel with $k_F \approx 0.14 \text{ \AA}^{-1}$, which appeared only in Hall effect and maintained its metallicity all the way down to 2 QL, cannot be explained by the 2DEG and is most likely from the TI surface states.

In summary, significant advances in Bi_2Se_3 thin film qualities allowed observation of dominant, thickness – independent surface transport channels. Conductance, sheet carrier densities, mobilities, and WAL parameters remained nearly independent of thickness over two orders of the thickness range. Such thickness-independent transport properties, trivially expected in TIs, were never observed before because of nontrivial bulk effects. In order to explain the observed surface transport properties, not only the topological surface states but also the quantum confined 2DEG channels have to be considered. How each of these different surface channels responds against various excitations is an important scientific and technological question that needs to be further investigated in future studies.

Chapter 7. ROBUST TOPOLOGICAL SURFACE STATES OF Bi_2Se_3 ON AMORPHOUS SiO_2/Si & AMBIPOLAR GATING EFFECT⁷

In order to utilize the unique properties of these topological surface states (TSS), numerous efforts have been made to grow Bi_2Se_3 films on various substrates (⁵⁸Zhang *et al.*, 2009; ⁶³Richardella *et al.*, 2010; ⁶⁴Chen *et al.*, 2010; ⁸⁸Li *et al.*, 2010; ⁸⁹Bansal *et al.*, 2011; ⁹⁰Kim *et al.*, 2011; ⁹⁴Wang *et al.*, 2011; ⁹⁵Tarakina *et al.*, 2012; ⁹⁶Bansal *et al.*, 2012; ⁹⁷Taskin *et al.*, 2012; ⁹⁸Chang *et al.*, 2011; ⁹⁹Zhang *et al.*, 2012; ¹⁰⁰Kou *et al.*, 2011; ¹⁰¹He *et al.*, 2012; ¹⁰²Jerng *et al.*, 2013). Among these, amorphous SiO_2 (a- SiO_2)/Si substrate stands out the most due to its unique standing in modern electronics and ease for back-gating. However, due to the complete lack of epitaxial template from the amorphous substrate, there have been only limited efforts to utilize a- SiO_2 /Si substrates for TI films (¹⁰² Jerng *et al.*, 2013), and many key questions including whether TSS survives on such an amorphous substrate remain unknown. The layered structure of Bi_2Se_3 allows mitigation of the lattice matching constraint; the weak bonding between the layers allows the epilayer lattice constant to relax to its bulk

⁷ This chapter is based on work published in ¹²³N. Bansal *et al.*, Applied Physics Letters **104**, 241606 (2014).

value with no strain at the interface between the substrate and the film. However, little is known about how robust the topological surface states (TSS) are against disorders and other detrimental effects originating from the substrates.

7.1 Bi₂Se₃ Film Growth on SiO₂/Si

The thin Bi₂Se₃ films were grown on 3-in. oxidized silicon wafers (400 nm SiO₂/doped-Si). The base pressure of the system was $\sim 1 \times 10^{-10}$ Torr. Bi and Se fluxes were provided by Knudsen cells and were calibrated using a quartz crystal microbalance and Rutherford backscattering spectroscopy. The oxidized silicon wafers were cleaned *ex-situ* by exposing the substrate to UV-ozone for 5 min before mounting in the MBE chamber to burn off the majority of organic compounds that may be present on the surface. Second cleaning step employed was to heat the substrates up to 300 °C in oxygen pressure of 10^{-6} Torr for 15 min. Oxygen was used both as an agent to burn off any remnant organics on the surface and prevent the formation of pinholes etc in the SiO₂ layer.

The amorphous nature of silicon dioxide is evident in the diffused RHEED pattern (Fig. 7-1a); evolution of the film surface during growth, as monitored by RHEED, is shown in Fig. 7-1. Due to the amorphous template, there is no preferred crystal orientation for Bi₂Se₃ to grow, and thus, the first 3 QLs of Bi₂Se₃ grown at 110 °C resulted in randomly oriented crystallites; RHEED shows a set of concentric ring-like pattern indicating polycrystalline growth (Fig. 7-1b).

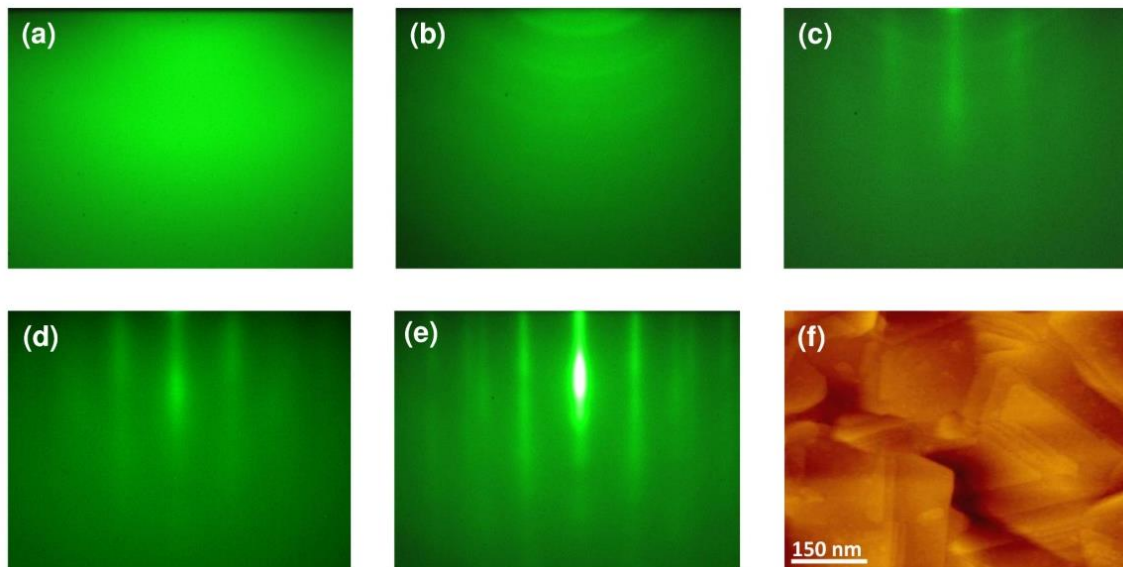


Fig. 7-1. Evolution of RHEED pattern during growth of Bi_2Se_3 film on a- SiO_2 substrates. **(a)** Amorphous SiO_2 substrate. **(b)** After deposition of 3 QL at 110 °C, a polycrystalline ring-like pattern is seen. **(c)** The diffraction pattern evolves to streaky pattern as the film is annealed to 220 °C. **(d)** Streaky pattern indicative of a single-crystalline structure improves on deposition of another 3 QL at 220 °C. **(e)** Final RHEED pattern of a 50 QL film. The RHEED pattern is rotationally invariant, implying the film is composed of random in-plane domains. **(f)** AFM image of a 60 QL film grown on a- SiO_2 . It is composed of randomly orientated triangular islands with QL-step terraces, which is consistent with the RHEED pattern of rotational invariance.

As the substrate was slowly annealed from low temperature to the second growth temperature of 220 °C in Se ambience, the RHEED showed a transition from poly-crystalline ring pattern to weak streaky pattern indicative of single crystalline-like Bi_2Se_3 structure (Fig. 7-1c). On another 3 QL deposition at 220 °C, sharp streaky pattern is observed (Fig. 7-1d). The RHEED pattern became sharper with further growth (Fig. 7-1e). However, in contrast to the RHEED patterns of the Bi_2Se_3 films grown on Si(111) (⁸⁹Bansal *et al.*, 2011) and $\text{Al}_2\text{O}_3(0001)$ (⁹⁶Bansal *et al.*, 2012) with the same two-step process, which show six-fold symmetry with sample rotation, the RHEED pattern observed here remains identical against sample rotation. This implies that the films on a- SiO_2 are composed of random in-plane domains; this is also

evidenced in the atomic force microscopy (AFM) image in Fig. 7-1f, which exhibit randomly oriented triangular islands.

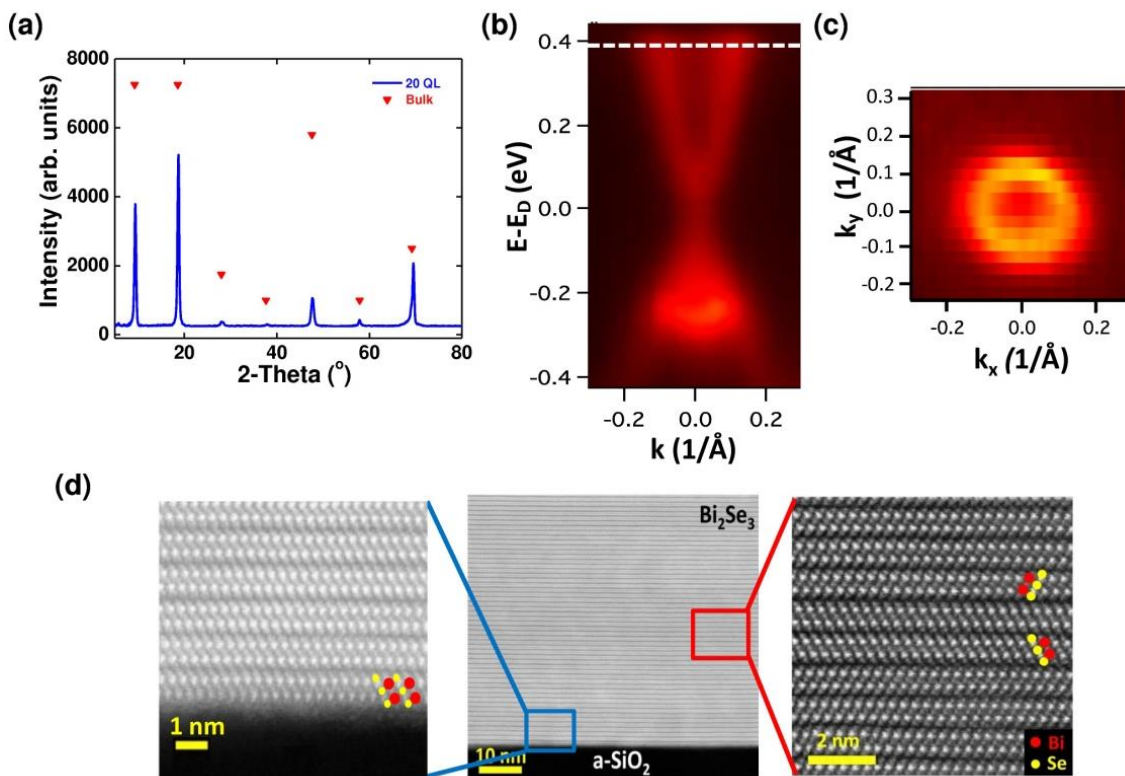


Fig. 7-2. XRD, ARPES and STEM images of Bi₂Se₃ films on a-SiO₂ substrates. **(a)** XRD scan for 20 QL film. **(b)** ARPES spectrum for a 60 QL film. **(c)** Cross-sectional plot of (b) in the k_x-k_y plane at the energy level shown as the dotted line in (b). **(d)** HAADF-STEM cross-section image of the whole structure of a 60 QL film. All the images show nice c-axis layering without any disruption in the QL sequence. The left zoomed-in image shows the interface between the Bi₂Se₃ film and the a-SiO₂ substrate; even the first QL is well defined other than the very bottom Se atoms. The right zoomed-in image shows well-defined Se-Bi-Se-Bi-Se ordering within each quintuple layer and occasional stacking faults between quintuple layers due to weak interlayer coupling.

X-ray diffraction (XRD), scanning transmission electron microscopy (STEM), and ARPES studies were carried out to further characterize these films. The XRD measurements were carried out using a Nonius FR571 rotating-anode generator with a copper target and a graphite monochromator, giving a wavelength of 1.5418 Å and

with a Bruker HiStar multi-wire area detector. The STEM sample was prepared by focused ion beam with final Ga^+ ion energy of 5 keV. A JEOL ARM 200CF equipped with a cold field-emission gun and double spherical-aberration correctors operated at 200kV were used for high-angle annular-dark-field (HAADF) STEM. The collection angles for HAADF detectors were 68 to 280 mrad. The ARPES experiments were carried out at the beam-line 12.0.1 of the Advanced Light Source, Lawrence Berkeley National Laboratory. The film was protected with a Se over-layer after growth and decapped *in-situ* by heating in the final vacuum environment of the analysis chamber.

In Fig. 7-2a, the XRD θ - 2θ scan of a 20 QL Bi_2Se_3 film exhibits only (0 0 3n) diffraction peaks, which implies that the film is fully ordered along the c-axis. This is also consistent with the cross-sectional STEM images shown in Fig. 7-2d, which reveal atomically ordered structure down to the first quintuple layer. Individual Bi_2Se_3 QLs with full c-axis ordering except for occasional stacking faults between QLs are clearly visible. The interface between Bi_2Se_3 and a- SiO_2 is sharp with the atomic layer sequence maintained down to the first quintuple layer, as highlighted by spherical dots in Fig. 7-2d, and the amorphous nature of a- SiO_2 does not impact the growth along the c-direction beyond the first QL. In Fig. 7-2b, ARPES clearly shows the V-shaped Dirac surface band; the constant energy Fermi surface map in the k_x - k_y plane around Γ -point in Fig. 7-2c shows a ring-like feature formed by the surface states.

7.2 Transport Properties: Substrate Effect

The wafer was cut into $\sim 1 \times 1 \text{ cm}^2$ substrates and the transport measurements were then carried out in the standard van der Pauw geometry. Temperature dependence

of sheet resistance (Fig. 7-3a) exhibits fully metallic behavior for films thicker than 10 QL. However, films thinner than ~ 10 QL develop an upturn in the sheet resistance at low temperatures due to low mobilities of these ultrathin samples. This implies that even if the films exhibit full c-axis ordering down to the first quintuple layer, the presence of random domains and correspondingly reduced mobilities leaves this system in a weakly insulating phase in this ultrathin regime despite the presence of the topological surface states as confirmed by the ARPES measurement (see Figs. 7-2b and 7-2c). Fig. 7-3b shows the sheet carrier densities (n_{2D}) and respective mobilities extracted from Hall effect data from the slope of R_{xy} vs. B (± 0.6 T); n_{2D} changes from $\sim 0.5 \times 10^{13} \text{ cm}^{-2}$ (6 QL) to $\sim 3.6 \times 10^{13} \text{ cm}^{-2}$ (100 QL), while the mobility increases fast with film thickness up to 20 QL and remains constant above ~ 20 QL at $\sim 2000 \text{ cm}^2/\text{V s}$.

Figs. 7-3c and 7-3d compare these films with those grown on single-crystalline substrates, Si(111) (⁹⁰Kim *et al.*, 2011) and Al₂O₃(0001) (⁹⁶Bansal *et al.*, 2012); all films were grown under nominally identical growth conditions using the same two-temperature growth process (⁸⁹Bansal *et al.*, 2011): for consistency, all the sheet carrier densities and mobilities are obtained from the same temperature (1.5K) and range of magnetic field (± 0.6 T).

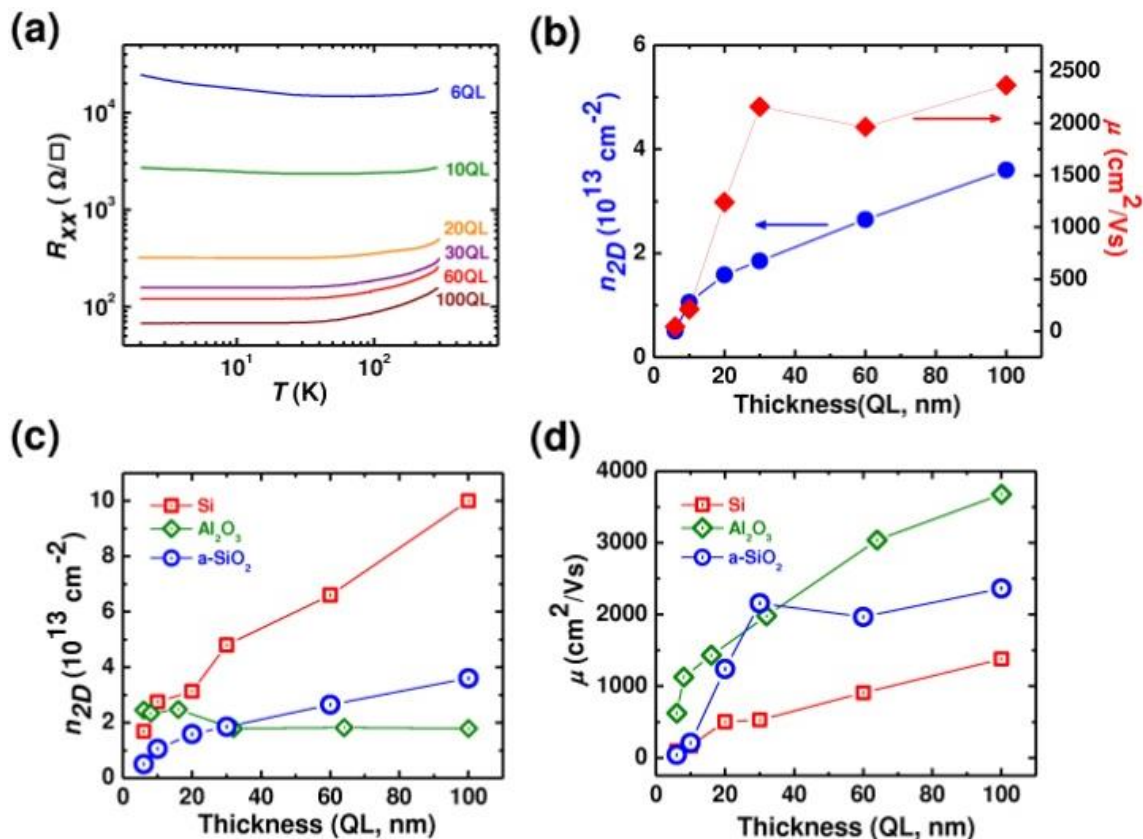


Fig. 7-3. Transport properties of Bi₂Se₃ films grown on a-SiO₂ (a and b); and their comparison with those on Si(111) and Al₂O₃(0001) (c and d) ($T = 1.5 \text{ K}$, $B = \pm 0.6 \text{ T}$). **(a)** Resistance vs. temperature for different thicknesses for a-SiO₂. **(b)** Sheet carrier densities (circles) and mobilities (diamonds) vs. thickness for a-SiO₂. **(c)** Sheet carrier densities and **(d)** mobilities vs. thickness for different substrates. Carrier densities of Bi₂Se₃ grown on a-SiO₂ are always lower than those on Si(111). Moreover, although the mobilities of Bi₂Se₃ grown on a-SiO₂ are comparable to those on Si(111) for thickness less than 10 QL, they quickly surpass those on Si substrates at larger thicknesses.

The first thing to notice is that films grown on a-SiO₂ have lower sheet carrier densities than those on Si(111) over the entire thickness range (Fig. 7-3c); this implies that both surface and bulk defect densities of the films on a-SiO₂ substrates are lower than those on Si(111). On comparison to those on Al₂O₃(0001), the films on a-SiO₂ exhibit lower carrier densities in the thin regime ($\leq 30 \text{ QL}$) but higher values for thicker films. Mobility comparison in Fig. 7-3d shows that Bi₂Se₃ films grown on

both $\text{Al}_2\text{O}_3(0001)$ and a- SiO_2 exhibit superior values to those on $\text{Si}(111)$. Only in the ultrathin regime (≤ 10 QL), the mobilities exhibited by the films on $\text{Si}(111)$ and a- SiO_2 are comparable. This comparison clearly shows that with this standard growth recipe, the amorphous SiO_2 substrate is a superior template than the single-crystalline $\text{Si}(111)$ for the transport properties of Bi_2Se_3 thin films.

The very observation that a- SiO_2 provides better template than $\text{Si}(111)$ for the transport properties of Bi_2Se_3 is surprising. From structural point of view, Bi_2Se_3 films on a- SiO_2 , even if they exhibit nice c-axis ordering as shown in Fig. 7-2d, are not as good as those on $\text{Si}(111)$ substrates, which are fully single crystalline along both c-axis and ab-plane as shown in Ref. 63. Therefore, the better transport properties observed on a- SiO_2 than on $\text{Si}(111)$ cannot be of structural origin. Although further studies will be needed to clarify this, one plausible scenario is as follows. Unlike SiO_2 and Al_2O_3 substrates, Si is chemically reactive and is a dopable semiconductor. Therefore, even if our two-step growth method suppresses any chemical reaction at the interface, it may still be possible for Bi_2Se_3 films and Si substrates to dope each other through an atomistic diffusion process, which would lead to increased carrier densities and reduced mobilities, whereas such a process is forbidden on the inert oxide substrates such as SiO_2 and Al_2O_3 .

Similar process could occur between Bi_2Se_3 and any other chemically reactive semiconductor substrates. For example, transport properties of Bi_2Se_3 films grown on $\text{SiC}(0001)$ substrate are known to be complicated by the graphene-like conducting channel at the interface (⁹⁸Chang *et al.*, 2011). Similarly, the anomalous transport properties previously observed in Bi_2Se_3 films on CdS substrates could be due to such

an inter-diffusion process (¹⁰⁰Kou *et al.*, 2011; ¹⁰¹He *et al.*, 2012). Another problem with these dopable semiconductor substrates is that once inter-diffusion or some other electronically active process occurs between the film and the substrate, it is hard to distinguish which of the transport contributions are intrinsic to the TI films and which are not. This observation suggests that for layered TI materials, chemical compatibility between the films and the substrate is a more (or at least, no less) important factor than the lattice matching for their transport properties.

7.3 Electrostatic Back - Gating

Finally, the Bi₂Se₃ films grown on a-SiO₂ on doped-Si substrates allowed an effective back-gating. For gating, a 1×1 cm² piece of an 8 QL film was cut out and then ion milled in argon plasma using a shadow mask to make the Hall bar device, and the highly doped Si substrate was used as the back gate.

Fig. 7-4a shows the device schematic with Fig. 7-4b showing an optical image of a part of the device; the Hall bar width is 0.56 mm and the length measured between the mid points of the longitudinal voltage probes is 2.1 mm. Fig. 7-4c shows the sheet resistance, R_{xx} , and Hall coefficient, R_H , as a function of applied gate voltage, V_G ; the corresponding sheet carrier density and mobility are shown in Fig. 7-4d. We found that for Bi₂Se₃ films grown on SiO₂, air exposure tends to reduce both carrier concentration and mobility of the sample.

For this sample, in the absence of any gate voltage, the sheet carrier density was $5 \times 10^{12} \text{ cm}^{-2}$, lower than the fresh samples of similar thicknesses shown in Fig. 7-3 and the sheet resistance (R_{xx}) was 15.22 k Ω /sq. about half of the quantum

resistance ($h/e^2 \approx 25.8 \text{ k}\Omega$). When positive gate bias was applied, R_{xx} decreased as more n-type carriers were injected into the film. On the other hand, with negative gate bias, the resistance increased as the n-type carriers were depleted, surpassing the quantum resistance of $25.8 \text{ k}\Omega$ at $V_G = -50 \text{ V}$. When the negative gate bias passed $V_G = -82 \text{ V}$, R_{xx} reached a peak of $\sim 100 \text{ k}\Omega/\text{sq}$ and the Hall resistance changed its sign to p-type, indicating that the system passed the Dirac point at this gate voltage.

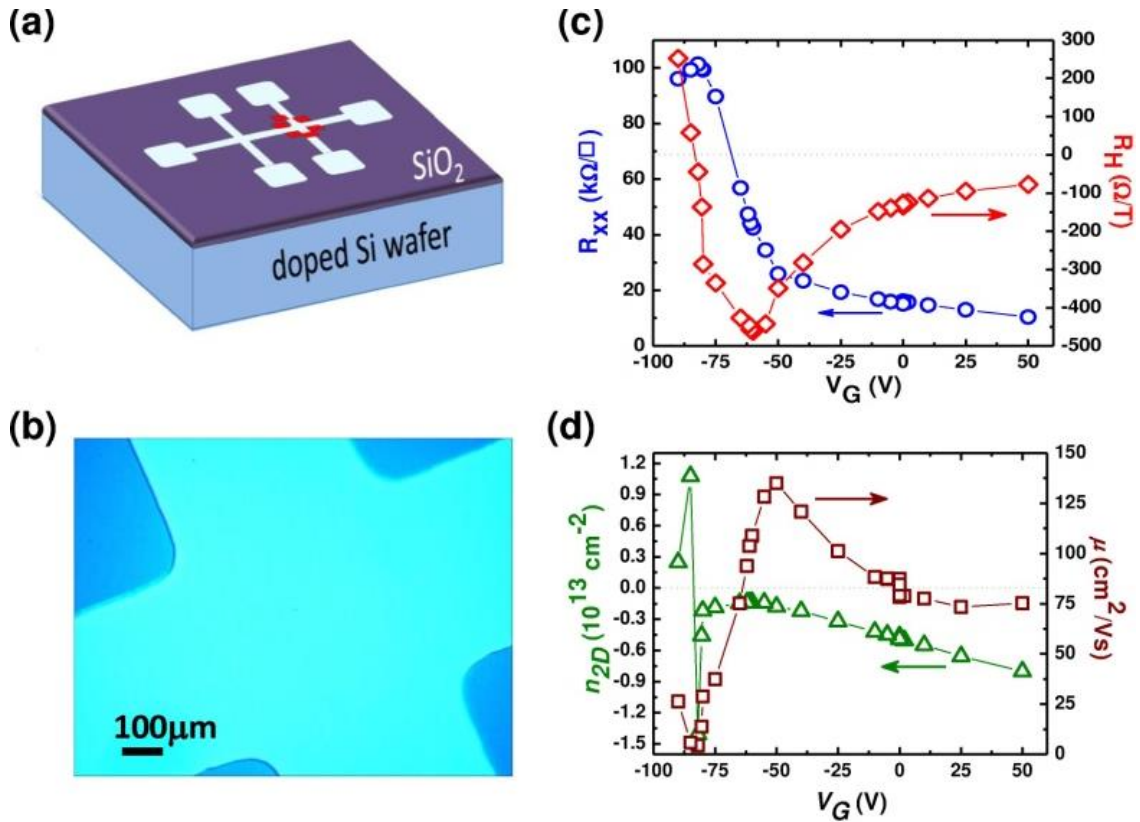


Fig. 7-4. Electrostatic back-gating of an 8 QL Bi₂Se₃ film on a-SiO₂/doped-Si substrate ($T = 6 \text{ K}$, $B = \pm 0.6 \text{ T}$). **(a)** Schematic for the Hall bar device. Optical image of the area enclosed by the red dashed square is shown in **(b)**. **(c)** Longitudinal resistance and Hall resistance, **(d)** corresponding sheet carrier densities and mobilities of the back-gated 8 QL film as a function of the gate voltage.

7.4 Conclusion

In summary, we have shown that Bi_2Se_3 films grown on amorphous SiO_2 substrates, despite their random in-plane disorders, exhibit a well-defined Dirac surface band, and superior transport properties to those on single-crystalline $\text{Si}(111)$ substrates. A large ambipolar electric field effect was observed on these films using the underneath doped-Si substrate as the back gate. This work sheds light on the importance of chemical compatibility of the substrate, compared to lattice matching, for the growth of TI thin films, and also demonstrates that the technologically important and gatable $\text{a-SiO}_2/\text{Si}$ substrate is a promising platform for TI electronics.

Chapter 8. TRANSFERRING MBE-GROWN Bi_2Se_3 FILMS TO ARBITRARY SUBSTRATES⁸

Significant progress has been made in understanding the properties of TIs through angle resolved photoemission spectroscopy (ARPES) (²⁴Xia *et al.*, 2009; ²²Hsieh *et al.*, 2008; ¹⁰³Hsieh *et al.*, 2009; ²³Chen *et al.*, 2009) scanning tunneling microscopy (²⁵Roushan *et al.*, 2009) and transport measurements (⁵¹Peng *et al.*, 2010; ⁸³Checkelsky *et al.*, 2011; ⁸⁶Steinberg *et al.*, 2011; ⁹⁰Kim *et al.*, 2011; ⁹⁶Bansal *et al.*, 2012; ¹⁰⁴Checkelsky *et al.*, 2009; ¹⁰⁵Butch *et al.*, 2010; ¹⁰⁶Xiu *et al.*, 2011; ¹⁰⁷Brahlek *et al.*, 2012; ¹⁰⁸Qu *et al.*, 2010). Recently, there is a growing interest in combining TIs with superconductors, (anti)-ferromagnets, and so forth in search of quantum anomalous Hall effect (¹⁰⁹Yu *et al.*, 2010; ¹¹⁰Chang *et al.*, 2013), Majorana fermions (¹¹¹Fu *et al.*, 2008; ¹¹²Akhmerov *et al.*, 2009), or other magneto – electric effects (¹¹³Garate *et al.*, 2010; ¹¹⁴Qi *et al.*, 2009).

Bi_2Se_3 has a rhombohedral structure with a sequence of Se–Bi–Se–Bi–Se forming a quintuple layer (QL, 1 QL \approx 1 nm) along the c-axis direction. This layered structure is held together strongly within the QL but only weakly between layers by

⁸ This chapter is based on work published in ¹³¹N. Bansal *et al.*, Nano Letters **14**, 1343 (2014).

van der Waals forces (⁵²Lind *et al.*, 2005; ⁵³Okamoto, 1994). The weak interlayer bonding enables mechanical exfoliation of thin Bi₂Se₃ flakes from bulk crystals and such flakes have been extensively used to fabricate TI devices (⁵¹Peng *et al.*, 2010; ⁸³Checkelsky *et al.*, 2011; ¹⁰⁴Checkelsky *et al.*, 2009; ¹⁰⁵Butch *et al.*, 2010; ¹⁰⁸Qu *et al.*, 2010; ¹¹⁵Kim *et al.*, 2012; ¹¹⁶Velasco *et al.*, 2011). However, the process of mechanically cleaving bulk crystals results in flakes of limited lateral sizes and ill-defined thicknesses and the yield of obtaining ultrathin flakes (≤ 10 nm) is very low (⁸³Checkelsky *et al.*, 2011; ¹¹⁵Kim *et al.*, 2012; ¹¹⁷Hong *et al.*, 2010; ¹¹⁸Cho *et al.*, 2011). On the other hand, techniques to transfer large-area 2D layered materials are well established in the field of graphene. A polymeric supporting layer has been successfully demonstrated as a transferring template for various 2D materials such as graphene (¹¹⁹Li *et al.*, 2009; ¹²⁰Reina *et al.*, 2009), hexagonal boron nitride (¹²¹Lee *et al.*, 2011), molybdenum disulfide (¹²²Bertolazzi *et al.*, 2011), and so forth. However, such a process has not been developed for TI structures yet. In this work, we aim to develop a transfer process to transfer the entire area of TI Bi₂Se₃ thin films grown epitaxially on Al₂O₃ and SiO₂ to arbitrary substrates. The ability to transfer large area TI films to any substrate will facilitate fabrication of TI heterostructure devices, and help explore other exotic phenomena associated with TIs.

8.1 Transfer Process

High-quality Bi₂Se₃ films were grown on 1 cm \times 1 cm Al₂O₃(0001) substrates (⁹⁶Bansal *et al.*, 2012) and 3 in. oxidized Si wafers (¹²³Bansal *et al.*, 2013) as discussed in Chapter 6 and Chapter 7 respectively. The transfer of these films to various substrates was

carried out using a poly(methyl methacrylate) (PMMA) layer as a transfer support; a single coat of PMMA provides enough mechanical strength to the Bi_2Se_3 film to prevent any cracking during the transfer process.

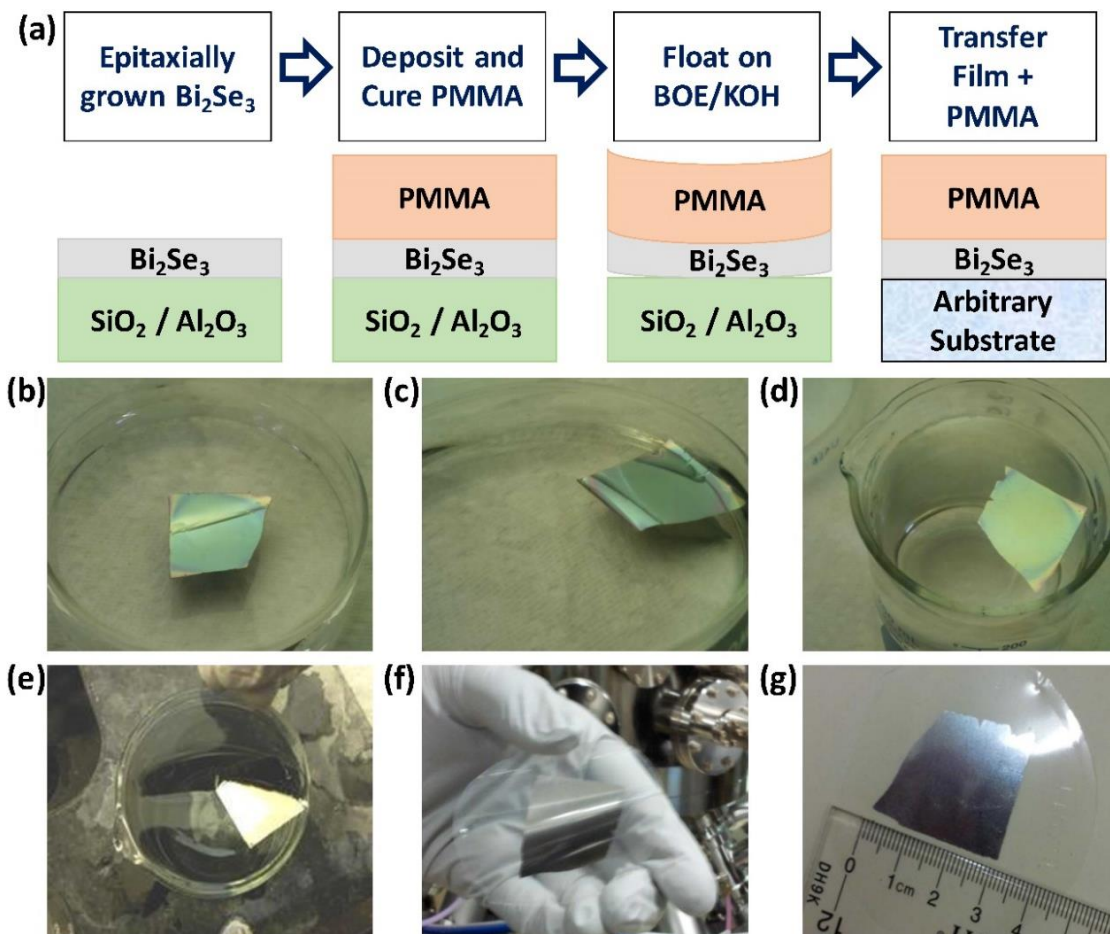


Fig. 8-1. Process for transfer of Bi_2Se_3 thin films. **(a)** Schematic diagram of the PMMA-based transfer method of Bi_2Se_3 films grown on a-SiO_2 or $\text{Al}_2\text{O}_3(0001)$ to any arbitrary substrate. **(b–e)** Photographs of a 30 QL thick Bi_2Se_3 film grown on a-SiO_2 transferred to a common transparency sheet. **(b,c)** PMMA spun on the sample provides enough buoyancy for floating the sample on BOE; as the peeling of the film progresses, the substrate sinks down. **(d)** The PMMA/ Bi_2Se_3 film is then floated in multiple water baths to remove any excess chemicals. **(e)** The PMMA/ Bi_2Se_3 film can be fished out of water using target substrate, a piece of common transparency sheet in this case. **(f)** Film transferred on a flexible substrate allows bending of the film without any cracks visible under an optical microscope. **(g)** Photographs of a $\sim 3\text{cm} \times 3\text{cm}$ Bi_2Se_3 film transferred from a-SiO_2 to a transparency sheet.

Fig. 8-1a shows the schematic for this process. After PMMA (A-6) is spin-coated and baked at 100 °C on top of Bi₂Se₃ film, the sample is floated on buffered oxide etch (BOE) or potassium hydroxide (KOH) solution. The solution acts on the interface between the film and the substrate and the peeling of PMMA/Bi₂Se₃ layer thus initiates from outer edge of the sample. Then, probably by capillary wet etch mechanism, the peeling gradually spreads out (Fig. 8-1b,c). This results in a free-standing PMMA/Bi₂Se₃ film that can be transferred to any desired substrate after rinsing off any excess BOE/KOH using deionized water (Figure 1d,e). After drying the film on the new substrate in ambient air, the PMMA layer can be easily removed by acetone. The detachment of PMMA/Bi₂Se₃ layer from the underlying substrate was much faster for films on a-SiO₂ than on Al₂O₃(0001). This process allows transfer of very large area Bi₂Se₃ films of any thickness to any substrate for multiple applications ranging from back-gating to flexible electronics; Fig. 8-1f,g shows a 30 QL Bi₂Se₃ film of area ~3 cm × 3 cm transferred to a common transparency sheet.

Fig. 8-2 provides the morphological and structural characteristics of the transferred films in optical microscopy (OM), atomic force microscopy (AFM), and transmission electron microscopy (TEM) images. TEM characterization was performed on a 6 QL Bi₂Se₃ film grown on Al₂O₃(0001) and transferred to a carbon foil on a TEM copper grid. A JEOL- 2010F transmission electron microscope (TEM) equipped with a 14-bit charge coupled device (CCD) array detector was used to take the electron diffraction patterns and high-resolution images.

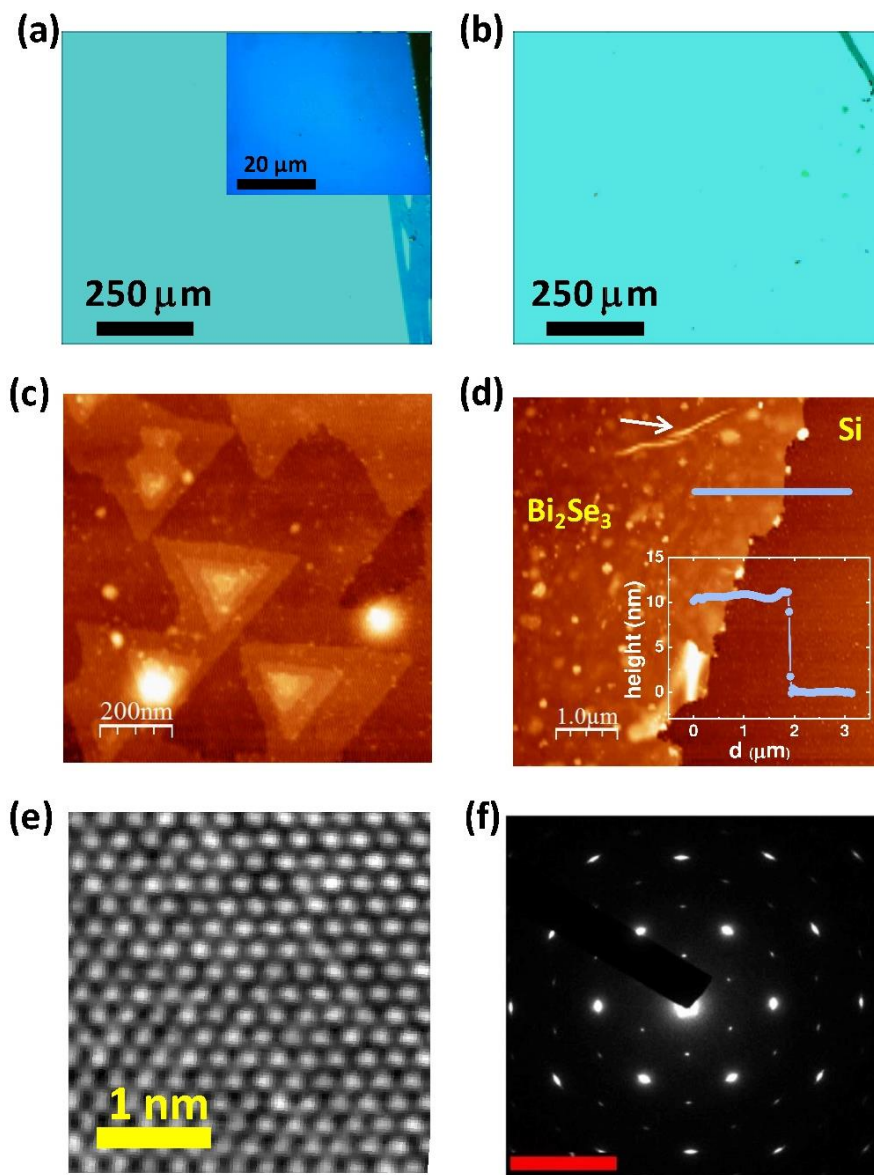


Fig. 8-2. Characterization of the transferred film. **(a,b)** Optical images of a 10 QL Bi_2Se_3 film grown on $\text{Al}_2\text{O}_3(0001)$ transferred to **(a)** $\text{Al}_2\text{O}_3(0001)$ and **(b)** $\text{Si}(111)$. The inset in (a) highlights the edge of the transferred film on Al_2O_3 substrate. The films are intentionally scratched on the sides to get a clear contrast. **(c)** AFM image of the 10 QL film transferred to $\text{Si}(111)$, exhibiting the pristine morphology of the transferred film. This image confirms that the chemicals used in the process do not attack the film. **(d)** A large area AFM image ($5 \times 5 \mu\text{m}^2$) showing the edge of the transferred film; the inset shows the height profile of the film along the line drawn on the image. The measured height (~ 10 nm) is consistent with the original thickness of 10 QL. The feature pointed by the arrow is probably a microwrinkle in the transferred film along the edge. **(e)** Plan view TEM image obtained from a 6 QL film grown on $\text{Al}_2\text{O}_3(0001)$ and transferred to a carbon foil and **(f)** corresponding SAED pattern acquired from the same sample. The scale bar is 5 nm^{-1} .

Fig. 8-2a,b shows optical images of a 10 QL thick Bi_2Se_3 film grown on $\text{Al}_2\text{O}_3(0001)$ and transferred to $\text{Al}_2\text{O}_3(0001)$ and $\text{Si}(111)$ substrates; part of the film is intentionally scratched to get a clear contrast. The excellent continuity of the film over a few millimeter length scale with uniform color contrast and absence of any wrinkles or bubbles in the images indicate the thickness uniformity and efficiency of the transfer process. Atomically flat film with long triangular terraces are observed in the AFM image (Fig. 8-2c) of a 10 QL-thick Bi_2Se_3 film transferred to $\text{Si}(111)$; there is no surface modification in the transferred film and the morphology looks similar to that of a pristine Bi_2Se_3 film. A large area, $5 \times 5 \mu\text{m}^2$, AFM scan is shown in Fig. 8-2d; the inset shows the height profile of the transferred film along the marked line. The large area scan shows one anomalous wavy feature, as pointed out by the arrow, which is probably due to a micro-wrinkle formed during the drying of the transferred film. The hexagonal atomic lattice structure seen in the TEM image of a 6 QL film (Fig. 8-2e) and the corresponding hexagonally symmetric pattern of the selected area electron diffraction (SAED) (Fig. 8-2f) also confirm the excellent quality of the transferred film.

8.2 Transport Analysis

Bi_2Se_3 films on Al_2O_3 substrates ($1 \text{ cm} \times 1 \text{ cm}$) were cut into four ($5 \text{ mm} \times 5 \text{ mm}$) pieces after spin-coating and curing PMMA on top; three of them were transferred onto $\text{Al}_2\text{O}_3(0001)$, $\text{Si}(111)$, and a-SiO_2 substrates, and the last piece was kept “as-is” to compare the transport properties before and after transfer. After the PMMA was removed from each sample, transport measurements were carried out with the van

der Pauw geometry in an AMI superconducting magnet with a base temperature of 1.5 K and a maximum field of 9 T. It was verified that PMMA curing without transfer on a pristine sample caused no significant degrading in the transport properties. The nonlinearity in the Hall resistance, R_{xy} , of the transferred films of varying thicknesses, Fig. 8-3a, implies that multiple channels contribute to the conduction; thus, only the total carrier concentration obtained from high B-field slope was considered.

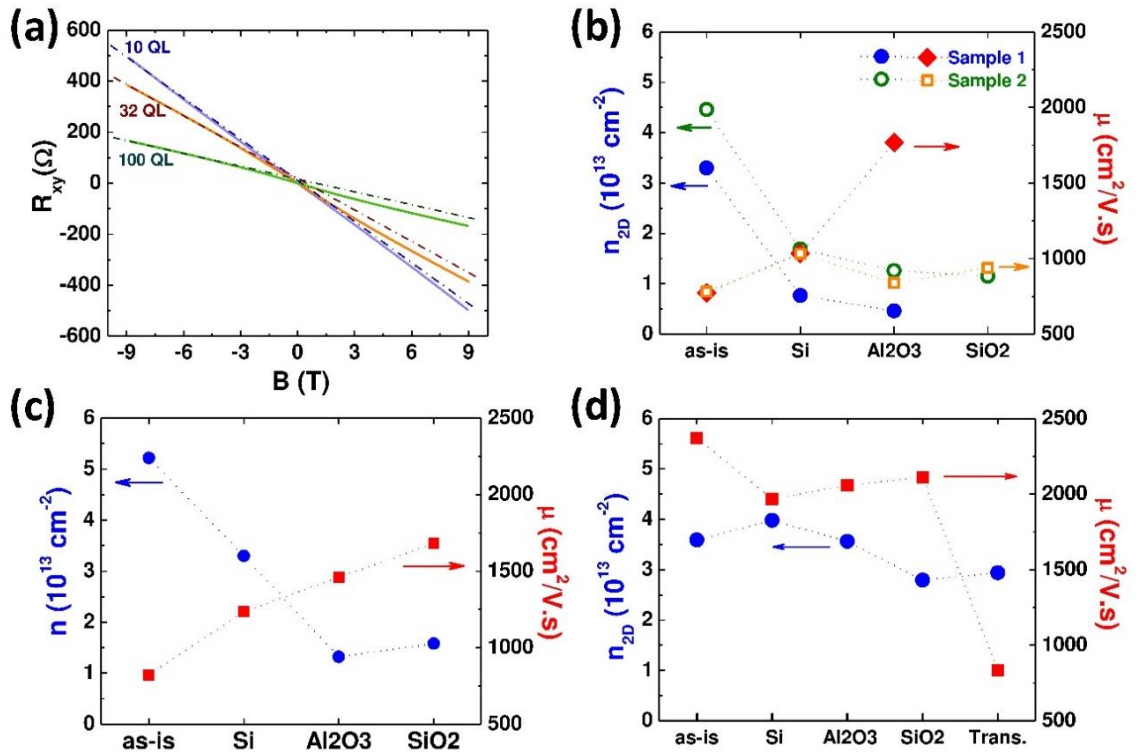


Fig. 8-3. Transport properties. **(a)** Hall resistance vs B for 10, 32, and 100 QL Bi₂Se₃ films transferred to a-SiO₂. The nonlinearity of the Hall resistance is indicative of multiple conducting channels; the dashed lines are straight guide lines, showing the level of nonlinearity for each curve. All samples are measured at 1.5 K and due to nonlinearity in the Hall resistance of these samples high field (~ 9 T) slope was used to estimate the total sheet carrier densities. Comparison of sheet carrier densities and corresponding mobilities of **(b)** 10 QL, **(c)** 32 QL thick Bi₂Se₃ films grown on Al₂O₃(0001), and **(d)** 100 QL Bi₂Se₃ film grown on a-SiO₂ transferred to different substrates, as labeled; the point *Trans.* refers to the film transferred to a common transparency sheet, and the point labeled *as-is* is the part of the film as grown on the initial substrate and not transferred.

Fig. 8-3b – Fig. 8-3d compares the transport properties of 10 QL (Fig. 8-3b) and 32 QL (Fig. 8-3c) Bi_2Se_3 films grown on $\text{Al}_2\text{O}_3(0001)$, and a 100 QL (Fig. 8-3d) Bi_2Se_3 film grown on a- SiO_2 before transfer (as-is) and after transferred onto different substrates. Because of the environmental doping effect (¹²⁴Brahlek *et al.*, 2011), exposure of Bi_2Se_3 films to air tends to increase the n-type carrier densities of the films with time. As these samples were left exposed to air for an indeterminable time, the as-is samples have higher sheet carrier density and lower mobility compared to pristine samples (⁹⁶Bansal *et al.*, 2012; ¹²³Bansal *et al.*, 2014). However, it is interesting to note that despite the aging effect in Bi_2Se_3 films, the transferred films have lower carrier concentrations than not only the as-is and but also the pristine samples (⁹⁶Bansal *et al.*, 2012; ¹²³Bansal *et al.*, 2014), especially in thinner films. This suggests that the transfer process is quite robust and is not affected much by aging of the samples.

We recently reported that though the high quality Bi_2Se_3 films on $\text{Al}_2\text{O}_3(0001)$ have very low bulk carrier densities, their surface charge defect density is quite substantial (⁹⁶Bansal *et al.*, 2012; ¹²³Bansal *et al.*, 2014). A plausible cause for the reduction in the carrier density after transfer is that the interface etching mechanism involved in the transferring process may either remove or neutralize the surface charge defects. This scenario is also supported by the observation that unlike the thinner samples, the change in the sheet carrier density of the thick 100 QL film grown on a- SiO_2 substrate during the transfer is relatively insignificant; because of comparatively large bulk contribution in the thicker films grown on a- SiO_2 (¹²³Bansal

et al., 2014), it is expected that the surface charge accounts for only a small fraction of the total sheet carrier density in these samples.

The change in mobility of the film after transfer also follows the above scenario. Mobility is a measure of scattering time and thus it is quite susceptible to disorders and interactions. Interestingly, Fig. 8-3 shows that most of the transferred films in the thin regime had their mobilities enhanced rather than degraded after the transfer. This enhancement in mobility indicates that the transfer process improves the film quality by removing the surface charge defects; this is quite surprising considering all the chemicals involved during the process. To demonstrate the applicability of this method to large-scale flexible electronics, we also measured a 100 QL film transferred from a-SiO₂ to a common transparency sheet as shown in Fig. 8-3d. The comparatively low mobility ($\sim 850 \text{ cm}^2/(\text{Vs})$) observed in this sample (labeled “Trans.” in Fig. 8-3d) is probably due to the graininess of the transparency sheet causing unevenness in the overlaying Bi₂Se₃ layer; still, the carrier density is comparable to those transferred onto other highly polished substrates.

8.3 Electrostatic Back-Gating & Metal - Insulator Transition via Dirac Gap

For the films transferred onto a-SiO₂, the Hall bar device was fabricated by ion milling in argon plasma through a shadow mask; the doped Si substrate was used as a back gate. It has been previously reported that argon bombardment induces hysteric metallic states on the surface of STO (¹²⁵Gross *et al.*, 2011; ¹²⁶Gross, Oh, 2011). Thus, for films transferred onto STO, manual patterning instead of ion milling was used to

make the Hall bar pattern, and silver paint was used to make the back contact. In both cases, the Hall bar width was 0.56 mm and the length measured between the mid points of the longitudinal voltage probes was 2.1 mm. The gating measurements were conducted using an electromagnet at a base temperature of 6 K and maximum magnetic field of ± 0.6 T. Fig. 8-4a shows a photograph of a Hall bar device with an 8 QL film grown on $\text{Al}_2\text{O}_3(0001)$ and transferred to a $5 \text{ mm} \times 5 \text{ mm} \times 0.5 \text{ mm}$ SrTiO_3 (STO) substrate; the substrate acts as a dielectric for back-gating purpose.

The initial carrier density of $\sim 8 \times 10^{12} \text{ cm}^{-2}$ implies that the Fermi level is low enough to be in the bulk band gap with no bulk contribution (¹¹⁸Cho *et al.*, 2011). This value of carrier concentration is lower than that of films of similar thickness grown directly on STO (⁶⁴Chen *et al.*, 2010; ⁶²Chen *et al.*, 2011). Fig. 8-4b shows the sheet resistance, R_{xx} , the low B-field Hall coefficient, R_H , (top panel), and corresponding sheet carrier density ($n_{2D} = 1/(eR_H)$) and mobility (bottom panel) as a function of applied back-gate voltage, V_G . By negatively biasing the gate, n-type carriers are depleted from the film, which is reflected as an increase in R_{xx} and decrease in R_H .

Beyond $V_G = -23 \text{ V}$, corresponding to an electron density of $1.7 \times 10^{12} \text{ cm}^{-2}$, R_H starts increasing and system crossovers from a pure electron regime to an electron-hole regime. R_H changes sign completely near $V_G = -39 \text{ V}$; this can be understood as Fermi level moving below Dirac point for both top and bottom surfaces and the transition of the system to a pure hole regime.

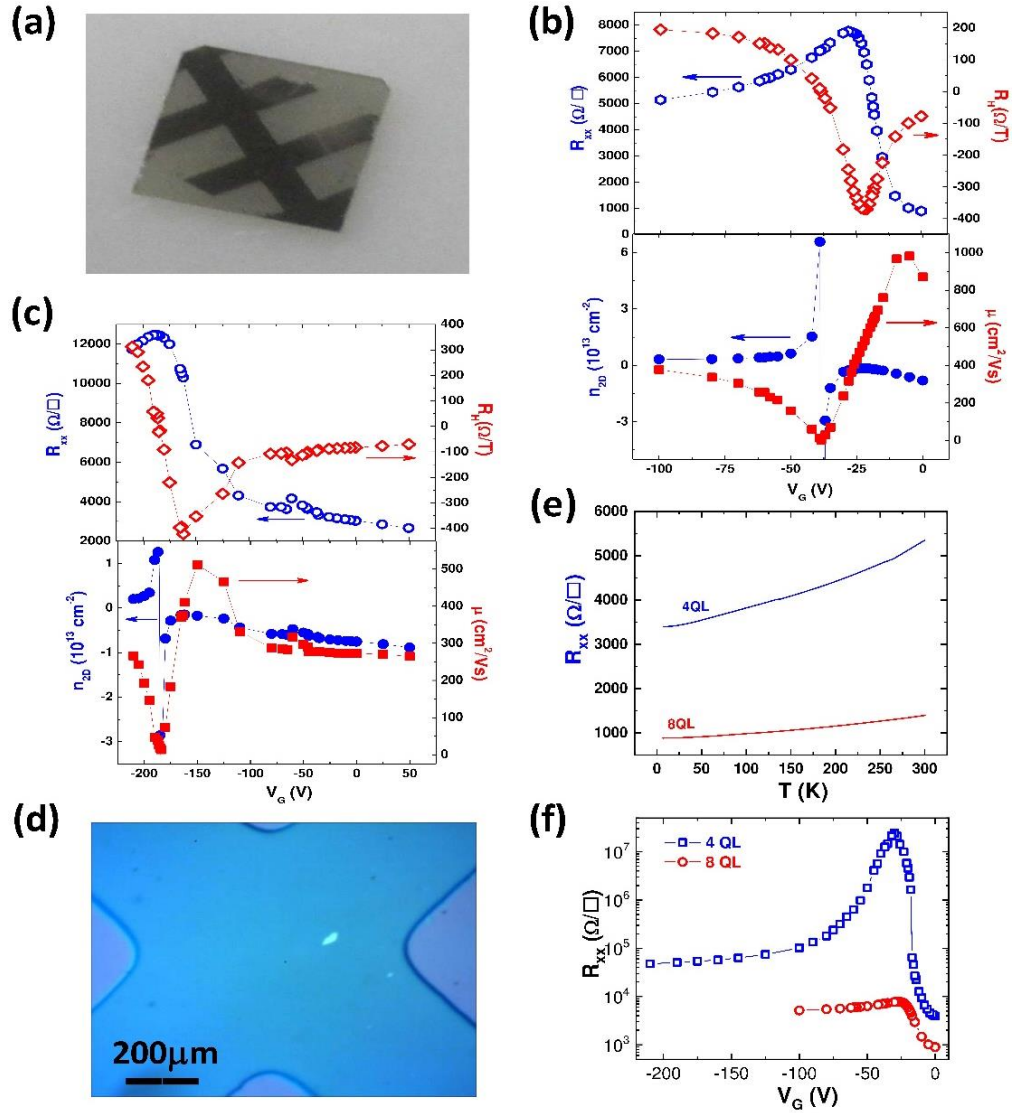


Fig. 8-4. Electrostatic back-gating of ultrathin transferred films. **(a)** Photograph of an 8 QL Bi_2Se_3 film grown on $\text{Al}_2\text{O}_3(0001)$ and transferred to STO (5 mm \times 5 mm); the Hall bar pattern was made manually through a metal shadow mask. **(b,c)** Longitudinal resistance, Hall resistance (top panel), and corresponding sheet carrier densities and mobility (bottom panel) of **(b)** an 8 QL-thick film grown on $\text{Al}_2\text{O}_3(0001)$ and transferred to STO, and **(c)** an 8 QL-thick film grown on a-SiO₂ and transferred back to a-SiO₂. **(d)** An optical image of a Hall bar device of a 4 QL Bi_2Se_3 film grown on $\text{Al}_2\text{O}_3(0001)$ and transferred to a-SiO₂; absence of any color change highlights the thickness uniformity of the ultrathin transferred film. **(e)** Resistance vs temperature for 8 QL and 4 QL Bi_2Se_3 films transferred onto STO; both show metallic temperature dependence. **(f)** Gate-voltage dependent longitudinal sheet resistance of an 8 QL-thick film (red circles) and a 4 QL-thick film (blue squares) grown on Al_2O_3 and transferred to STO as a function of back-gate voltage. Although four-probe method was used for all other cases, two-probe method had to be used for the highly resistive state ($V_G < -18$ V) of the 4 QL film.

As more negative bias is applied, more p-type carriers are injected, leading to a continuous drop in R_{xx} . Similar behavior was observed for an 8 QL Bi_2Se_3 film grown on a-SiO₂ and transferred back to a-SiO₂, using the doped Si as the back gate (Figure 4c). Again, by applying negative gate bias we were able to reduce the electron density from $8.8 \times 10^{12} \text{ cm}^{-2}$ at $V_G = 0 \text{ V}$ to $1.5 \times 10^{12} \text{ cm}^{-2}$ at $V_G = -162 \text{ V}$. P-type conduction was observed for $V_G < -185 \text{ V}$ accompanied with a maximum in longitudinal resistance, R_{xx} .

Finally, we demonstrate the electrostatic control of Fermi level through the hybridization gap opened at the Dirac point of a 4 QL thick Bi_2Se_3 film due to coupling of the top and bottom surfaces (⁶¹Zhang *et al.*, 2010). Regions of different thicknesses within a mechanically exfoliated Bi_2Se_3 crystal on a-SiO₂ have often been identified by color contrast of the film with respect to the substrate (⁸³Checkelsky *et al.*, 2011; ¹¹⁸Cho *et al.*, 2011). As observed by the uniformity in color in the optical image of a 4 QL film transferred from $\text{Al}_2\text{O}_3(0001)$ to a-SiO₂ (Fig. 8-4d), large-size ultrathin films of uniform thickness can be easily transferred by this process. Another major advantage is that, so far, some of the highest quality films have been achieved on $\text{Al}_2\text{O}_3(0001)$ (⁹⁶Bansal *et al.*, 2012; ⁹⁷Taskin *et al.*, 2012) and this method provides an efficient way to transfer these high quality films to arbitrary substrates. This is best exemplified by the observation that the resistance of the 4 QL film grown on $\text{Al}_2\text{O}_3(0001)$ and transferred onto STO shows metallic temperature dependence all the way down to the lowest measured temperatures (Fig. 8-4e). In such an ultrathin regime, only high mobility films show metallic temperature dependence (⁹⁶Bansal *et al.*, 2012), and films with low mobilities exhibit insulating temperature dependence

as observed in ultrathin films grown directly onto STO (¹²⁷Zhang *et al.*, 2013), cleaved from bulk (¹¹⁸Cho *et al.*, 2011), or exfoliated from nanoribbons (¹¹⁷Hong *et al.*, 2010), even if their Fermi levels are far from the hybridization gap. Therefore, the very observation of metallic temperature dependence of the 4 QL sample both before and after the transfer further evidence the robustness of this transfer process.

Fig. 8-4f shows the gate voltage dependence of R_{xx} for 4 and 8 QL thick films transferred from Al_2O_3 to STO. For the 8 QL film, R_{xx} was measured in a four-probe configuration, as shown in Fig. 8-4a. The 4 QL film was metallic with $n_{2D} = 6.2 \times 10^{12} \text{ cm}^{-2}$ and $\mu = 270 \text{ cm}^2/(\text{Vs})$ at $V_G = 0 \text{ V}$ but it soon became highly insulating on applying negative gate bias; for $V_G < -18 \text{ V}$, the sample became so insulating that we had to switch to the two probe method to measure the resistance in this regime, but we confirmed that the two-point and the four-point method provide consistent resistance values in the metallic regime. For both 4 and 8 QL films, the resistance increased as a negative gate voltage was applied, reached a maximum, and decreased with further increase in the magnitude of the gate voltage. This implies that the Dirac points were reached in both cases. However, a closer look reveals significant qualitative difference between the two. For the 8 QL film, the surface states remained metallic at all times with the resistance well below the quantum resistance (h/e^2) of $25.8 \text{ k}\Omega$ and the peak resistance ($7.8 \text{ k}\Omega/\text{sq.}$) was about ten times larger than the ungated value. On the other hand, even if the ungated 4 QL film was fully metallic with its resistance substantially lower than the quantum resistance, gating made the resistance cross the quantum resistance at $V_G \approx -15 \text{ V}$ and reach a maximum value of $\sim 25 \text{ M}\Omega/\text{sq.}$, which is 1000 times larger than the quantum resistance, covering four

orders of resistance modulation. In other words, while the 4 QL film is metallic when its Fermi level is far from the Dirac point, it becomes highly insulating as the Fermi level approaches the Dirac point.

The presence (absence) of the metal–insulator transition in the 4 QL (8 QL) film imply that the 8 QL film does have gapless Dirac states whereas the 4 QL sample has a gap at the Dirac point. According to the previous ARPES study, it is known that a gap is formed at the Dirac point for ultrathin TI films due to hybridization of the top and bottom surface states (⁶¹Zhang *et al.*, 2010). According to this observation, if the Fermi level is tuned in and out of the Dirac point, metal–insulator transition is obviously expected. However, despite numerous gating studies so far, no such observation has been made until now. There are multiple factors responsible for that. Sometimes, due to the difficulty in quality control in the ultrathin regime, ultrathin films exhibit extremely low mobilities; in such a case, the film remains insulating throughout the gating (¹¹⁸Cho *et al.*, 2011). In other cases, the carrier density (surface or bulk or both) is so high that the Fermi level cannot be fully tuned into the gap; in that case, the film remains metallic throughout the gating. The very observation of a clear metal–insulator transition in the transferred 4 QL film implies that we have effectively overcome these barriers by combining high quality film growth with the effective film transfer method. This work also demonstrates that unlike the graphene system, it is possible to turn off all the conducting channels in properly engineered TI films, which is a highly desired property for device applications.

8.4 Conclusion

To summarize, we have shown that high-quality MBE-grown Bi_2Se_3 films of any thickness, as low as 4 nm, can be easily transferred to a whole range of desired substrates, including flexible transparencies. Using this process, we demonstrated complete suppression of the metallic transport channel in an ultrathin film by tuning the Fermi level into the hybridization gap formed at the Dirac point. The efficient back-gating effect also suggests that the substrate side of the transferred films is free of significant defects, which could work as traps for mobile carriers. Considering that MBE allows atomic-level control of various heterostructures, transferring MBE-grown TI films to arbitrary templates will bring many new opportunities for novel TI devices.

Chapter 9. FUTURE RESEARCH

9.1 Review

To explore a new material and grow thin films by MBE, the first step is to maintain stable fluxes for the multiple source elements being used, which becomes challenging in an oxygen environment. Considering that La is one of the most easily oxidized element, and Cu requires extreme oxidation conditions, to control their stoichiometry during growth, the aim is to stabilize the flux of easily oxidized elements better than 1%. Using easily oxidized Sr as the source material, varying flux values, port geometries and source shapes were studied (⁴⁷Kim *et al.*, 2010). Crucible aperture insert scheme with different aperture materials and positions were also tested which resulted in an improved flux stability by a factor of four (¹²⁸Kim *et al.*, 2010). On further investigation, the source oxidation issue was resolved by using a self-gettering differential pump (¹²⁹Kim *et al.*, 2011).

Next step was to optimize the growth procedure for thin TI Bi₂Se₃ films – starting with an atomically smooth single crystal substrate. Bi₂Se₃ grows in atomic layers with a sequence of Se-Bi-Se-Bi-Se forming a quintuple layer. High quality

epitaxial growth of Bi₂Se₃ on Si(111) with an atomically sharp interface was achieved using a two-step growth process (¹³⁰Bansal *et al.*, 2010). Using a 9 T superconducting magnet system, the electronic transport properties of these films were studied as a function of thickness (⁹⁰Kim *et al.*, 2011). The film quality was further improved by growing Bi₂Se₃ films on Al₂O₃ substrates; allowing observation of dominant, thickness-independent surface transport channels over two orders of the thickness range (⁹⁶Bansal *et al.*, 2012). Because of the large difference in transport properties of Bi₂Se₃ grown on different substrates the effect of substrate was investigated by growing films on amorphous SiO₂; comparison of transport properties suggested that the chemical compatibility of the substrate was a crucial factor for growing good Bi₂Se₃ films. Also, growth on amorphous SiO₂ allowed electrostatic gating experiments by fabrication and measurement of a field-effect transistor (¹²³Bansal *et al.*, 2014). A scheme to transfer ultrathin films of Bi₂Se₃, ≥ 4 nm, to a whole range of substrates including flexible transparencies was developed; while preserving the transport properties, such as carrier concentration, and mobility, during the transfer process (¹³¹Bansal *et al.*, 2014).

9.2 Future Scope

In the past years, several improvements have been observed in both TI thin films and stabilizing source fluxes for complex-oxide growth. With many interesting properties already known, and many awaiting discovery, TI – complex oxide heterostructures seem to be a consummate platform.

Commonly used capping materials, such as Se or In_2Se_3 , seem to pull Se out of the Bi_2Se_3 surface layer, resulting in an increased carrier density. Thus, on the materials side, a reliable capping material needs to be researched to protect the topological insulator films from atmospheric effects. Another feature to look for in the capping layer scheme is the potential to act as a gate dielectric, allowing Fermi level tuning.

On the physics side, topological surface states can be engineered by integrating with ferromagnetic or superconducting materials. Majorana fermion states supported by introduction of a superconducting bandgap in the surface states seem promising for quantum device innovation. Integrating TIs with an electrically insulating ferromagnet can result in observation of quantum anomalous hall phase at tens of Kelvin. Spintronics uses the spin of electrons to perform *on-off* logic operation or to act as data storage; using TIs with their strong spin-momentum locking could potentially solve the issue of spin-dephasing across micron-scale devices.

Lastly, with the ever-evolving understanding of topological states, one needs to find new topological materials that do not suffer intrinsic defects, such as thermodynamically favorable vacancies, as seen in layered chalcogenide TIs.

“The Stone Age didn’t end because we ran out of stones, but because we moved on to better materials”

REFERENCES

1. M. J. Brahlek. *Atomic Scale Engineering of Topological Materials*. Doctoral dissertation. Rutgers, the State University of New Jersey, 2014.
doi:<https://doi.org/doi:10.7282/T3TM78KB>
2. C. L. Kane and E. J. Mele, *Phys. Rev. Lett.* **95**, 146802 (2005).
3. C. L. Kane and E. J. Mele, *Phys. Rev. Lett.* **95**, 226801 (2005).
4. M. Hood. (2016, October 5). *When is a coffee mug a donut? Topology explains it*. Retrieved from www.gmanetwork.com
<http://www.gmanetwork.com/news/scitech/science/583886>
5. M. Nakahara. *Geometry, Topology and Physics*. London: Institute of Physics Publishing, 2003. Print.
6. M. V. Berry, *Proc. R. Soc Lond A Math. Phys. Sci.* **392**, 45–57 (1984).
7. K. V. Klitzing, G. Dorda and M. Pepper, *Phys. Rev. Lett.* **45**, 494–497 (1980).
8. M. Z. Hasan and C. L. Kane, *Rev. Mod. Phys.* **82**, 3045–3067 (2010).
9. B. I. Halperin, *Phys. Rev. B* **25**, 2185–2190 (1982).
10. D. J. Thouless, M. Kohmoto, M. P. Nightingale, and M. den Nijs, *Phys. Rev. Lett.* **49**, 405–408 (1982).
11. L. Fu and C. Kane, *Phys. Rev. B - Condens. Matter Mater. Phys.* **76**, 045302 (2007).
12. L. Fu, C. L. Kane and E. J. Mele, *Phys. Rev. Lett.* **98**, 106803 (2007).
13. B. A. Bernevig, T. L. Hughes and S-C. Zhang, *Science* **314**, 1757–1761 (2006).
14. B. A. Bernevig and S-C. Zhang, *Phys. Rev. Lett.* **96**, 106802 (2006).
15. X-L. Qi, Y-S. Wu and S-C. Zhang, *Phys. Rev. B* **74**, 085308 (2006).
16. X-L. Qi, T. L. Hughes and S-C. Zhang, *Phys. Rev. B* **78**, 195424 (2008).
17. J. E. Moore and L. Balents, *Phys. Rev. B* **75**, 121306 (2007).
18. S-C. Zhang and J. Hu, *Science* **294**, 823–828 (2001).
19. X-L. Qi and S-C. Zhang, *Phys. Today* **63**, 33 (2010).
20. C. Kane and J. Moore, *Phys. World February*, 32–36 (2011).
21. M. König, S. Wiedmann, C. Brune, A. Roth, H. Buhmann, L. W. Molenkamp, X-L. Qi and S-C. Zhang, *Science* **318**, 766–770 (2007).
22. D. Hsieh, D. Qian, L. Wray, Y. Xia, Y. S. Hor, R. J. Cava and M. Z. Hasan, *Nature* **452**, 970–4 (2008).
23. Y. L. Chen, J. G. Analytis, J-H. Chu, Z. K. Liu, S-K. Mo, X-L. Qi, H. J. Zhang, D. H. Lu, X. Dai, Z. Fang, S-C. Zhang, I. R. Fisher, Z. Hussain and Z-X. Shen, *Science* **325**, 178–81 (2009).

24. Y. Xia, D. Qian, D. Hsieh, L. Wray, A. Pal, H. Lin, A. Bansil, D. Grauer, Y. S. Hor, R. J. Cava and M. Z. Hasan, *Nat. Phys.* **5**, 398–402 (2009).
25. P. Roushan, J. Seo, C. V. Parker, Y. S. Hor, D. Hsieh, D. Qian, A. Richardella, M. Z. Hasan, R. J. Cava and A. Yazdani, *Nature* **460**, 1106–9 (2009).
26. R. F. C. Farrow. *Molecular Beam Epitaxy - Applications to Key Materials*. Park Ridge: Noyes Publications, 1995. Print.
27. K. Barnham and D. Vvedensky. *Low- Dimensional Semiconductor Structures*. New York: Cambridge University Press, 2001. Print.
28. E. S. Hellman and E. H. Hartford Jr., *J. Vac. Sci. Technol. B* **12**, 1178 (1994).
29. J. Lettieri, J. H. Haeni and D. G. Schlom, *J. Vac. Sci. Technol. A* **20**, 1332 (2002).
30. I. Bozovic and J. N. Eckstein, *MRS Bull.* **6**, 32 (1995).
31. S. Oh, T. A. Crane, D. J. Van Harlingen and J. N. Eckstein, *Phys. Rev. Lett.* **96**, 107003 (2006).
32. S. Oh and J. N. Eckstein, *Thin Solid Films* **483**, 301–305 (2005).
33. J-P. Locquet and E. Machler, *MRS Bull.* **Sept** 39–43 (1994).
34. C. D. Theis and D. G. Schlom, *J. Vac. Sci. Technol. A Vacuum* **14**, 2677 (1996).
35. C. D. Theis and D. G. Schlom, *J. Cryst. Growth* **174**, 473–479 (1997).
36. M. E. Klausmeier-Brown, J. N. Eckstein, I. Bozovic and G. F. Virshup, *Appl. Phys. Lett.* **60**, 657 (1992).
37. Y. Kasai and S. Sakai, *Rev. Sci. Instrum.* **68**, 2850 (1997).
38. S. Oh, T. Di Luccio and J. N. Eckstein, *Phys. Rev. B* **71**, 052504 (2005).
39. R. H. Lamoreaux and D. L. Hildenbrand, *J. Phys. Chem. Ref. Data* **16**, 419 (2009).
40. D. M. Kearns, D. R. Gillen, D. Voulot, R. W. McCullough and W. R. Thompson, *J. Vac. Sci. Technol. A* **19**, 993 (2001).
41. Miller, J. N. aip_jvn10_803. *J. Vac. Sci. Technol. B Microelectron. Nanom. Struct.* **10**, 803–6 (1992).
42. G. W. Turner, B. A. Nechay and S. J. Eglash, *J. Vac. Sci. Technol. B* **8**, 283 (1990).
43. P. A. Maki, S. C. Palmateer, A. R. Calawa and B. R. Lee, *J. Vac. Sci. Technol.* **4**, 564 (1986).
44. F. C. Celii, Y. C. Kao, H-Y. Liu, L. A. Files-Sesler and E. A. Beam III, *J. Vac. Sci. Technol.* **11**, 1014 (1998).
45. A. J. SpringThorpe, A. Majeed, C. J. Miner Z. R. Wasilewski and G. C. Aers, *J. Vac. Sci. Technol. A* **9**, 3175 (1998).
46. R. N. Sacks, G. A. Patterson and K. A. Stair, *J. Vac. Sci. Technol. B* **14**, 2187 (1996).
47. Y. S. Kim, N. Bansal, C. Chaparro, H. Gross and S. Oh, *J. Vac. Sci. Technol. A* **28**,

- 271 (2010).
48. P. Cheng, C. Song, T. Zhang, Y. Zhang, Y. Wang, J-F. Jia, J. Wang, Y. Wang, B-F. Zhu, X. Chen, X. Ma, K. He, L. Wang, X. Dai, Z. Fang, X. Xie, X-L. Qi, C-X. Liu, S-C. Zhang and Q-K. Xue, *Phys. Rev. Lett.* **105**, 076801 (2010).
 49. H. Zhang, C-X. Liu, X-L. Qi, X. Dai, Z. Fang and S-C. Zhang, *Nat. Phys.* **5**, 438–442 (2009).
 50. J. Moore, *Nat. Phys.* **5**, 378–380 (2009).
 51. H. Peng, K. Lai, D. Kong, S. Meister, Y. Chen, X-L. Qi, S-C. Zhang, Z-X. Shen and Y. Cui, *Nat. Mater.* **9**, 225–9 (2010).
 52. H. Lind, S. Lidin and U. Haussermann, *Phys. Rev. B* **72**, 184101 (2005).
 53. H. Okamoto, *J. Phase Equilibria* **15**, 195 (1994).
 54. A. P. Torane and C. Bhosale, *Mater. Res. Bull.* **36**, 1915 (2001).
 55. W. Wang, Y. Geng, Y. Qian, Y. Xie and X. Liu, *Mater. Res. Bull.* **34**, 131–134 (1999).
 56. B. R. Sankapal, R. S. Mane and C. D. Lokhande, *Mater. Chem. Phys.* **63**, 230 (2000).
 57. R. K. Nkum, A. A. Adimado and H. Totoe, *Mater. Sci. Eng. B* **55**, 102–108 (1998).
 58. G. Zhang, H. Qin, J. Teng, J. Guo, Q. Guo, X. Dai, Z. Fang and K. Wu, *Appl. Phys. Lett.* **95**, 053114 (2009).
 59. H. D. Li, Z. Y. Wang, X. Kan, X. Guo, H. T. He, Z. Wang, J. N. Wang, T. L. Wong, N. Wang and M. H. Xie, *New J. Phys.* **12**, 103038 (2010).
 60. C-L. Song, Y-L. Wang, Y-P. Jiang, Y. Zhang, C-Z. Chang, L. Wang, K. He, X. Chen, J-F. Jia, Y. Wang, Z. fong, X. Dai, X-C. Xie, X-L. Qi, S-C. Zhang, Q-K. Xue and X. Ma, *Appl. Phys. Lett.* **97**, 143118 (2010).
 61. K. He, Q-K. Xue *et al.*, *Nat. Phys.* **6**, 584–588 (2010).
 62. M. Liu, C-Z. Chang, Z. Zhang, Y. Zhang, W. Ruan, K. He, L. Wang, X. Chen, J-F. Jia, S-C. Zhang, Q-K. Xue, X. Ma and Y. Wang, *Phys. Rev. B* **83**, 165440 (2011).
 63. A. Richardella, D. M. Zhang, J. S. Lee, A. Koser, D. W. Rench, A. L. Yeats, B. B. Buckley, D. D. Awschalom and N. Samarth, *Appl. Phys. Lett.* **97**, 262104 (2010).
 64. J. Chen, H. J. Qin, F. Yang, J. Liu, T. Guan, F. M. Qu, G. H. Zhang, J. R. Shi, X. C. Xie, C. L. Yang, K. H. Wu, Y. Q. Li and L. Lu, *Phys. Rev. Lett.* **105**, 176602 (2010).
 65. A. Koma, *Thin Solid Films* **216**, 72–76 (1992).
 66. A. Ishizaki and Y. Shiraki, *J. Electrochem. Soc.* **133**, 666 (1986).
 67. G. E. Becker and J. C. Bean, *J. Appl. Phys.* **48**, 3395–3399 (1977).
 68. J. C. Bean, *J. Vac. Sci. Technol.* **1**, 540 (1983).
 69. Y. Wei, X. Hu, Y. Liang, D. C. Jordan, B. Craigo, R. Droopad, Z. Yu, A. Demkov, J. L. Edwards and W. J. Ooms, *J. Vac. Sci. Technol. B* **20**, 1402 (2002).

70. G. Wang, X. Zhu, J. Wen, X. Chen, K. He, L. Wang, X. Ma, Y. Liu, X. Dai, Z. Fang, J. Jia and Q-K. Xie, *Nano Res.* **3**, 874–880 (2010).
71. Y. Sakamoto, T. Hirahara, H. Miyazaki, S-I. Kimura and S. Hasegawa, *Phys. Rev. B* **81**, 165432 (2010).
72. T. Hirahara, Y. Sakamoto, Y. Takeichi, H. Miyazaki, S-I. Kimura, I. Matsuda, A. Kakizaki and S. Hasegawa, *Phys. Rev. B* **82**, 155309 (2010).
73. R. D. Bringans and M. A. Olmstead, *Phys. Rev. B* **39**, 12985–12988 (1989).
74. Y-Y. Li, G. Wang, X-G. Zhu, M-H. Liu, C. Ye, X. Chen, Y-Y. Wang, K. He, L-l. Wang, X-C. Ma, H-J. Zhang, X. Dai, Z. Fang, X-C. Xie, Y. Liu, X-L. Qi, J-F. Jia, S-C. Zhang and Q-K. Xue, *Adv. Mater.* **22**, 4002–7 (2010).
75. J. G. Analytis, J-H. Chu, Y. Chen, F. Corredor, R. D. McDonald, Z-X. Shen and I. R. Fisher, *Phys. Rev. B* **81**, 205407 (2010).
76. A. Elshabini and F. D. Barlow. *Thin Film Technology Handbook*. New York:McGraw-Hill. 1998. Print.
77. J. Linder, T. Yokoyama and A. Sudbo, *Phys. Rev. B* **80**, 205401 (2009).
78. H-Z. Lu, W-Y. Shan, W. Yao, Q. Niu and S-Q. Shen, *Phys. Rev. B* **81**, 115407 (2010).
79. M. Bianchi, D. Guan, S. Bao, J. Mi, B. Brummerstedt Iversen, P. D. C. King and P. Hofmann, *Nat. Commun.* **1**, 128 (2010).
80. Y. S. Hor, A. Richardella, P. Roushan, Y. Xia, J. G. Checkelsky, A. Yazdani, M. Z. Hasan, N. P. Ong and R. J. Cava, *Phys. Rev. B* **79**, 195208 (2009).
81. D. Kong, J. J. Chan, K. Lai, H. Leng, J. G. Analytis, S. Meister, Y. Chen H-J. Zhang, E. R. Fisher, Z-X. Shen and Y. Cui, *ACS Nano* **5**, 4698–4703 (2011).
82. J. M. Ziman. *Electrons and Phonons: The theory of Transport Phenomenon in Solids*. Oxford: Clarendon Press. 1960. Print.
83. J. G. Checkelsky, Y. S. Hor, R. J. Cava and N. P. Ong, *Phys. Rev. Lett.* **106**, 196801 (2011).
84. S. Hikami, A. I. Larkin and Y. Nagaoka, *Prog. Theor. Phys.* **63**, 707–710 (1980).
85. J. Chen, X. Y. e, K. H. Wu, Z. Q. Ji, L. Lu, J. R. Shi, J. H. Smet and Y. Q. Li, *Phys. Rev. B* **83**, 241304 (2011).
86. H. Steinberg, J-B. Laloe, V. Fatemi, J. S. Moodera and P. Jarillo-Herrero, *Phys. Rev. B* **84**, 233101 (2011).
87. S. Gota, E. Guiot, M. Henriot and M. Gautier-Soyer, *Phys. Rev. B* **60**, 14387 (1999).
88. H. D. Li, Z. Y. Wang, X. Kan, X. Guo, H. T. He, Z. Wang, J. N. Wang, T. L. Wong, N. Wang and M. H. Xie, *New J. Phys.* **12**, 103038 (2010).
89. N. Bansal, Y-S. Kim, E. Edrey, M. Brahlek, Y. Horibe, K. Iida, M. Tanimura, G-H. Li, T. Feng, H-D. Lee, T. Gustafsson, E. Andrei and S. Oh, *Thin Solid Films* **520**, 224–229 (2011).

90. Y-S. Kim, M. Brahlek, N. Bansal, E. Edrey, G. A. Kapilevich, K. Iida, M. Tanimura, Y. Horibe, S-W. Cheong and S. Oh, *Phys. Rev. B* **84**, 073109 (2011).
91. C. Chen, S. He, H. Weng, W. Zhang, L. Zhao, H. Liu, Z. Jia, D. Mou, S. Liu, J. He, Y. Peng, Y. Feng, Z. Xie, G. Liu, X. Dong, J. Zhang, X. Wang, Q. Peng, Z. Wang, S. Zhang, F. Yang, C. Chen, Z. Xu, X. Dai, Z. Fang and X. J. Zhou, *Proc. Natl. Acad. Sci. U. S. A.* **109**, 3694–8 (2012).
92. P. D. C. King, R. C. Hatch, M. Bianchi, R. Ovsyannikov, C. Lupulescu, G. Landolt, B. Slomski, J. H. Dil, D. Guan, J. L. Mi, E. D. L. Rienks, J. Fink, A. Lindblad, S. Svensson, S. Bao, G. Balakrishnan, B. B. Iversen, J. Osterwalder, W. Eberhardt, F. Baumberger and P. Hofmann, *Phys. Rev. Lett.* **107**, 096802 (2011).
93. D. Hsieh, Y. Xia, D. Qian, L. Wray, J. H. Dil, F. Meier, J. Osterwalder, L. Patthey, J. G. Checkelsky, N. P. Ong, A. V. Fedorov, H. Lin, A. Bansil, D. Grauer, Y. S. Hor, R. J. Cava and M. Z. Hasan, *Nature* **460**, 1101–5 (2009).
94. Z. Y. Wang, H. D. Li, X. Guo, W. K. Ho and M. H. Xie, *J. Cryst. Growth* **334**, 96–102 (2011).
95. N. V. Tarakina, S. Schreyeck, T. Borzenko, C. Schumacher, G. Karczewski, K. Brunner, C. Gould, H. Buhmann and L. W. Molenkamp, *Cryst. Growth Des.* **12**, 1913–1918 (2012).
96. N. Bansal, Y. S. Kim, M. Brahlek, E. Edrey and S. Oh, *Phys. Rev. Lett.* **109**, 116804 (2012).
97. A. A. Taskin, S. Satoshi, K. Segawa and Y. Ando, *Phys. Rev. Lett.* **109**, 066803 (2012).
98. C-Z. Chang, K. He, L-L. Wang, X-C. Ma, M-H. Liu, Z-C. Zhang, X. Chen, Y-Y. ang and Q-K. Xue, *Spin* **01**, 21–25 (2011).
99. L. Zhang, R. Hammond, M. Dolev, M. Liu, A. Palevski and A. Kapitulnik, *Appl. Phys. Lett.* **101**, 153105 (2012).
100. X. F. Kou, L. He, X. Xiu, M. R. Lang, Z. M. Liao, Y. Wang, A. V. FEdorov, X. X. Yu, J. S. Tang, G. Huang, X. W. Jiang, J. F. Zhu, J. Zhou and K. L. wang, *Appl. Phys. Lett.* **98**, 242102 (2011).
101. L. He, F. Xiu, X. Yu, M. Teague, W. Jiang, Y. Fan, X. Kou, M. Lang, Y. Wang, G. Hiang, N-C. Yeh and K. L. Wang, *Nano Lett.* **12**, 1486–90 (2012).
102. S-K. Jerng, K. Joo, Y. Kim, S-M. Yoon, J. H. Lee, M. Kim, J. S. Kim, E. Yoon, S-H. Chun and Y. S. Kim, *Nanoscale* **5**, 10618–22 (2013).
103. D. Hsieh, Y. Xia, L. Wray, D. Qian, A. Pal, J. H. Dil, J. Osterwalder, F. Meier, G. Bihlmayer, C. L. Kane, Y. S. Hor, R. J. Cava and M. Z. Hasan, *Science* **323**, 919–22 (2009).
104. J. G. Checkelsky, Y. S. Hor, M-H. Liu, D-X. Qu, R. J. Cava and N. P. Ong, *Phys. Rev. Lett.* **103**, 246601 (2009).
105. N. P. Butch, K. Kirshenbaum, P. Syers, A. B. Sushkov, G. S. Jenkins, H. D. Drew and J. Paglione, *Phys. Rev. B* **81**, 241301 (2010).

106. F. Xiu, L. He, Y. Wang, L. Cheng, L-T. Cheng, M. Lang, G. Huang, X. Kou, Y. Zhou, X. Jiang, Z. Chen, J. Zou, A. Shailos and K. L. Wang, *Nat. Nanotechnol.* **6**, 216–21 (2011).
107. M. Brahlek, N. Bansal, N. Koirala, S-Y. Xu, M. Neupane, C. Liu, M. Z. Hasan and S. Oh, *Phys. Rev. Lett.* **109**, 186403 (2012).
108. D-X. Qu, Y. S. Hor, J. Xiong, R. J. Cava and N. P. Ong, *Science* **329**, 821–4 (2010).
109. Y. Yu, W. Zhang, S-C. Zhang, X. Dai and Z. Fang, *Science* **329**, 61–4 (2010).
110. C-Z. Chang, J. Zhang, X. Feng, J. Shen, Z. Zhang, M. Guo, K. Li, Y. Ou, P. Wei, L-L. Wang, Z-Q. Ji, Y. Feng, S. Ji, X. Chen, J. Jia, X. Dai, Z. Fang, S-C. Zhang, K. He, Y. Wang, L. Lu, X-C. Ma and Q-K. Xue, *Science* **340**, 167–70 (2013).
111. L. Fu and C. L. Kane, *Phys. Rev. Lett.* **100**, 096407 (2008).
112. A. R. Akhmerov, J. Nilsson and C. W. J. Beenakker, *Phys. Rev. Lett.* **102**, 216404 (2009).
113. I. Garate and M. Franz, *Phys. Rev. Lett.* **104**, 146802 (2010).
114. X-L. Qi, R. Li, J. Zang and S-C. Zhang, *Science* **323**, 1184–7 (2009).
115. D. Kim, S. Cho, N. P. Butch, P. Syers, K. Kirshenbaum, S. Adam, J. Paglione and M. S. Fuhrer, *Nat. Phys.* **8**, 460–464 (2012).
116. J. Velasco Jr, Z. Zhao, H. Zhang, F. Wang, Z. Wang, P. Kratz, L. Jing, W. Bao, J. Shi and C. N. Lau, *Nanotechnol.* **22**, 285305 (2011).
117. S. S. Hong, W. Kundhikanjana, J. J. Cha, K. Lai, D. Kong, S. Meister, M. A. Kelly, Z-X. Shen and Y. Cui, *Nano Lett.* **10**, 3118–22 (2010).
118. S. Cho, N. P. Butch, J. Paglione and M. S. Fuhrer, *Nano Lett.* **11**, 1925–7 (2011).
119. X. Li, Y. Zhu, W. Cai, M. Borysiak, B. Han, D. Chen, R. D. Piner, L. Colomco and R. S. Ruoff, *Nano Lett.* **9**, 4359–63 (2009).
120. A. Reina, X. Jia, J. Ho, D. Nezich, H. Son, V. Bulovic, M. S. Dresselhaus and J. Kong, *Nano Lett.* **9**, 30–5 (2009).
121. G-H. Lee, Y-J. Yu, C. Lee, C. Dean, K. L. Shepard, P. Kim and J. Hone, *Appl. Phys. Lett.* **99**, 243114 (2011).
122. S. Bertolazzi, J. Brivio and A. Kis, *ACS Nano* **5**, 9703–9 (2011).
123. N. Bansal, N. Koirala, M. Brahlek, M-G. Han, y. Zhu, Y. Cao, J. Waugh, D. S. Dessau and S. Oh, *Appl. Phys. Lett.* **104**, 241606 (2014).
124. M. Brahlek, Y. S. Kim, N. Bansal, E. Edrey and S. Oh, *Appl. Phys. Lett.* **99**, 012109 (2011).
125. H. Gross, N. Bansal, Y-S. Kim and S. Oh, *J. Appl. Phys.* **110**, 073704 (2011).
126. H. Gross and S. Oh, *Appl. Phys. Lett.* **99**, 092105 (2011).
127. T. Zhang, N. Levy, J. Ha, Y. Kuk and J. A. Stroscio, *Phys. Rev. B* **87**, 115410 (2013).
128. Y. S. Kim, N. Bansal and S. Oh, *J. Vac. Sci. Technol. A* **28**, 600 (2010).

129. Y. S. Kim, N. Bansal and S. Oh, *J. Vac. Sci. Technol. A* **29**, 041505 (2011).
130. N. Bansal, Y. S. Kim, E. Edrey, M. Brahlek, Y. Horibe, K. Iida, M. Tanimura, G-H. Li, T. Feng, H-D. Lee, T. Gustafsson, E. Andrei and S. Oh, *Thin Solid Films* **520**, 224–229 (2011).
131. N. Bansal, M. R. Cho, M. Brahlek, N. Koirala, Y. Horibe, J. Chen, W. Wu, Y. D. Park and S. Oh, *Nano Lett.* **14**, 1343–8 (2014).